NASA CONTRACTOR REPORT

NASA CR-2899

STUDY OF NOISE AND INFLOW DISTORTION SOURCES IN THE NASA QF-1B FAN USING MEASURED BLADE AND VANE PRESSURES

Donald B. Hanson

Prepared by
HAMILTON STANDARD
Windsor Locks, Conn. 06096
for Lewis Research Center

NATIONAL AERONAUTICS AND SPACE ADMINISTRATION • WASHINGTON, D. C. • SEPTEMBER 1977

1. Report No.	2. Government Accession No.	3. Recipient's Catalog
NASA CR-2899		

4. Title and Subtitle	5. Report Date
STUDY OF NOISE AND INFLOW DISTORTION SOURCES IN THE NASA QF-1B FAN USING MEASURED BLADE AND VANE PRESSURES	September 1977
	6. Performing Organization Code
7. Author(s)	8. Performing Organization Report No.
Donald B. Hanson	None
	10. Work Unit No.
9. Performing Organization Name and Address	
Hamilton Standard Windsor Locks, Connecticut 06096	11. Contract or Grant No. NAS3-19749
	13. Type of Report and Period Covered Contractor Report
12. Sponsoring Agency Name and Address	
National Aeronautics and Space Administration Washington, D.C. 20546	14. Sponsoring Agency Code

15. Supplementary Notes

Final report. Project Manager, Joseph R. Balombin, V/STOL and Noise Division, NASA Lewis Research Center, Cleveland, Ohio 44135

16. Abstract

Pressure transducers were installed on the blades and vanes of QF-1B, a transonic-tip-speed fan from the NASA Quiet Fan Program which was tested on the outdoor quiet fan test facility at NASA-Lewis. Signals from the transducers and from far field microphones were analyzed to determine sources of nonuniform inflow and noise. The nonuniform inflow was mostly unsteady with roughly equal contributions from atmospheric turbulence and rig interference. The rig interference was largest at the bottom and appeared to be generated by the support structure which was located behind the inlet lip under the fan. Interaction of this inflow distortion was the dominant source of noise at 1, 2, and 3 times blade passing frequency (BPF) at 60, 70, and 80 percent of design speed. At 90 percent speed, noise at BPF was dominated by the steady rotor field. A broadband spectrum peak centered at about 2.2 times BPF was identified as rotor/stator interaction stemming from a high frequency rotor exit flow component. The remaining broadband energy from 0.3 to 3.5 times BPF was attributed to the better known type of rotor/stator interaction associated with rotor wake turbulence.

17. Key Words (Suggested by Author(s))	18. Distribution Statement
Fan noise Noise theory Inlet distortion Inlet turbulence Blade pressure	Unclassified - unlimited STAR Category 02

19. Security Classif. (of this report)	20. Security Classif. (of this page)	21. No. of Pages	22. Price*
Unclassified	Unclassified	84	A05

* For sale by the National Technical Information Service, Springfield, Virginia 22161

CONTENTS

STUDY OF NOISE AND INFLOW DISTORTION SOURCES IN THE NASA QF-1B FAN USING MEASURED BLADE AND VANE PRESSURES

By Donald B. Hanson
Hamilton Standard
Division of United Technologies Corporation

SUMMARY

The QF-1B is a 1.83m (6 ft) diameter, 1.5 design pressure ratio research fan designed to test low noise concepts for propulsion turbofans. Noise reduction features include a high vane/blade ratio (112/53), a large rotor/stator spacing (3.6 rotor chords), and a low design tip speed 338m/sec (1110 ft/sec). The fan was run statically in the front drive configuration on the outdoor full scale fan test facility at NASA-Lewis while tape recordings were made of signals from far field microphones and pressure transducers flush mounted on the rotor blades and stator vanes. The tapes were analyzed at Hamilton Standard using computerized analytical techniques developed previously in Q-Fan™ studies. The objectives of the work were to diagnose sources of non-uniform inflow and to establish the dominant noise generating mechanisms in the fan.

In this report the inflow distortion is analyzed in terms of the unsteady rotor blade pressures caused by atmospheric turbulence and rig interference. Atmospheric turbulence effects are considered to act more or less uniformly around the circumference whereas rig interference, which is roughly an equal contributor to the distortion, acts mainly at the bottom of the inlet. The source of rig interference appears to be the support structure which is located behind the inlet lip underneath the fan. The distortion is mostly unsteady, particularly the smaller scale distortion which is important for noise generation.

A noise spectrum peak occurs at approximately 2.2 times blade passing frequency at all RPMs' tested. Because the stator pressure signals exhibit the same spectrum peak, stator radiation is clearly the source. Although no satisfactory explanation was found for stator excitation at this frequency, it seems possible that the mean tangential velocity in the rotor exit flow which increased near the outer duct wall was involved.

Narrowband sound power spectra calculated from the far field microphone data are presented and the prominent features of these spectra are attributed to various noise generating mechanisms. At 60, 70, and 80% of design RPM, the spectrum peaks at 1, 2, and 3 times blade passing frequency are caused by inlet distortion/rotor

interaction. At 90% RPM the steady rotor field is dominant at blade passing frequency. The rotor/stator interaction mechanism described above is the source of a substantial broadband peak centered at about 2.2 times blade passing frequency for all RPM's. The remaining broadband energy between 0.3 and 3.5 times blade passing frequency is attributed to the better known rotor/stator interaction source associated with rotor wake turbulence.

If the QF-1B fan were used on an aircraft engine, the noise at multiples of blade passing frequency should be reduced in forward flight at the lower RPM's due to reduced inflow distortion and turbulence. The other spectrum components would not be substantially affected by forward motion.

SECTION 1
INTRODUCTION

For some years a major element in NASA's Quiet Engine Program was the full scale quiet fan test facility at NASA-Lewis. With its 37,000 horsepower electric motor, propulsion type fans having diameters of 1.83m (6 ft) can easily be driven at tip speeds, pressure ratios, and weight flows typical of fans in modern, high bypass engines. Early in the program, however, it was recognized that rig induced flow distortion was influencing fan noise (ref. 1). Various modifications to the support structure were incorporated resulting in the configuration shown in figure 1 which was used for the tests reported herein. Later on, through research at Hamilton Standard (refs. 2, 3, 4) and elsewhere, it became clear that atmospheric turbulence and ground vortices are also significant noise producing sources of flow distortion in static (zero forward speed) test facilities.

In order to evaluate various noise generating mechanisms in the NASA QF-1B fan, pressure transducers were installed on the fan rotor blades and stator vanes by Bolt, Beranek, and Newman, Inc. of Cambridge, Mass. The fan was run through a range of operating conditions while signals from the transducers and from far field microphones were tape recorded by NASA-Lewis. BBN and Hamilton Standard analyzed portions of the data using electronic signal processing techniques and analytical models of the noise generation processes. The BBN work concentrated primarily on the rotor/stator interaction and their results are reported in reference 5. Hamilton Standard's effort was mainly on the rotor blade pressure data using techniques developed for noise diagnosis of its Q-Fan^{TM} as reported in reference 6. However, some analysis of the stator data was also performed and this led to important conclusions. This report presents results of Hamilton Standard's study of rotor pressure, stator pressure, and microphone signals from the QF-1B fan.

The organization of the report is as follows. Section 2 gives some general background on the nature of flow non-uniformities in fans, their influence on unsteady blade and vane surface pressures, and the resulting noise characteristics. Section 3 describes the test equipment and operating conditions. Section 4 gives the results of inlet flow diagnosis using signals from the rotor mounted pressure transducers which were processed with a special data analysis computer program developed for this purpose. Section 5 documents a relatively unknown source of rotor/stator interaction which appears to be important for fan designs departing significantly from free vortex flow near the outer duct wall. In Section 6 results of the noise source diagnosis are given in which another computer program is used to compute the far field noise spectrum from the spectrum of the measured blade pressure. Section 7 summarizes the conclusions of the study.

SECTION 2
BACKGROUND
GENERAL COMMENTS ON NOISE MECHANISMS AND DIAGNOSTIC METHODS

Figure 2 illustrates the noise generating mechanisms which were studied for this report relevent to the QF-1B fan. In the inlet turbulence/rotor interaction process shown at the left, the local terrain and weather conditions produce ambient turbulence through thermal action and wind. As this turbulence is drawn toward the rotor, it is stretched by the sink-like inlet flow. The turbulence interacts with the rotor causing unsteady blade pressures. These pressures act as acoustic dipole distributions which radiate noise to the far field. Similar comments apply to the inlet distortion/rotor interaction and rotor wake/stator interaction processes shown at the center and right in figure 2.

For noise diagnosis purposes, it would be desirable to have calculation procedures for each of the steps indicated in figure 2. However, for the first steps (through the blade and vane pressure response calculations, the state of the art is not adequate to produce reliable calculations with the detail needed for noise analysis. Fortunately, the last step of noise radiation caused by the blade and vane pressures requires acoustic calculations (as opposed to the previous aerodynamic calculations) for which good formulations are available. With this difficulty in calculating internal flows, it becomes desirable to make measurements at one of the intermediate steps shown in figure 2. The blade and vane surface pressures measured for this study were a good choice for two reasons: Firstly, in any acoustic radiation theory these surface pressures <u>are</u> the acoustic sources. And secondly, the temporal and statistical behaviors of the pressure signals help identify the sources of unsteady flow and their relative importance.

Since the narrowband spectrum is the most common type of statistical analysis used in noise diagnosis, it is appropriate to review the features of blade and vane pressure spectra and noise spectra which are peculiar to the three noise mechanisms discussed above. These features, which are all well known from the literature, are summarized in figure 3. In general, pressure transducers on a rotor blade pass through the inlet distortion pattern once per revolution. Thus, the prominent blade pressure frequencies caused by inlet turbulence and steady inlet distortion are the rotor shaft frequency and its multiples. If the inlet distortion is truly steady, then it causes purely harmonic blade pressures with no random components. The inlet turbulence, however, is random and tends to include a long length scale component, which gives rise to narrowband peaks in the blade pressure spectrum, and small scale components, which cause broadband noise (refs. 3, 4). The corresponding noise spectra at the right in figure 3 show that, for both inlet turbulence and inlet distortion, the basic frequency is blade passing frequency. The rotor wake/stator interaction spectra are shown at the bottom in figure 3. The basic frequency for the stator pressure is BPF because B wakes per revolution impinge on each vane. Since the wakes are turbulent, there is also a broadband

component in the stator pressure spectrum. If the turbulence in the rotor wakes is not correlated from wake to wake, then the spectrum peaks have zero bandwidth (ref. 7). The noise spectrum for rotor/stator interaction shown at the bottom right in figure 3 generally has the same characteristics as the vane pressure spectrum. The major exception is that for the QF-1B, the number of blades (53) and the number of vanes (112) have been chosen for cutoff in the sense of the Tyler-Sofrin spinning mode theory (ref. 8). Thus, in the noise spectrum, the blade passing frequency peak is greatly reduced whereas the higher harmonics are not. (The stator noise studied in Section 5 has a component which departs from the classic model described here.)

The proceeding discussion has shown that, although the noise spectra for all three mechanisms under consideration are similar in general, they are different in detail. One of the purposes of this study was to exploit these detailed differences to help identify the dominant noise generating mechanisms. For example, the peak in the noise spectrum at blade passing frequency must come from the rotor because the stator radiation is cut off. However, we hope to distinguish between steady distortion (caused, for example, by test rig or ground interference) and random inlet flow (from atmospheric turbulence) by use of special analysis techniques developed for this purpose in conjunction with the Hamilton Standard Q-Fan program (ref. 6).

SECTION 3
DESCRIPTION OF TEST

This section describes the test facility, the test fan, and the fan instrumentation used in the study. Since detailed descriptions are available in the references, only the most important features are presented here. The test conditions are listed at the end of this section.

Test Facility

The tests were performed at the NASA-Lewis Research Center on the full scale quiet fan test facility. The original configuration of this facility was described by Leonard, et al (ref. 9) and modifications for cleaner inlet flow were described by Povinelli and Dittmar (ref. 1). A plan view of the test area in figure 4 shows the 1.83m (6 ft) diameter fan installed 33.5m (109.8 ft) from the drive motor building. Microphones are located every 10 degrees on a 30.5m (100 ft) radius arc at the fan centerline height of 5.8m (19 ft). Figure 1 shows the front drive, long shaft configuration used for the tests reported herein.

Since the ground surface between the fan and microphones is paved with asphalt, acoustic reflections do interfere with the direct radiation from the fan. However, since the first cancellation is at approximately 80 Hz, ground reflection is not expected to affect spectrum shape at frequencies in the vicinity of blade passing (2700 Hz) and above. The wall of the drive motor building has absorptive treatment to minimize reflections from that surface.

Test Fan

The test fan was the NASA QF-1, which is designated QF-1B in the front drive configuration. It is typical of modern technology, low noise designs in that blade and vane numbers were chosen for acoustic cutoff, the rotor/stator spacing is large, and the tip speed is low. The fan design is described in reference 9 and detailed aerodynamic measurements on a scale model of the QF-1 are given in reference 10. Design features are summarized in the table below.

QF-1 Design Features

Rotor Diameter, m (in.)	1.83 (72)
Design Pressure Ratio	1.5
Design Tip Speed, m/sec (ft/sec)	338 (1110)
Design Weight Flow, kg/sec (lb/sec)	396 (873)
Number of rotor blades	53
Rotor chord (constant) m (in.)	0.139 (5.49)
Rotor solidity, tip (hub)	1.34 (2.56)
Number of stator vanes	112
Stator chord (constant), m (in.)	0.0683 (2.69)
Stator solidity, tip (hub)	1.40 (2.39)
Axial spacing between rotor and stator, rotor chords	3.6

Fan Instrumentation

Piezolectric pressure transducers were manufactured and installed on the blades and vanes of the fan by Bolt, Beranek, and Newman, Inc. (BBN). In all, 24 transducers were installed as described in reference 5. However, only the 3 rotor transducers and one stator transducer at locations given in figure 5 were used for this study. These were flush mounted so as to measure unsteady surface pressures. According to BBN, the sensing area of the transducers is 5.6mm (0.22 in.) in diameter and their frequency response is flat within $\pm$ 1 dB from 10 Hz to 10 kHz. Pressure signals from the rotor were recovered via a rotary transformer at the aft end of the fan. Signals from the pressure transducers and far field microphones were FM recorded simultaneously by NASA on 14 track magnetic tape systems. These tapes were re-recorded by NASA with frequency response compensation to reduce the low frequency roll-off of the rotary transformer. The compensated data tapes were sent to Hamilton Standard where they were processed with various analog and digital systems described elsewhere in this report. Details of the record/playback characteristics of the data system are given in Appendix A.

Test Conditions

Data for two front driven configurations were studied:

Condition 401 - Unobstructed inlet
Condition 403 - Blockage plate in inlet

For both tests the wind was under 7 knots. The blockage plate is shown installed in figure 6. Test conditions listed below were studied:

Configuration	Nominal % RPM	RPM	Rotational Tip Speed		Blade Passing Frequency
401	60	2053	197 m/s	645 ft/s	1813 Hz
	70	2396	229	753	2116
	80	2738	262	860	2418
	90	3080	295	968	2720
403	60	2066	198	649	1825
	70	2413	231	758	2131
	80	2757	264	866	2435
	90	3102	297	975	2740

SECTION 4
INLET FLOW DIAGNOSIS

Pressure signals measured on rotating blades are of obvious value in studies of blade vibration and acoustic radiation. However, by use of a computer system developed for plotting blade pressure waveforms and measuring blade pressure statistics, these signals can also be used to study the structure and sources of nonuniform inflow as described in this section. One objective of this portion of the study was to evaluate the relative importance of sources of inlet distortion such as the fan support structure and atmospheric turbulence.

The locations of the rotor-mounted pressure transducers were shown in figure 5. The transducers were all on blade number 2 (RII) approximately 2.5cm from the leading edge. Transducer A1P was on the pressure side of the blade approximately 2.5cm from the tip. A1S and C1S were on the suction side 2.5cm and 7.5cm from the tip, respectively. In fan Configuration 401 the inlet was aerodynamically clean and symmetrical; in Configuration 403 a blockage plate was installed as shown in figure 6 to produce a pronounced increase in far-field noise and in blade pressure.

To help understand sources of non-uniform inflow, streamlines were traced from the transducer radii at the rotor face upstream to the point where obstructions exist in the inflow. The streamlines demonstrating this in figure 7 were adapted from propeller potential flow calculations which assume axisymmetric geometry and thus are approximate. However, it is clear that the flow interacting with the blade tips comes from behind the inlet lip where the support structure must be located. Thus, installing the fan in the "turn-around" or rear drive mode would not be expected to improve the flow over the blade tip region.

Overall Blade Pressure Behavior

Gross trends in measured blade pressure are shown in figure 8 which gives overall RMS blade pressure for the 3 transducers versus RPM with and without the blockage plate. Except for transducer A1P, the trends are generally as expected with RMS pressure increasing with RPM and increasing with the blockage plate. A1P, however, shows practically no increase with RPM and no increase due to the blockage plate. Since this behavior may be caused by transducer problems, the remainder of the study will concentrate on transducers RII/A1S and RII/C1S.

Results from Configurations 401 and 403 in figure 8 indicate that the gross effect of the blockage plate is to increase blade pressure levels by 3 to 9 dB. Perhaps a more revealing way to view this result is that, when this very severe blockage is removed,

the blade pressure levels drop by a factor of only about 4. This gives a rough idea of the magnitude of the distortion caused by atmospheric turbulence, crosswind effects and rig interference which set the remaining blade pressure levels.

It is interesting to compare these results with similar data from the Hamilton Standard Q-Fan Demonstrator engine tested on an outdoor test stand in 1973. Blade pressures for a clean inlet which were reported in reference 6 are shown in figure 9. The clean inlet results from figure 8 are repeated for comparison. It is seen that the levels are similar despite major differences in rotor design and test facilities. In the Q-Fan the tip signal was larger than the mid blade signal whereas for the QF-1B the opposite behavior occurred. No special significance is attached to this because the transducers were on opposite faces of the blades and the duct boundary layers could be significantly different.

Review of Waveform Analysis System

Although the blade pressure analysis system used in this section has been described previously in the literature (refs. 6, 11), its basic principles are simple enough to review here. To consider blade pressure waveform plots as inlet distortion space-time histories, the waveforms recorded with the flow blockage shown in figure 6 are presented first. The instrumented blade passes through the wake of the blockage plate once per revolution producing a once per revolution blade pressure pulse. Signal waveforms from transducers RII/A1S and RII/C1S are shown as the upper and lower plots, respectively, in figure 10. Each trace in these plots represents the pressure signal during one revolution, starting and ending as the instrumented blade passes through the top of its rotation. Fifty traces from 50 consecutive revolutions are shown. On each channel, the effect of the blockage plate is clearly visible at rotor angles between 180° and 270°. Thus, the waveform plotting technique accurately shows the location of the inlet disturbance in the circumferential sense.

In order to generate figure 10, the analog data tapes supplied by NASA were digitized at Hamilton Standard using a clock signal from a frequency multiplier which generated exactly 150 equally spaced pulses for each pulse of the once-per-revolution (1E) sync signal. The 150 clock pulses caused the blade pressures to be digitized at 150 angles of rotation. Because the clock output is phase-locked to the 1E signal, the samples are taken at the same locations in the inlet during each revolution. For example, sample number 75 is always taken as the blade passes through 180°.

This digitizing system allows the computer to perform statistical operations on the 150 data points as if they had been acquired from 150 hot wire anemometers fixed around the circumference. For mathematical manipulation, the samples from the mid blade transducer (RII/C1S) are labeled $p_{m,n}$ where the subscript m identifies the number of the revolution and n counts the sample (or angle) during that revolution starting

with n = 1 at the top of the fan. The blade tip signals (transducer RII/A1S) are labeled $q_{m,n}$. The index m runs from 1 to M, the number of revolutions analyzed, and n runs from 1 to N, the number of samples per revolution. For the first statistical analysis, the system computes the average, or signal enhanced, waveform according to

$$\bar{p}_n = \frac{1}{M} \sum_{m=1}^{M} p_{m,n} \tag{1}$$

which is plotted after the instantaneous waveforms in figure 10. The effect of the blockage plate wake extends over considerably greater circumferential distance than does the plate itself. This is due partly to the spreading of the wake and partly to the fact that the airfoil continues to respond even after it has passed out of the wake.

The last traces on the right in figure 10 are the standard deviations of the signals computed in the streamwise direction,

$$\sigma_{pn} = \left[\frac{1}{M} \sum_{m=1}^{M} (p_{m,n} - \bar{p}_n)^2 \right]^{1/2} \tag{2}$$

which are an indication of the distribution of turbulence around the circumference. Later in this section enlarged plots of $\bar{p}_n$ and σ_{pn} will be shown to compare the levels of steady and unsteady inlet distortion.

Blade Pressure Waveforms with Unobstructed Inlet

Now that the general behavior of blade pressure signals caused by an intentional flow disturbance has been explained via the waveform plots, it is appropriate to examine similar plots for the clean inlet cofiguration. These are shown for 60, 70, 80, and 90% RPM in figures 11, 12, 13, and 14. In each case, 600 revolutions are shown corresponding to between 12 and 18 seconds of operation, depending on RPM. As was found with the Hamilton Standard Q-Fan (ref. 6), the waveform plots show the inlet flow to be random but with narrow, highly persistent disturbances which can exist in the inlet for hundreds of revolutions. These disturbances are highly effective for generating a tone-like rotor noise component because (1) being narrow, they led to propagating acoustic modes and (2) being long, they are chopped by so many blades that the noise spectrum peaks are very narrow at multiples of blade passing frequency. A characteristic not found with the Q-Fan, however, is that the distortion activity is concentrated near the bottom of the inlet. There, the blade pressure pulses are strong, persistent, and cover roughly 5% to 10% of the circumference. At the top of the inlet, the pulses are weaker, less persistent, and narrower.

Frequently, several distinct disturbances can be found at once. This is particularly obvious in figure 12 which suggests 4 or 5 vortices streaming from the fan support structure. In figure 12 it can also be seen that similar patterns appear on both transducer signals. Thus, the radial scale of the inflow disturbances is at least as big as the spacing between transducers (5cm or 2 in.). However, the individual pulses in the waveforms seem to have opposite signs. This, and the crosscorrelation coefficient of the two signals (not shown here) suggest that they were recorded with opposite polarity.

Figure 11 shows an interesting result on the tip transducer signal. Disturbances which enter the rotor at the side or top tend to migrate toward the bottom by the shortest route before losing their identity. A similar effect was noted in the Q-Fan tests but the migration was always in the direction of rotor rotation.

Circumferential Distribution of Inlet Distortion

The preceeding discussion of inlet flow distortion was based on qualitative inspection of the blade pressure waveforms in figures 11 through 14. A more quantitative assessment can be made through the use of the signal enhanced waveforms and standard deviation distributions described above with reference to equations 1 and 2 and figure 10.

If it is accepted that the blade pressure waveform is a measure of inlet distortion (through a blade pressure response function), then the distortion can be separated into steady and unsteady components as follows. The steady part, represented by the signal enhanced, or averaged waveform, $\overline{p}_n$ is that portion of the distortion which does not vary from revolution to revolution. The unsteady part, represented by the standard deviation σ_{pn} of the waveform is that portion of the distortion which varies from revolution to revolution with zero mean value. Thus, at each circumferential location, designated by the sample number n, the mean square pressure is the square of the mean plus the variance $\overline{p}_n^2 + \sigma_{pn}^2$. Through this idealization, it is hoped that the steady distortion can be related to fixed geometrical items such as the fan support structure.

A typical plot of $\overline{p}_n$ and σ_{pn} averaged over 3000 revolutions is shown at the top in figure 15. The most important implication of this figure is that the unsteady distortion σ_{pn} is far larger than the steady distortion, particularly near the bottom of the inlet. Secondly, the steady part of the flow p_n is distorted about equally around the circumference whereas the unsteady distortion is concentrated near the bottom.

The σ_{pn} curve is replotted at the bottom in figure 15 where it is interpreted in terms of sources of inlet turbulence: At the top of the inlet the level is set by atmospheric turbulence and any shroud boundary layer effects (negligible for mid-blade transducer). These sources are assumed to be uniformly distributed around the circumference and the associated level is labeled the symmetric portion of the inlet turbulence distribution. In the absence of significant cross wind, any level above this

can be attributed to the fan support structure. Thus, it appears that the fan support structure is roughly as important as atmospheric turbulence in generating random inflow. Therefore, to make a significant improvement in rotor noise, both sources would have to be reduced. Figures 16 and 17 show similar results for the other transducer and all four RPM's. Finally, figure 18 shows the effect of the blockage plate. The mean pressure is increased substantially to the point that it is larger than the standard deviation and is localized to the vicinity of the plate location.

Periodicity of Blade Pressure and Noise Signals

One of the original motivations for this study was the hope that the source of the spectrum peaks at 1, 2, and 3 times BPF could be deduced from the periodicity of these spectral components. The idea was that the periodic component would be associated with a truly repetitive process such as rotor/stator interaction and that the random part of these spectrum peaks would be attributable to inlet turbulence. Although it was just shown that the blade pressure signals are mostly random, it still remains to check that result as a function of frequency.

The desired frequency distribution information is displayed in plots typified by figure 19. The same plotting system is used later for both microphone signals and stator pressure signals. The upper spectrum curve, labeled PSD, was calculated by a process equivalent to the following steps (ref. 6):

1. Digitize waveforms for many revolutions giving samples, $p_{m,n}$ where m counts revolutions from 1 to M and n counts samples within a revolution from 1 to N.

2. For each revolution find the Fourier coefficients

$$A_{bm} = \frac{2}{N}\sum_{n=1}^{N} p_{m,n} \cos\left(\frac{2\pi bn}{N}\right)$$

$$B_{bm} = \frac{2}{N}\sum_{n=1}^{N} p_{m,n} \sin\left(\frac{2\pi bn}{N}\right) \qquad (3)$$

for the harmonics of shaft frequency b=1, 2,---, N/2-1.

3. Calculate $S_{bm} = \frac{1}{2}(A_{bm}^2 + B_{bm}^2)$ representing the mean square energy in harmonic b for revolution m.

4. Average S_{bm} over many revolutions, giving

$$S_b = \frac{1}{M}\sum_{m=1}^{M} S_{bm} \qquad (4)$$

The sum of the harmonics S_b is the mean square value of the signal and the plot of S_b versus b is labeled PSD because it shows how the power (mean square value) is distributed over frequency. It is a crude measure because the frequency scale has only one point per E order.

The lower curve labeled HAR in figure 19 is obtained via the following steps.

1. From digitized waveforms, calculate signal enhanced waveform, $\bar{p}_n$.

2. Find Fourier coefficients of $\bar{p}_n$ according to

$$A_b = \frac{2}{N} \sum_{n=1}^{N} \bar{p}_n \cos\left(\frac{2\pi bn}{N}\right) \tag{5}$$

and

$$B_b = \frac{2}{N} \sum_{n=1}^{N} \bar{p}_n \sin\left(\frac{2\pi bn}{N}\right) \tag{6}$$

3. Plot $H_b = \frac{1}{2}\left(A_b^2 + B_b^2\right)$

This represents the frequency distribution of the periodic portion of the waveform. Thus, the area under the PSD curve adds up to the entire signal energy whereas the area under the HAR curve includes only the energy of the periodic portion of the signal.

To interpret figure 19, it must first be decided what blade pressure frequencies are of interest. Since the blade pressure harmonics correspond to inlet distortion harmonics, duct acoustic theory can be used to find the range of these harmonics which lead to propagating duct modes at blade passing frequency. The values, calculated in Appendix B, are shown on the abcissa in figure 19 to lie between 8 and 98 for 80% RPM. In this frequency range the periodic portion of the signal (HAR) is at least 10dB below the spectrum of the overall signal (PSD). Thus, distortion induced noise at blade passing frequency should be essentially all random at 80% RPM. Figures 20 and 21 show similar curves for two rotor transducers and four RPM's. However, at 90% RPM, even the lowest frequency blade pressure harmonics couple to propagating modes. Since the distortion is mainly steady at these low orders, we can expect some harmonic rotor noise at BPF due to inlet distortion at 90% RPM. Also, it should be noted that the rotor steady field is cut on at 90% RPM.

Figure 22 compares the digitally generated spectra with and without the blockage plate. The only significant effect of the plate is to increase the periodicity of the signals at frequencies below about 20E.

The spectrum plotting system described above can be used with microphone signals to study the periodicity of far field noise at multiples of blade passing frequency. Examples are shown in figure 23 for inlet and aft quadrant microphones at 60% and 90% RPM. The true harmonic components are below the spectrum peaks by increasing amounts at higher multiples of BPF. The 60° mic at 90% RPM shows the most periodic behavior at BPF but even this harmonic peak is 10dB below the overall PSD at that frequency.

Thus, the harmonic contribution which was expected from the rotor steady field and the low order distortion harmonics failed to materialize and the value of signal enhancing for deducing noise sources in turbofans now appears questionable. It seems that a noise component which is periodic at the source may lose its periodicity in propagation to a far field microphone. To survive the signal enhancing process, a signal must remain "phase-locked" to the rotor rotation. For example, when recording a sine wave, if the phase shifts by 1/2 cycle halfway through the recording, signal enhancing will yield zero level. At wavelengths corresponding to blade passing frequency (~15cm), this phase cancellation may occur in the highly turbulent inlet flow or in propagation because of small wind variations.

Finally, samples of the far field microphone signal waveforms are shown in figures 24 and 25 to illustrate further their lack of periodicity. The 60% RPM condition given in figure 24 occasionally shows a 53E characteristic as for example, in revolution number 6 near the top of the figure for the 50° mic. However, at revolutions 44 and 45 an example is shown where the 53E components cancel on successive revolutions. The 60° mic at 90% RPM in figure 25 shows a far stronger 53E component. However, the lack of phase coherence can be seen by checking the polarity of the pulses at the top edge of the plot. The aft quadrant noise shown at the bottom in figure 25 shows less of the 53E component. In fact, the higher characteristic frequency which appears (about 117E) is the subject of the next section of this report.

Conclusions from this section and others are summarized in Section 7.

SECTION 5
ROTOR/STATOR INTERACTION - A DEPARTURE FROM THE CLASSIC MODEL

As described in Section 2, the well known sources of noise in subsonic tip speed fans lead to far field noise spectra with peaks at multiples of blade passing frequency plus a smooth broadband component. The narrow band sound power spectra for the QF-1B shown in figure 26 generally show this behavior except for a substantial additional "haystack" centered at about 2.2 times blade passing frequency and smaller humps at 3.2 and 4.2 BPF at 60% and 70% RPM. Because of the breadth of the 2.2 BPF hump and the frequency at which it occurs, it makes an important contribution to the fan noise annoyance. This report section presents a brief study of this spectrum component.

Documentation of the 117E Spectrum Component

Since it appears in figure 26 that the haystack occurs at approximately the same harmonic of shaft frequency (E order) over the full RPM range, the remaining spectra in this section are plotted versus E order rather than frequency. For example, in the noise spectrum shown at the top in figure 27 the haystack frequency is found to be approximately 117E. Since the stator pressure spectrum shown at the bottom in figure 27 exhibits the same behavior, a cause and effect relationship is immediately assumed. This is further verified in figure 28 which shows the 117E haystack in the stator pressure and microphone spectra at 60, 70, 80, and 90% RPM. Because of its independence of RPM, this effect cannot be caused by resonant structural vibration. Figure 29 shows spectra of the same signals at 60% and 90% RPM calculated with the digital system described in Section 4. These demonstrate that there are no components in the haystack which are phase locked to the rotor rotation.

Waveforms of the stator pressure which are shown in figure 30 exhibit a curious behavior: the stator pressure (presumably responding to the rotor wake) oscillates sometimes at the expected 53E rate but more often at the 117E rate. Similar behavior can be found in the lower sections of figure 24 and 25 which give the corresponding far field noise waveforms. This intermittent switching of frequencies is suggestive of an instability in the rotor exit flow.

Non-uniformities in Rotor Exit Flow

It seems clear that the 117E noise component is caused by a strong stator pressure component at 117 times the shaft rotation frequency. Also, it is likely that these pressures are excited by non-uniformities in the rotor exit flow because there is no evidence of structural resonance. However, no mechanism has been found which would satisfactorily explain a 117E component in the exit flow of a rotor with 53 blades. The only

related work of which the author is aware is that of Professor J. L. Kerrebrock and his associates at the Massachusetts Institute of Technology Gas Turbine Lab. (refs. 12, 13). This is discussed briefly here as it provides clues for further study of the phenomenon.

Kerrebrock's test compressor includes a transonic rotor with 23 blades and no stator. References 12 and 13 present analytical and experimental studies of the swirling flow which exits the rotor and develops in the downstream annulus. In one series of measurements, Mach number distributions were mapped behind the rotor. Close to the rotor (0.1 chord), the flow showed the expected 23E frequency. However, 1 chord downstream of the rotor the frequency shifted to 16E in the outer annular region ($r > 0.8 r_t$) while remaining at 23E for $r < 0.8 r_t$. Kerrebrock feels this downward frequency shift is probably caused by a characteristic of the mean tangential velocity distribution behind the rotor. In his analytical study of swirling annular flow (ref. 12), Kerrebrock derived differential equations describing the behavior of small disturbances via a linearized analysis. He found that, if the mean tangential velocity increases with radius, the flow can support shear waves with a number of oscillations around the annulus which is determined by the boundary conditions. Since the number of oscillations predicted for the MIT compressor was very nearly 16, this seemed to provide a satisfactory explanation for Kerrebrock's test results.

Because the tangential Mach number distribution for the QF-1B also increases with radius near the outer duct wall, this was investigated as a possible explanation for the 117E haystack in the noise and stator pressure spectra. Figure 31 at the top shows design calculations for the QF-1B rotor exit tangential Mach number distribution. In the region outboard of the 93% radius, which behaves approximately like wheel flow, the fundamental shear mode would be the cellular vortex pattern sketched at the bottom in figure 31. To find how many vortices are in the array, Kerrebrock (in a personal communication) suggested use of the simplified analysis of reference 13. He assumes the spacing at the mean radius ($r = 0.965R$) to be equal to the vortex diameter, $0.07R$. Thus, the approximate number of vortices is $N = 2\pi r/0.07R = \frac{2\pi \times 0.965}{0.07} \approx 86$. Since the vortices alternate in direction of rotation, a pair of vortices constitutes a period in the disturbed flow with $m = N/2 = 43$ cycles per duct circumference. Because the pattern is nearly convected with the mean flow in the same sense as the rotor viscous wakes, the expected frequency of stator excitation would be 43E. Therefore, this mechanism does not provide a direct explantion for the 117E component. Nevertheless, it is still possible that the upturned swirl Mach number distribution is related,as suggested by the scale model results which follow.

Scale Model Results

A 27.7% scale model of the QF-1B has been tested in a compressor performance facility and in the General Electric anechoic chamber. An example of noise test results reported by Gelder and Soltis (ref. 14) is reproduced in figure 32. The anechoic chamber data has a spectrum peak at 102E which is possibly evidence of the same phenomenon which caused the 117E haystack in the full scale fan. The downward shift in frequency could be a Reynolds number effect.

The haystack is absent in the noise data from the compressor performance facility as shown in the bottom curve of figure 32. Since inlet air was drawn from a plenum, the inlet velocity profile undoubtedly was different near the outer wall. This difference is reflected in measurements of the rotor exit swirl velocity which are plotted in figure 33. Since this distribution does not have the upward hook near the outer wall which was calculated for the full scale fan in figure 31, it seems that the tangential velocity distribution may have an important influence on rotor/stator interaction noise.

Recommendations

Because the spectral behavior reported here is not often observed in turbofans, it might seem that these are isolated results. However, it may be that what we have observed here is a well organized version of a more generally occurring flow phenomenon. That is, in the QF-1B, the spectral peak at 117E was easily identified because of its narrow bandwidth while in other fans the phenomenon may appear as a more nondescript broadband component. Since the radial distribution of swirl velocity is largely dictated by the radial distribution of rotor loading, the designer has some control over it. Therefore, it is recommended that the rotor exit flow of the QF-1B or its model be explored with fast response instrumentation to discover the structure and origin of the 117E flow component as a function of measured mean velocity distributions.

The simplest approach would be to use a traversing hot wire or hot film probe which could be placed at each of several axial locations between rotor and stator. Significant variations in the swirl velocity distribution can be achieved by varying the nozzle exit area: increasing the nozzle area will increase the slope of the swirl velocity distribution to the point where the upturn at the outer wall may disappear. Decreasing the nozzle area should aggravate the upturn. Documentation of the behavior of the 117E flow component and the rate of decay of the 53 rotor wakes should provide guidance for further experimental and analytical work as well as possible design guidelines.

SECTION 6
DIAGNOSIS OF FAN NOISE SOURCES

The objective of this report section is to establish the dominant noise generating mechanisms for the QF-1B fan operating on the full scale fan test facility at NASA-Lewis at 60, 70, 80 and 90% of design RPM. The results will be explained with reference to prominent features of the measured narrowband sound power spectra. One feature (the 117E haystack) has already been diagnosed. The remaining analytical task is to establish how much of the radiated sound power can be attributed to interaction of the rotor with inlet turbulence and distortion. This will be accomplished by use of an aeroacoustic theory which predicts narrowband sound pressure and sound power spectra from measured blade pressure spectra. In the following subsections this theory is reviewed and then applied to the QF-1B data.

Review of Acoustic Theory for Inlet Turbulence/Rotor Interaction

The main strength of the subject acoustic theory is that it starts from measured blade pressure statistics and thus avoids the difficult calculation of turbulence properties and blade pressure response required by other analyses. The derivation of the theory has been published in references 4 and 6. Therefore, only a review of the assumptions and results is given here. Statistical parameters specific to the four operating conditions of the QF-1B are given in Appendix C. The reader interested in details will find that between Appendix C and reference 6 all the information needed to reproduce the rotor noise calculations is given.

The central concept of the procedure for calculating the spectra of blade pressure and sound pressure due to interaction of the rotor with inlet turbulence is that the turbulence consists of discrete eddies. Thus, in principle, the flow could be observed for a long period of time and the eddies could be counted and categorized as to their length, width, point of entry on the rotor disc, and any other variables of interest. The observed values of these variables would be sets of random numbers whose statistical properties are given by their joint probability density function. In practice, it is not the eddies themselves which are observed but the blade pressure waveform which results from interference of the rotor blade with the eddies. The statistical property of the waveform measured is its spectrum rather than a probability density function. The statistics are in terms of time and space variables rather the more frequently used Fourier transform variables of frequency and wavenumbers.

Derivation of the spectrum equations requires the following steps. A form is chosen for the pressure pulse in the rotor disc due to a blade chopping an eddy one time. From this the associated far field pressure pulse is calculated. If the eddies are counted by the index v, the blades by u, and the successive chops (once per revolution) by m, then the Fourier transform of the acoustic pressure pulse can be designated P_{vum}.

It remains then to choose a joint probability density function for the statistical variables (i.e., formulate the statistical model) which has enough generality to fit a wide variety of flow conditions. Then the power spectral density of the sound pressure is computed from

$$G_s(\omega) = \lim_{V\to\infty} \frac{2\pi N}{2(V+1)T} \overline{\left| \sum_{-V}^{V} \sum_{u=1}^{B} \sum_{m} P_{vum} \right|^2} \tag{7}$$

where N/T is the average number of eddies per revolution entering the rotor. An analogous expression exists for the PSD of blade pressure. Since (2V+1)T/N is the time for entry of 2V+1 eddies, equation (7) is read "the power spectral density equals the limit as time goes to infinity of the expected value (ensemble average) of the energy spectral density per unit time". Finally, it must be noted that for signals with extremly narrowband components such as fan noise, it is not practical to measure the power spectral density without bias because the PSD peaks and the filters have about the same bandwidth. The best solution for comparing experimental and theoretical spectra is to analyze the theoretical PSD with a set of mathematical filters whose characteristics match the electronic spectrum analyzer used with the test data. Then in the diagnosis process, filtered spectra are compared rather than PSD's.

In the practical application of equation (7) the following simplifications have been made. The open source Green's function is used so that the effects of duct boundaries and mean fluid motion are ignored. This approximation may be rather poor at any specific directivity point but it should be satisfactory for sound power, as the theory is used here. The blade pressures are assumed to act on a disc in the plane of rotation so that the source is acoustically compact in the axial direction. The chordwise pressure distribution on the blade disc caused by any eddy is taken to be triangular with the peak at the leading edge. The radial pressure distribution has a pulse-like shape whose span is chosen to be the same, on the average, as the circumferential eddy size. This accounts for the fact that the spanwise correlation length of blade pressure is a function of frequency. However, for the acoustic radiation due to a given eddy, the source pressure distribution is taken to be compact in the radial direction.

The turbulence properties are handled through blade pressure pulse statistics. Long eddies are chopped by many blades, producing narrowband random (or tone-like) spectrum components which appear at blade passing frequency harmonics in the noise and at shaft rotation frequency harmonics in the blade pressure. Short eddies are chopped only once, producing a smooth, broadband component. The pulse statistics are quite general with many adjustable parameters. Their validity is demonstrated by forcing a satisfactory fit between measured and theoretical blade pressure spectra. If the narrowband blade pressure spectra agree well, then the narrowband sound power spectra should be well predicted.

System Calibration

The system just described attempts to predict noise from pressure measured at just one point on the blade surface. Thus, its accuracy depends on assumptions regarding pressure distributions over the blade surface. This was overcome in the Hamilton Standard Q-Fan studies (ref. 6) by a "calibration" scheme in which the inlet flow was intentionally disturbed to cause a strong increase in the tone components of blade pressure and noise. Then a calibration constant (an effective chord) was derived via a simple inlet guide vane noise theory with the knowledge that blade pressure and noise bore a clear cause-and-effect relationship.

It was intended to use the same calibration scheme for the QF-1B with the blockage plate data. However, it was found at the frequency of interest (53E) that the blockage plate produced only broadband contributions to the noise and blade pressure as shown in figure 34. An alternative scheme was attempted in which the same inlet turbulence noise theory described above was used to match blade pressure spectra and noise spectra for the 10° microphone. The result shown in figure 35 appears quite satisfactory. However, the ratio of effective chord to blade chord derived from this exercise was only 0.2 (versus the 0.7 found from the Q-Fan studies) and the noise predictions using this calibration constant for the clean inlet conditions were clearly too low. For example, the blade passing frequency spectrum peak, which must be caused by inlet distortion at low RPM because of duct cutoff, was underpredicted by 10 to 15db.

The reason for this failure probably is related to the asymmetry (in a statistical sense) of the inlet flow. The localized blockage causes a noise directivity pattern which is not symmetric with respect to the fan axis of rotation. The theory correctly handles this condition for sound power calculations but not for sound pressure. Since it was not practical to measure noise all over a hemisphere surrounding the fan, the true sound power cannot be accurately known. And since the plate blockage and the natural blockage from the support structure occurred at different azimuths in the inlet, sound pressures from the two configurations could not be related. The analogous problem

in the Q-Fan studies was overcome by using an on-axis microphone and absorptive material on the ground to suppress reflections of sound radiated at an angle from the axis. Thus, by working with an on-axis microphone, a more reliable calibration was achieved. Also, the inlet turbulence and distortion were more nearly uniform circumferentially for the clean inlet condition.

Fortunately, another satisfactory means exists for assigning an absolute level to the rotor noise predictions. Because the rotor steady field and the rotor/stator interaction effects are cut off at the lower RPM's, the levels of the rotor unsteady loading predictions can be set by the spectrum peak at blade passing frequency. The spectrum shape will be determined, as before, by fitting theoretical and experimental shapes of blade pressure spectra. At 90% RPM, the rotor steady field is just cut on and a different argument must be given, as will be seen.

The Sound Power Account

Now the information and techniques developed in the preceeding section can be applied to the process of attributing the important components of the measured sound power spectra to various noise generating mechanisms. This results in what is called here the "sound power account".

The process starts by establishing the level of noise due to unsteady rotor loads via the theory just described. Figure 36 shows how the theoretical blade pressure spectrum was forced to fit test data for the 60% RPM case. (The statistical parameters required for this fit are given in Appendix C.) The fit is quite satisfactory for all harmonics (23E and above) which can couple to propagating duct modes at blade passing frequency and higher. Figure 37 shows how the shapes of predicted sound pressure spectra for rotor radiation compare with measured spectra for all sources. The bandwidth of the peaks and their relative heights are well predicted but the broadband levels are lower relative to the peaks than in the test data. This is shown more clearly in the 60% RPM sound power account in figure 38. Here the level of the inlet distortion/rotor interaction curve was adjusted to match test at BPF and the known 117E haystack from rotor/stator interaction was sketched in. This leaves considerable broadband energy unaccounted for. However, study of the stator pressure spectra in figures 27 and 28 indicates considerable stator broadband pressure in addition to the haystack. Since the haystack phenomenon should occur only locally near the vane tips, whereas the more general broadband pressures should extend from root to tip, it is felt that the remaining broadband components in figure 38 are correctly labeled as rotor/stator interaction.

Figure 39 gives the blade pressure spectrum matches at the higher RPM's. The agreement is seen to be reasonably good for the harmonics which lead to propagating modes except possibly at 90% RPM where even the 1E pressure harmonic contributes. The corresponding "power accounts" for 70% and 80% RPM shown in figure 40 indicate

the same diagnosis just given for the 60% RPM case. However, at 90% RPM the steady field of the rotor appears to make a significant contribution. For this case, the level of spectral contribution from rotor unsteady loading is adjusted to match test data at the third harmonic of BPF to prevent overprediction at lower frequencies.

Conclusions from this portion of the study are summarized in the next section.

SECTION 7
CONCLUSIONS

The purpose of this study was to diagnose inlet flow non-uniformities and sources of noise in the QF-1B fan operating on the NASA quiet fan test facility. Conclusions from the study are given below.

Inlet Flow Diagnosis

A digital data analysis system designed to use signals from rotor-mounted pressure transducers was applied to the QF-1B data with the following results.

1. Blade pressures were recorded with and without a large blockage plate just upstream of the rotor. Because removal of the blockage plate reduced the unsteady blade RMS pressures only slightly, it was concluded that the distortion which was caused naturally by atmospheric turbulence and installation effects was nearly as severe as distortion caused by the intentional blockage.

2. With the blockage plate removed, the remaining inflow distortion was dominated by narrow, highly persistent disturbances similar to those found in earlier Q-Fan studies at Hamilton Standard. Because of their narrowness and length, these disturbances are effective in producing tone-like (narrowband random) noise components at blade passing frequency and its harmonics.

3. The RMS distortion was 2 to 3 times stronger at the bottom than at the top. This is different from the Q-Fan whose distortion was more nearly uniform around the circumference. By tracing streamlines upstream from the blade transducer locations, it was concluded that this additional distortion was caused by the fan support structure which was under the fan behind the inlet lip. From this, it follows that no great noise reduction should be expected from installing the fan in the turn-around mode (rear drive configuration).

4. By use of signal enhancing techniques, the distortion was divided into two components: steady (fixed in space and time) and unsteady. The steady component was more or less uniformly distributed around the circumference and produced relatively low frequency blade excitation. The unsteady distortion component was significantly stronger and produced higher frequency blade excitation. The sources of unsteady distortion were atmospheric turbulence and rig interference. The magnitude of these two sources were roughly equal but rig interference appeared to contribute only at the bottom of the inlet whereas atmospheric turbulence contributed all around the circumference.

5. An attempt was made to use signal enhancing of the far field microphone data to separate truly periodic processes, such as rotor steady loading noise and rotor/stator interaction noise, from random processes, such as inlet turbulence interaction noise. This was unsuccessful apparently because noise signals lose their phase coherence in the process of propagating from the blade through the turbulent inlet and exhaust flows or in the process of propagating from the near field to the far field. Signal enhancing may still be useful for this purpose in fans with fewer blades.

Dominant Noise Sources

Narrowband spectra of sound power were calculated from far field microphone data. The prominant features of these spectra were accounted for as follows.

1. At 60, 70, and 80% of design RPM, the spectrum peak at blade passing frequency was caused by interaction of the rotor with inlet turbulence and distortion. At 90% RPM, the rotor steady field dominates at blade passing frequency.

2. The spectrum peaks at 2 and 3 times blade passing frequency were caused by interaction of the rotor with inlet turbulence and distortion at all RPM's.

3. A noise spectrum peak occurs at approximately 117 times the rotor rotation frequency, or 2.2 times blade passing frequency, at all RPM's studied. Because of its width (about 20 times the shaft rotation frequency) and the frequency at which it occurs, this peak contributes significantly to the annoyance of the fan noise. The peak is caused by stator pressure fluctuations at the same 117E frequency. The source of the stator pressure fluctuations is not known but it may be related to an increase in rotor exit swirl velocity near the duct outer wall. It is recommended that the rotor exit velocity be surveyed the next time the QF-1 (or its model) is on test to determine the structure and source of this high frequency flow component.

4. The remaining broadband energy from about 0.3 times blade passing frequency to about 3.5 times blade passing frequency is caused by rotor wake/stator interaction. Higher frequency broadband noise appears to be caused by inlet turbulence/rotor interaction.

5. If the QF-1B fan were used on an aircraft engine, the noise at multiples of blade passing frequency should be reduced in forward flight at 60, 70, and 80% RPM due to reduced inflow distortion and turbulence. The other spectrum components would not be substantially affected by forward motion.

APPENDIX A
DATA SYSTEM CHARACTERISTICS

Signals from the rotor pressure transducers were transmitted to the stationary tape recording system via a multichannel rotary transformer. Because the transformer frequency response rolled off below 600 Hz, NASA re-recorded the original tapes through a compensating network which boosted the low frequencies. The re-recorded tapes were used in Hamilton Standard's study. This Appendix documents the net frequency response, linearity, signal to noise ratio, and waveform fidelity characteristics of the data system from transducer output through the Hamilton Standard analyzer systems.

Frequency response and linearity are shown in figure 41 which was generated by playing back a NASA test tape through the Hamilton Standard narrowband spectrum analyzer. The test tape was made by injecting sine waves at various frequencies on the rotor side of the transformer and recording them through the frequency compensation system. For the top curve, the sine waves were attenuated 18.1dB below the recorder full scale of 1 volt. Linearity was checked by attenuating the signals further in 10dB steps at 100 Hz, 1 kHz, and 10 kHz. Figure 41 shows that frequency response and linearity are quite good at 100 Hz and above for high recording levels. Because the blade pressure spectra tended to peak at about 100 Hz (or roughly 2E), the compensation system was satisfactory for the diagnostic analyses of this report.

Figure 42 is a demonstration of the signal to noise ratio of the data system. Tapes for these runs were made by recording the data normally for a given test condition and then, without changing any of the recorded gain settings, turning off the test fan and recording the residual noise level. During playback, the "signal" data was analyzed normally and then the "noise" data was analyzed without changing attenuators on the spectrum analyzer. Because the only difference in the system for the signal and noise curves was that the fan was not turning for the latter, the difference in the two curves in a good measure of net signal to noise ratio. Figure 42 shows that the signal to noise ratio was excellent at all frequencies above 2E.

Comparison of the signal curves in figure 42 shows that transducer RII/C1S has many spectrum peaks at frequencies of 30E and higher which do not appear with transducers RII/A1S. This behavior was typical of all RPM's. Because it is likely that this was caused by blade vibration or other effects of rotation, transducer RII/A1S was used for most of the analysis reported.

Because the rotary transformer and compensating network described above modified phase as well as amplitude charactieristics of the blade pressure signals, it was necessary to verify that the waveform plots could be interpreted reliably. This was done as follows. NASA made a test tape by injecting a repetitive pulse from a signal generator at the pressure transducer output and recording the signal as passed by the rotary transformer and compensating network. This was played back and analyzed at Hamilton Standard as if it were a blade pressure waveform. Results for two typical signals are shown in figures 43 and 44. In figure 43 the top plot shows a signal generated from a 400 Hz sine wave by blanking 9 out of every 10 cycles of the wave. This 10% duty cycle simulates pressure response to a flow disturbance extending over 10% of the inlet circumference. This same signal had the appearance shown at the bottom after passing through the transformer and compensating network. The signal was inverted but otherwise the waveform distortion was not severe. The noise on the bottom trace is caused by a low recording level. Similar results are shown for the 6% duty cycle signal in figure 44 but the distortion is reduced. These figures demonstrate that the data system adequately reproduces the width and location of the pressure pulses. Waveform distortion is small enough not to influence any of interpretations in the report.

APPENDIX B
DETERMINATION OF PROPAGATING MODE ORDERS

In order to understand the significance of the blade pressure spectrum plots in Sections 4 and 6, it was necessary to establish what blade pressure harmonics could cause noise. In particular, the low order harmonics were of interest because experimental and theoretical blade pressure spectra were difficult to match in that region. The Tyler-Sofrin theory for spinning modes in circular ducts (ref. 8) shows that, for each blade passing frequency harmonic in the noise, there is a range of blade loading harmonics which produce propagating modes in the duct. For the QF-1B these ranges overlap for the adjacent noise harmonics so it is only necessary to consider the modes at blade passing frequency. This appendix shows how spinning mode theory was used to determine the range of blade pressure harmonics which could couple to propagating modes at each of the RPM's tested.

When the effect of mean flow in the duct is included (ref. 15), the condition for mode propagation at blade passing frequency is

$$B\,M_T \geq \beta\,K_{m0} \tag{8}$$

where B = number of rotor blades

M_T = rotor tip rotational Mach number

$\beta^2 = 1 - M_x^2$

M_x = axial velocity in duct

K_{mn} = duct eigenvalue

m = circumferential mode order

n = radial mode order

The duct eigenvalues K_{mn} are established by satisfying boundary conditions on the duct surface. The index m counts the number of lobes in the circumferential direction. The blade pressure harmonics k are given by $k = B \pm m$. The following table gives the ranges of k for propagating modes.

% Design RPM	M_X	M_T	BM_T/β	m_{max} for $BM_T \geq \beta K_{m0}$	Range of k
60	0.298	0.600	33.3	30	23 to 83
70	0.388	0.704	40.5	37	16 to 90
80	0.461	0.810	48.4	45	8 to 98
90	0.550	0.919	58.3	55	-2 to 108

For this table M_X (at the rotor face) was determined using the weight flow given in reference 9, standard day conditions, and isentropic flow relations. M_T came from the mechanical tip speed and the speed of sound at the rotor face set by M_X and isentropic flow.

APPENDIX C
WORKING FORMULAS FOR THEORETICAL SPECTRUM CALCULATIONS

This Appendix presents the formulas used for prediction of blade pressure, sound pressure, and sound power spectra in Section 6. These are essentially as described in reference 6 except for a variation on the blade pressure statistics to be described later.

Working Equations

The theoretical spectra, which correspond to measurements with a 500 filter analyzer much as a Spectral Dynamics model 301 B, C or D, consist of 500 filter levels in dB counted by the index m which runs from 1 to 500. For example,the blade pressure spectrum is calculated from

$$L_{xm} = 10 \log_{10}\left(\frac{2\pi^3 N \mu R_e \beta_x T}{R_T - R_H}\right)\left\{ \underbrace{Q_{xm} e^{-(2\pi x \sigma)^2}}_{\text{peaked component}} + S_{xm}\left[\underbrace{\sigma_a}_{\text{PAM}} + \underbrace{1-e^{-(2\pi x \sigma)^2}}_{\text{PPM}} \right] \right\} \tag{9}$$

where Q_{xm} and S_{xm} are statistical averages over all the eddies in the flow given symbolically by

$$Q_{xm} = \frac{1}{T^2 p_o^2} \iiint a^2 w^3 (2\pi\lambda)^2 \left| F(w\Omega x) \right|^2 L_m f(a,w,\lambda)\, da\, dw\, d\lambda \tag{10}$$

$$S_{xm} = \frac{1.58}{T^2 p_o^2} \iiint a^2 w^3 (2\pi\lambda) \left| F(w\Omega x) \right|^2 f(a,w,\lambda)\, da\, dw\, d\lambda \tag{11}$$

where F ( ) is the Fourier transform of the standard blade pressure pulse. These equations and equations 13 and 14 will be discussed later. The sound pressure spectrum is given by

$$L_{sm} = 10 \log_{10} \frac{\pi^3 N \mu^2 C_e^2 \beta_s T}{r^2} \sum_{n=-\infty}^{\infty} \nu_n \nu_{-n} Z_n \left\{ e^{-(By+n)^2 (2\pi\sigma)^2} Q_{smn} + \left[\sigma_a^2 + 1 - e^{-(By+n)^2 (2\pi\sigma)^2} \right] S_{smn} \right\} \tag{12}$$

where

$$Q_{smn} = \frac{1}{T^2 p_o^2} \iiint a^2 \; w^4 \; (2\pi B\lambda)^2 \left| F\left[w\Omega \; (By+n)\right]\right|^2 L_m \; f(a,w,\lambda) \; da \; dw \; d\lambda \qquad (13)$$

$$S_{smn} = \frac{1.58}{T^2 p_o^2} \iiint a^2 \; w^4 \; (2\pi B\lambda) \left| F\left[w\Omega \; (By+n)\right]\right|^2 f(a,w,\lambda) \; da \; dw \; d\lambda \qquad (14)$$

The sound power spectrum is given by

$$L_{wm} = 10 \log_{10}\left(\frac{\pi^3 N p_o^2 C_e^2 \mu^2}{W_o \rho c}\right)\left(\beta_s T\right)\sum_{n=-\infty}^{\infty} \nu_n \; \nu_{-n} \; \alpha_n \left\{ e^{-(By+n)^2 (2\pi\sigma)^2} \; Q_{smn} \right.$$

$$\left. + \left[\sigma_a^2 + 1 - e^{-(By+n)^2 (2\pi\sigma)^2}\right] S_{smn} \right\} . \qquad (15)$$

In equation 9,

R_e is the effective radius (taken here equal to 0.8)

R_T and R_H are the tip and hub radius of the rotor

β_x is the spacing between filters (full scale frequency /500)

T is the period of rotor rotation

x is the center frequency of the m^{th} filter divided by the rotor rotation frequency

σ and σ_a represent pulse position and pulse amplitude modulation as described in reference 6.

μ is the ratio of radial to circumferential length scales entering the rotor. (μ was set to 1 for the present study).

To use equation 9, the blade pressure spectrum shape is matched to the test spectrum as nearly as possible using the parameters σ and σ_a and the statistical parameters in Q_{xm} and S_{xm}. Then normally the spectrum level is adjusted using the parameter N, which represents the number of eddies entering the rotor per revolution. However, as described in the text, an absolute level calibration was not possible and N was not determined.

In equation 12 for the sound pressure spectrum,

β_s is the filter spacing for the sound spectra.

r is the microphone distance

y is the center frequency of the m^{th} filter

$$Z_n = \frac{1}{4}\left(yB \sin\beta \cos\theta + \frac{n\cos\beta}{M}\right)^2 J_n^{\,2}\,(yBM \sin\theta)$$

B is the number of blades (53)

β and M are the blade stagger angle and rotational Mach number at the effective radius

θ is the microphone angle

For reasons given in the text, the effective chord C_e was not found. The product $\nu_n \nu_{-n}$ comes from the assumption of a triangular chordwise loading peaked at the leading edge:

$$\nu_o^{\,2} = 1$$

$$\nu_n\ \nu_{-n} = 4\left(\frac{R_e}{nC_B}\right)^4 \left[2+\left(\frac{nC_B}{R_e}\right)^2 - 2\cos\left(\frac{nC_B}{R_e}\right) - \frac{2nC_B}{R_e}\sin\left(\frac{nC_B}{R_e}\right)\right] \quad , n \neq 0. \tag{16}$$

In the sound power spectrum

$W_o = 10^{-13}$ Watt

$p_o = 2 \times 10^{-5}$ Pascal

$$\alpha_n = 2\pi \int_0^{\pi} Z_n \sin\theta \, d\theta$$

ρ and c are the ambient density and sound speed

The statistics required for the calculation of Q_{xm}, S_{xm}, Q_{smn}, and S_{smn} were slightly changed from those in reference 6 for a better match with the QF-1B data. In particular, the joint probability density function for pulse amplitude a, width w, and length λ were modified from the form.

$$f(a, w, \lambda) = f_{a/w, \lambda}(a/w, \lambda) f_{w/\lambda}(w, \lambda) f_{\lambda}(\lambda) \tag{17}$$

given by equation (67) of reference 6 to

$$f(a, w, \lambda) = \sum_{i=1}^{I} k_i f_{ia/w}(a/w) f_{iw}(w) f_{i\lambda}(\lambda) \tag{18}$$

which permits independent families of eddies (counted by the index i) to coexist in the flow. The density function for the amplitude, given the width, is Gaussian:

$$f_{ia/w}(a/w) = \frac{e^{-a^2/2A_i^2}}{A_i\sqrt{2\pi}} \tag{19}$$

where A_i is the RMS amplitude. The density functions for width and length are exponential:

$$f_{iw}(w) = \frac{e^{-w/W_i}}{W_i} \tag{20}$$

$$f_{i\lambda}(\lambda) = \frac{e^{-\lambda/L_i}}{L_i} \tag{21}$$

where W_i and L_i are the mean pulse width and eddy length.

The amplitude and width statistics are coupled through

$$A_i^2 = K_i \left(\frac{w}{W_i}\right)^{E_i} \tag{22}$$

which means that, on the average, pulse heights are proportional to pulse widths to the E_i power.

When these formulas are substituted into the probability integrals given by equations (54) and (56) of reference 6, the integrations over a and w were performed analytically, leaving the following integrals to be done numerically.

$$Q_{xm} = \pi^2 \sum_{i=1}^{I} \frac{C_i L_i^2 \Gamma (E_i + 4)}{W_i^{E_i + 1} (4\pi x + 1/W_i)^{E_i + 4}} \int_0^{\infty} Z_i^2 L_m (L_i) e^{-Z_i} dZ_i \tag{23}$$

$$S_{xm} = \frac{1.58\pi}{2} \sum_{i=1}^{I} \frac{C_i L_i \Gamma (E_i + 4)}{W_i^{E_i + 1} (4\pi x + 1/W_i)^{E_i + 4}} \tag{24}$$

$$Q_{smn} = \pi^2 B^2 \sum_{i=1}^{I} \frac{C_i L_i^2 \Gamma (E_i + 5)}{W_i^{E_i + 1} (4\pi \left| By + n \right| + 1/W_i)^{E_i + 5}} \int_0^{\infty} Z_i^2 L_m (L_i) e^{-Z_i} dZ_i \tag{25}$$

$$S_{smn} = \frac{1.58\pi B}{2} \sum_{i=1}^{I} \frac{C_i L_i \Gamma (E_i + 5)}{W_i^{E_i + 1} (4\pi \left| By + n \right| + 1/W_i)^{E_i + 5}} \tag{26}$$

where $Z_i = \lambda / L_i$. L_m is the integral of the theoretical PSD peak over the actual filter passband characteristics (ref. 6).

Statistical Parameters

These formulas, with I = 2, were used for the predictions presented in Section 6. Values of the statistical parameters are given in the following for the four RPM's tested.

STATISTICAL PARAMETERS USED IN FIT OF BLADE PRESSURE SPECTRA

TEST COND	C_2	W_1	W_2	E_1	E_2	L_1	L_2	σ_a	σ
403 - 80% RPM	0.01	0.005	0.005	-1.9	0.1	0.01	0.5	0.2	0.0021
401 - 60% RPM	3.2×10^{-7}	0.001	0.001	-1.9	7.1	0.1	1.0	0.10	0.0015
401 - 70% RPM	3.2×10^{-7}	0.001	0.001	-1.9	7.1	0.2	2.0	0.05	0.0017
401 - 80% RPM	3.2×10^{-7}	0.001	0.001	-1.7	7.3	0.1	2.0	0.10	0.0013
401 - 90% RPM	3.2×10^{-7}	0.001	0.001	-1.9	7.1	0.03	0.3	0.10	0.0012

These values apply for all test conditions:

$\mu = 1.0$

$R_e/R_T = 0.8$

$C_1 = 1.0$

Note: k_i and K_i appear only as the product $k_iK_i = C_i$ for i = 1 and 2

Interpretation

In the previous work with Q-Fan data, a good match of theoretical blade pressure spectra to test spectra was achieved using the single family probability density function (PDF) given by equation 17. However, for the QF-1B data no such PDF could be found which produced a good match at both high and low frequency. Therefore, the PDF was generalized to equation 18 with I = 2 so that one set of eddies (i = 1) could be used to match spectra at high frequencies and another set (i = 2) for low frequencies. As suggested by the values of L_1 and L_2 in the table above, the high frequency contributors tend to have a shorter axial scale than the low frequency contributors. As can be inferred from equations 23-26, the parameters E_1 and E_2 determine the general slope of the

spectrum which tends to be relatively flat at high frequencies and steep at low frequencies. Beyond these comments, it does not appear possible to interpret the statistical parameters in physical terms. Also, since different forms for the PDF were used for the QF-1B and the Q-Fan, the inflow to these two fans cannot be compared through the above blade pressure statistics.

REFERENCES

1. Povinelli, F. P.; and Dittmar, J. H.: Installation Caused Flow Distortion and Its Effect on Noise from a Fan Designed for Turbofan Engines. NASA TM X-68105, 1972.

2. Hanson, Donald B.: Spectrum of Rotor Noise Caused by Atmospheric Turbulence. J. Acoust. Soc. Am., vol. 56, no. 1, July 1974.

3. Hanson, Donald B.: Measurements of Static Inlet Turbulence. Preprint no. 75-467, Am. Inst. Aeron. and Astronaut., March 1975.

4. Hanson, Donald B.: A Study of Subsonic Fan Noise Sources. Preprint no. 75-468, Am. Inst. Aeron. and Astronaut., March 1975.

5. Bliss, D. B.; Chanderamani, K. L.; and Piersol, A. G.: Data Analysis and Noise Prediction for the QF-1B Experimental Fan Stage. NASA CR-135066, 1976.

6. Hanson, D. B.: Study of Noise Sources in a Subsonic Fan Using Measured Blade Pressures and Acoustic Theory. NASA CR-2574, 1975.

7. Hanson, Donald B.: Unified Analysis of Fan Stator Noise. J. Acoust. Soc. Am., vol. 54, no. 6, Dec. 1973.

8. Tyler, J. M.; and Sofrin, T. G.: Axial Flow Compressor Noise Studies. Trans. S.A.E., 1961, pp 309-332.

9. Leonard, B. R.; Schmiedlin, R. F.; Stakolich, E. G.; and Neumann, H. E.: Acoustic and Aerodynamic Performance of a 6-Foot-Diameter Fan for Turbofan Engines. NASA TN D-5877, 1970.

10. Gelder, T. F.; Lewis, G. W.: Aerodynamic Performance of 0.5 Meter Diameter, 337-Meter-per-Second Tip Speed, 1.5-Pressure-Ratio, Single Stage Fan Designed for Low Noise Aircraft Engines. NASA TN D-7836, 1974.

11. Hanson, D. B.: Application of Rotor Mounted Pressure Transducers to Analysis of Inlet Turbulence. Preprint no. 177-9, AGARD Conference on Unsteady Phenomena in Turbomachinery, 1975.

12. Kerrebrock, J. L.: Small Disturbances in Turbomachine Annuli with Swirl. Mass. Inst. of Tech. Gas Turbine Laboratory Report no. 125, 1975.

13. Thompkins, W. T.; and Kerrebrock, J. L.: Exit Flow from a Transonic Compressor Rotor. Preprint no. 177-6, AGARD Conference on Unsteady Phenomena in Turbomachinery, 1975.

14. Gelder, T. F.; and Soltis, R. F.: Inlet Noise of 0.5 Meter Diameter NASA QF-1 Fan as Measured in an Unmodified Compressor Aerodynamic Test Facility and in an Anechoic Chamber. NASA TN D-8121, 1975.

15. Goldstein, M. E.: Aeroacoustics. McGraw-Hill, Inc., 1976.

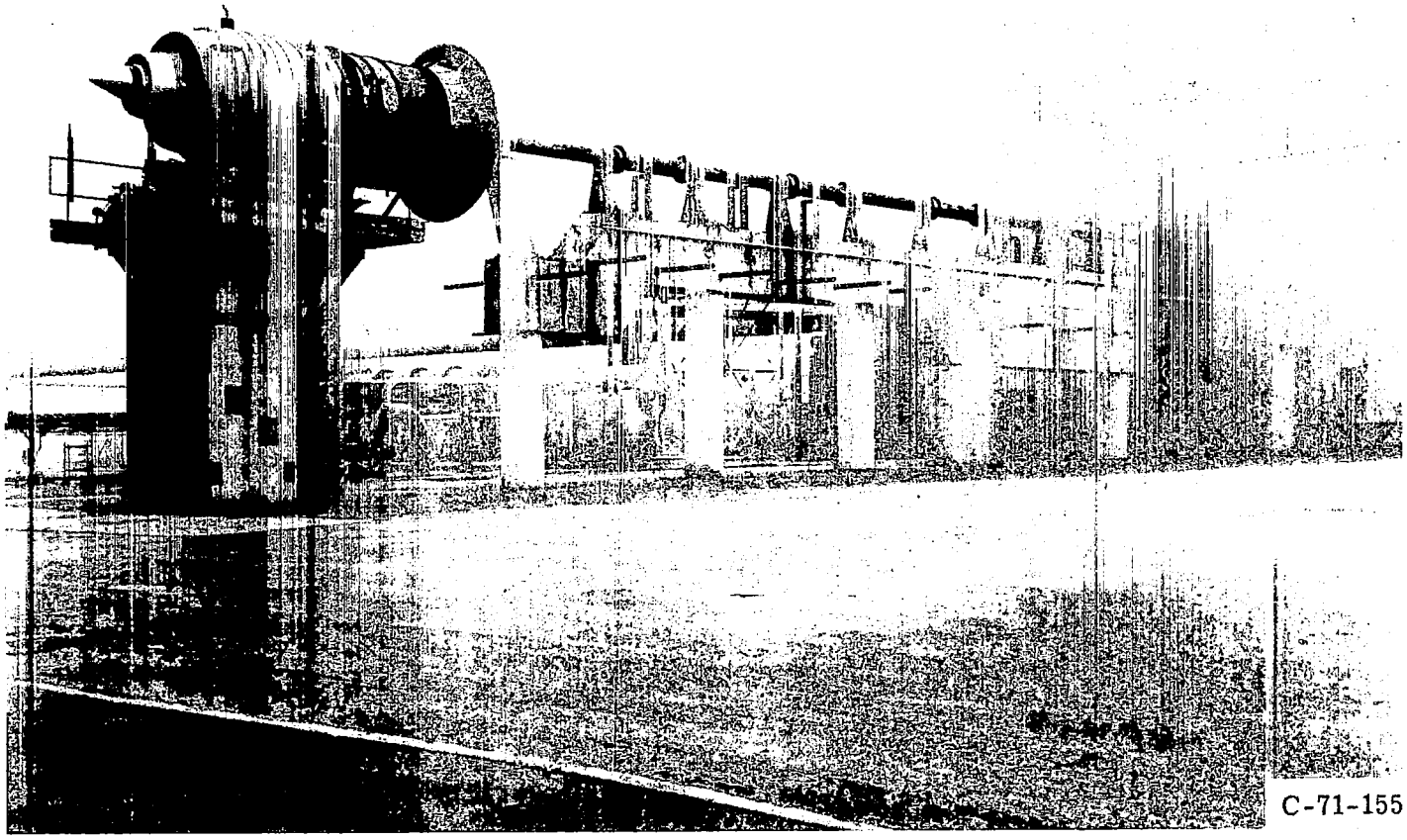

Figure 1. Rear quarter view of test fan in front drive configuration

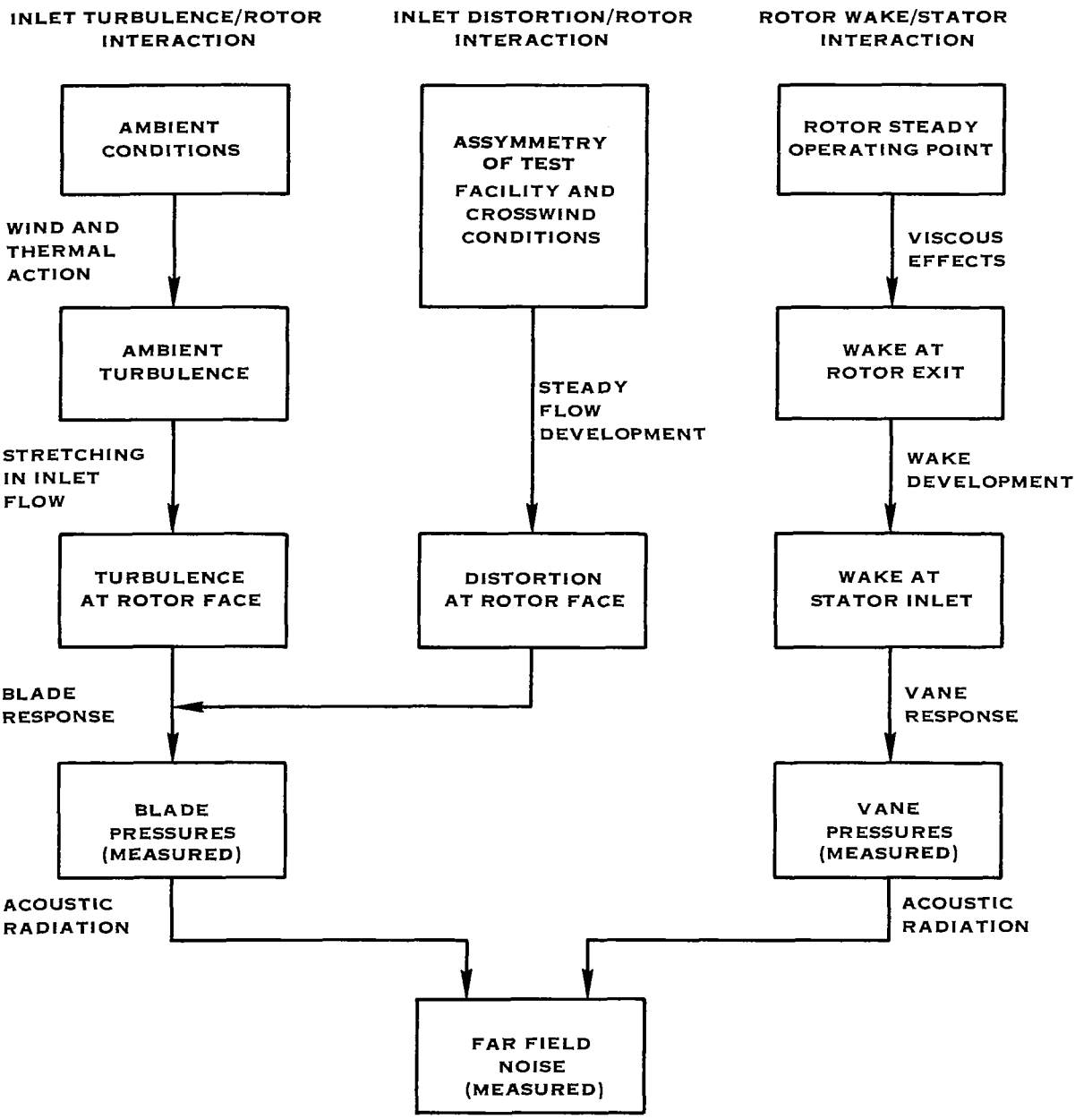

Figure 2. Fan noise generation processes

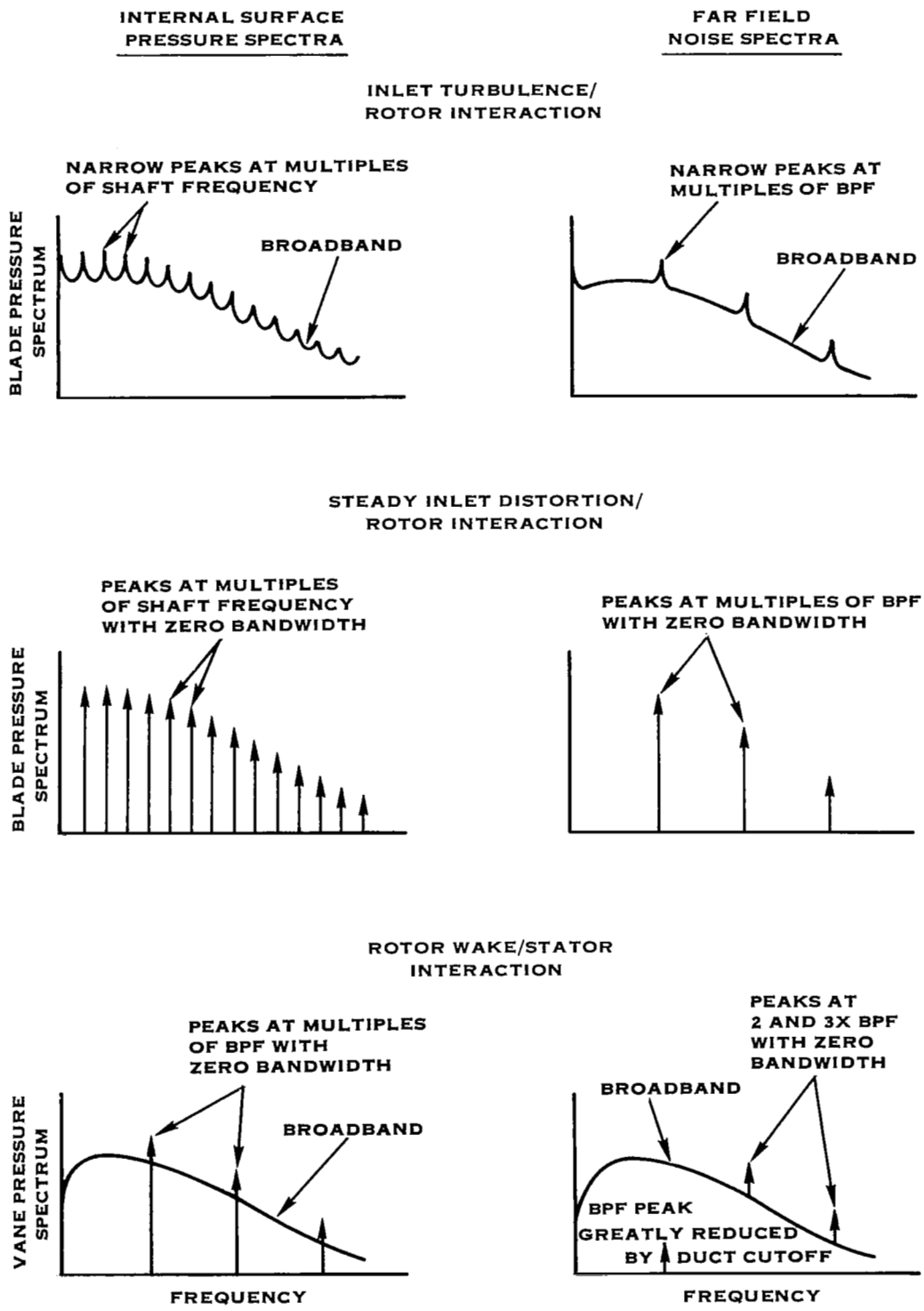

Figure 3. Comparison of blade and vane surface pressure spectra with corresponding noise spectra for 3 noise mechanisms

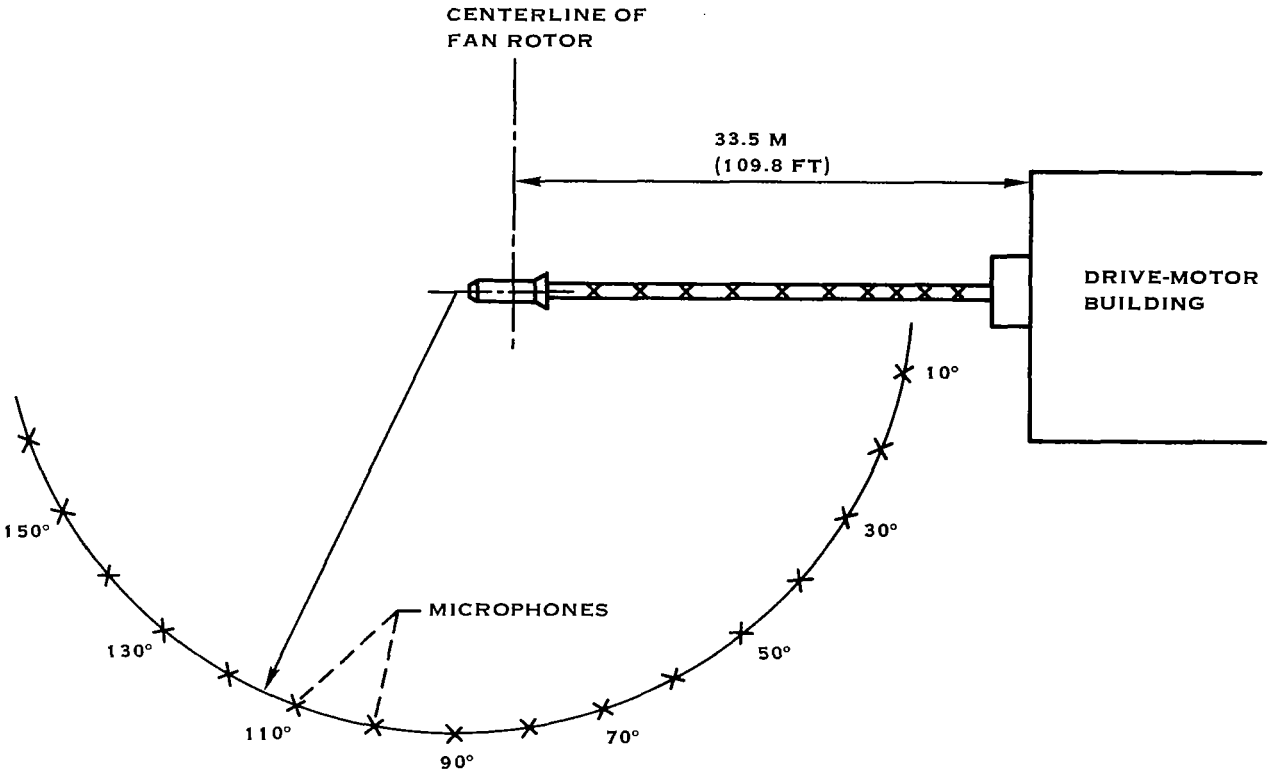

Figure 4. Plan view of full scale quiet fan test facility at NASA-Lewis

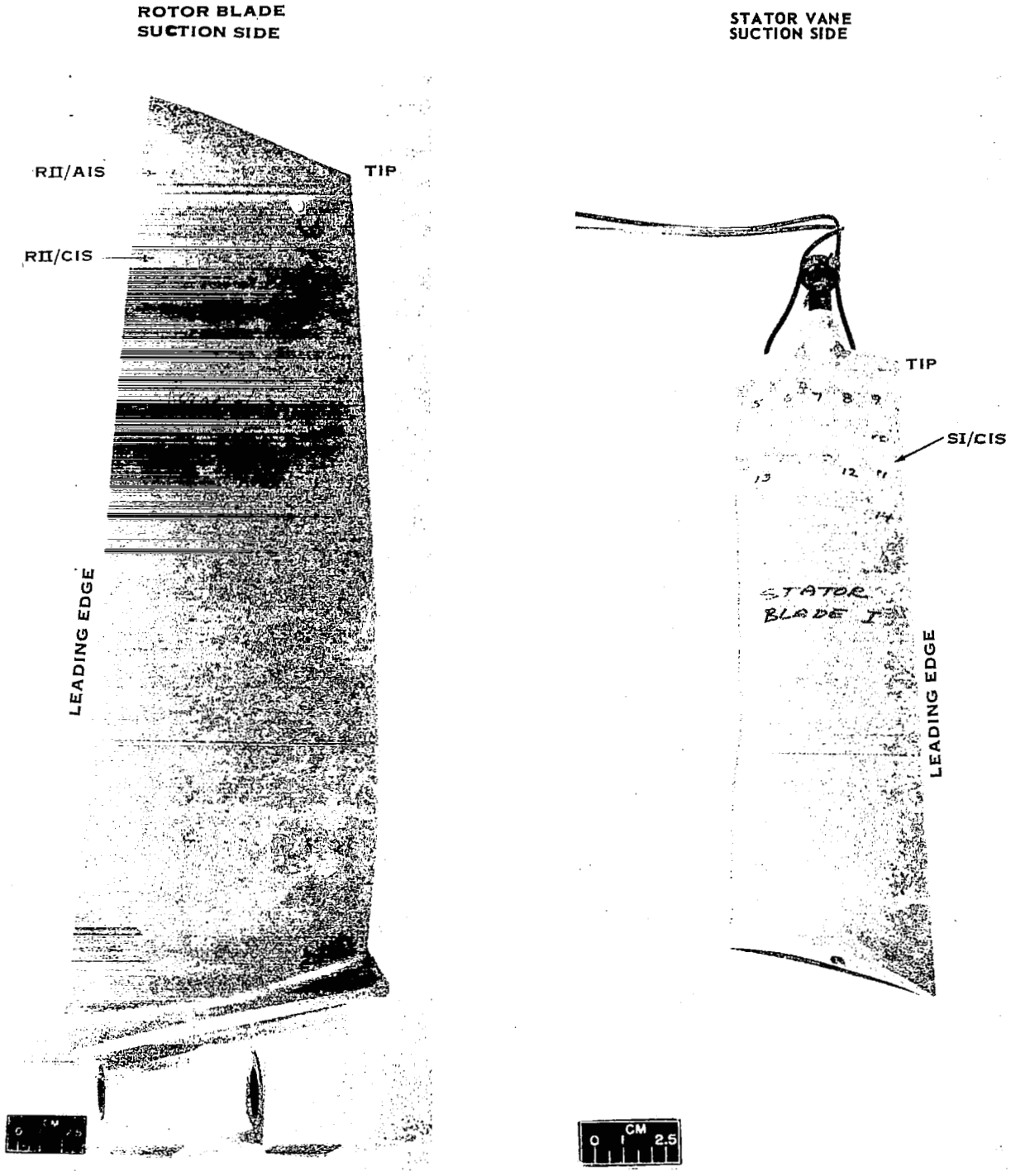

Figure 5. Instrumented rotor blade and stator vane showing transducers used for this report (From NASA-Lewis photographs C-74-1304 and C-74-1307)

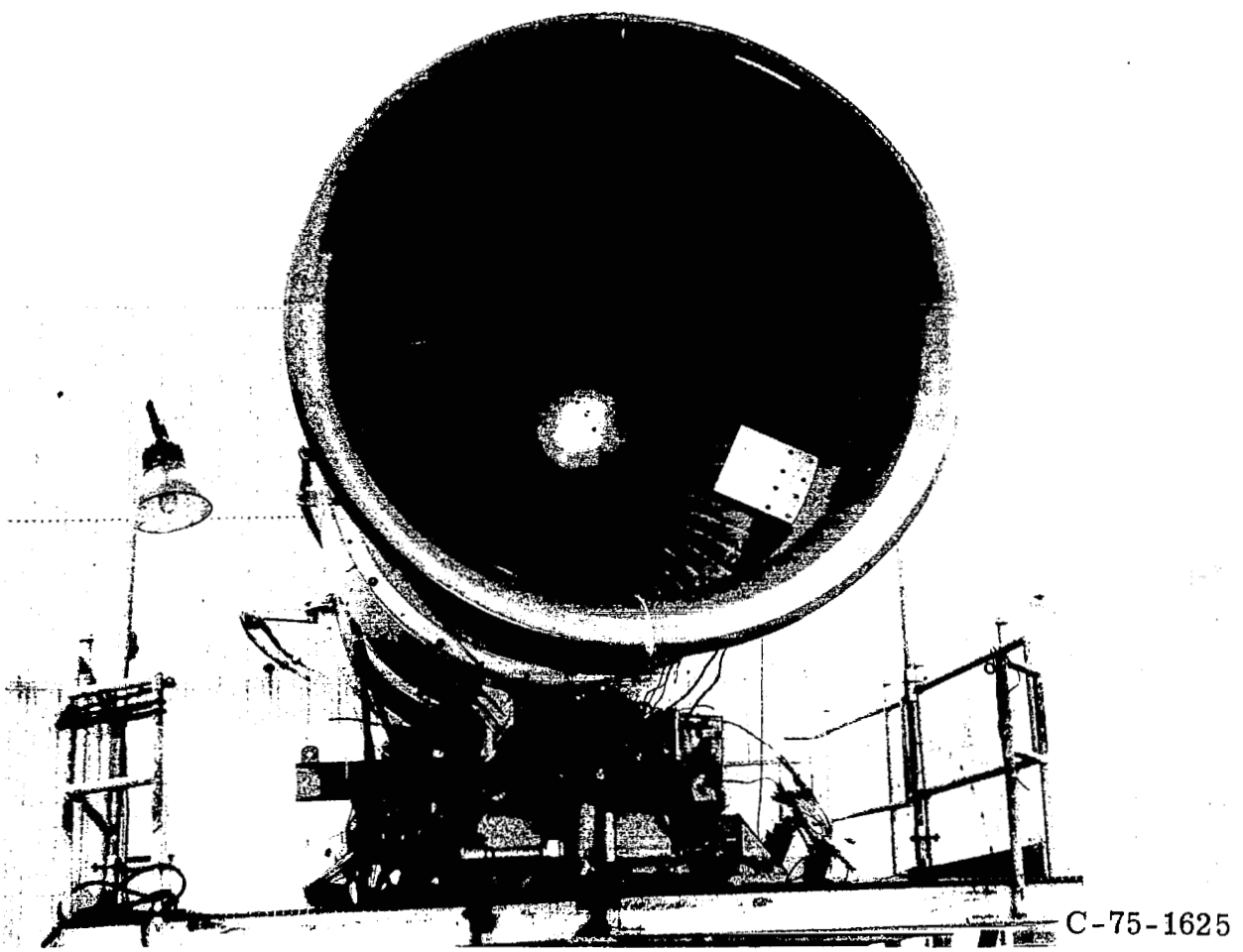

Figure 6. Blockage plate installed in inlet of test fan. This photograph shows the fan in the rear drive configuration whereas the data analyzed in this report is from the front drive configuration.

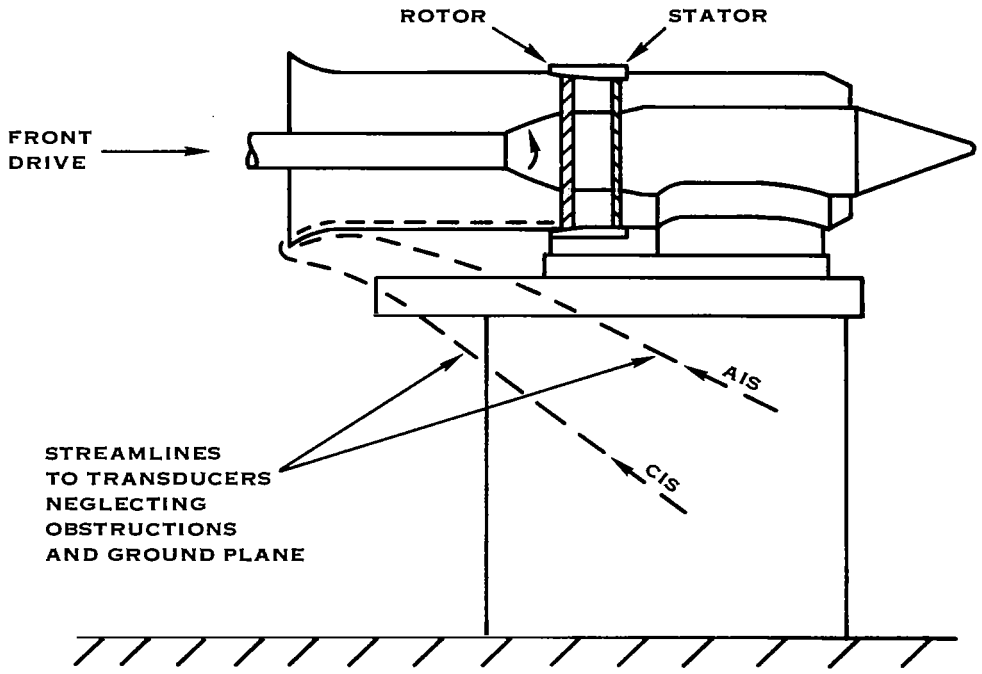

Figure 7. Side view of QF-1B showing possible streamlines to transducers at two rotor radii

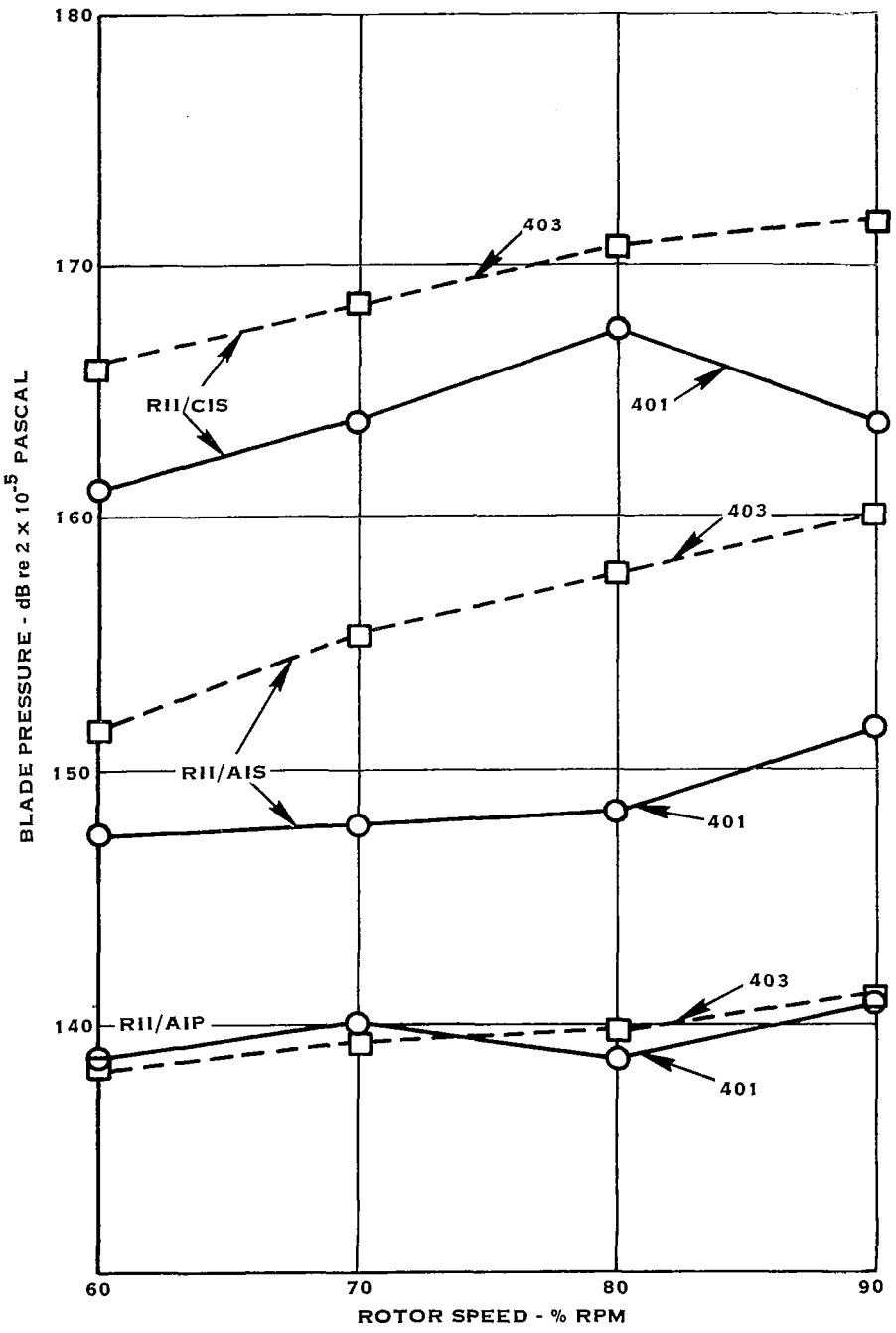

Figure 8. Overall blade pressure versus RPM with clean inlet (Configuration 401) and with inlet partially blocked by a plate (Configuration 403).

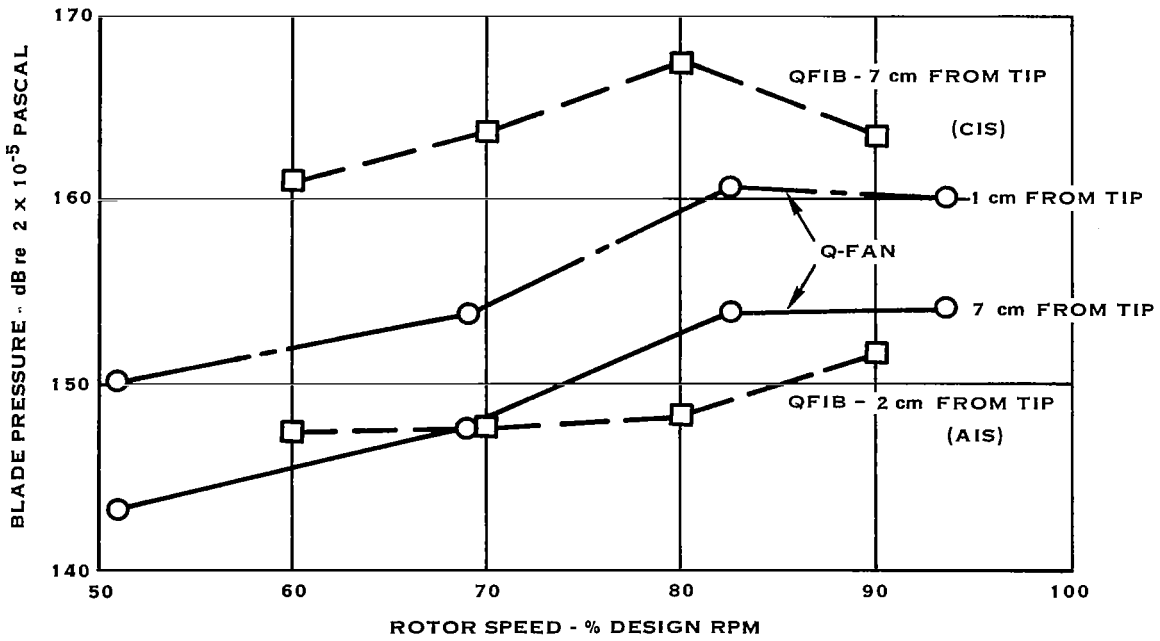

Figure 9. Overall (mean square) blade pressure versus RPM compared for Hamilton Standard Q-Fan and NASA-Lewis QF-1B

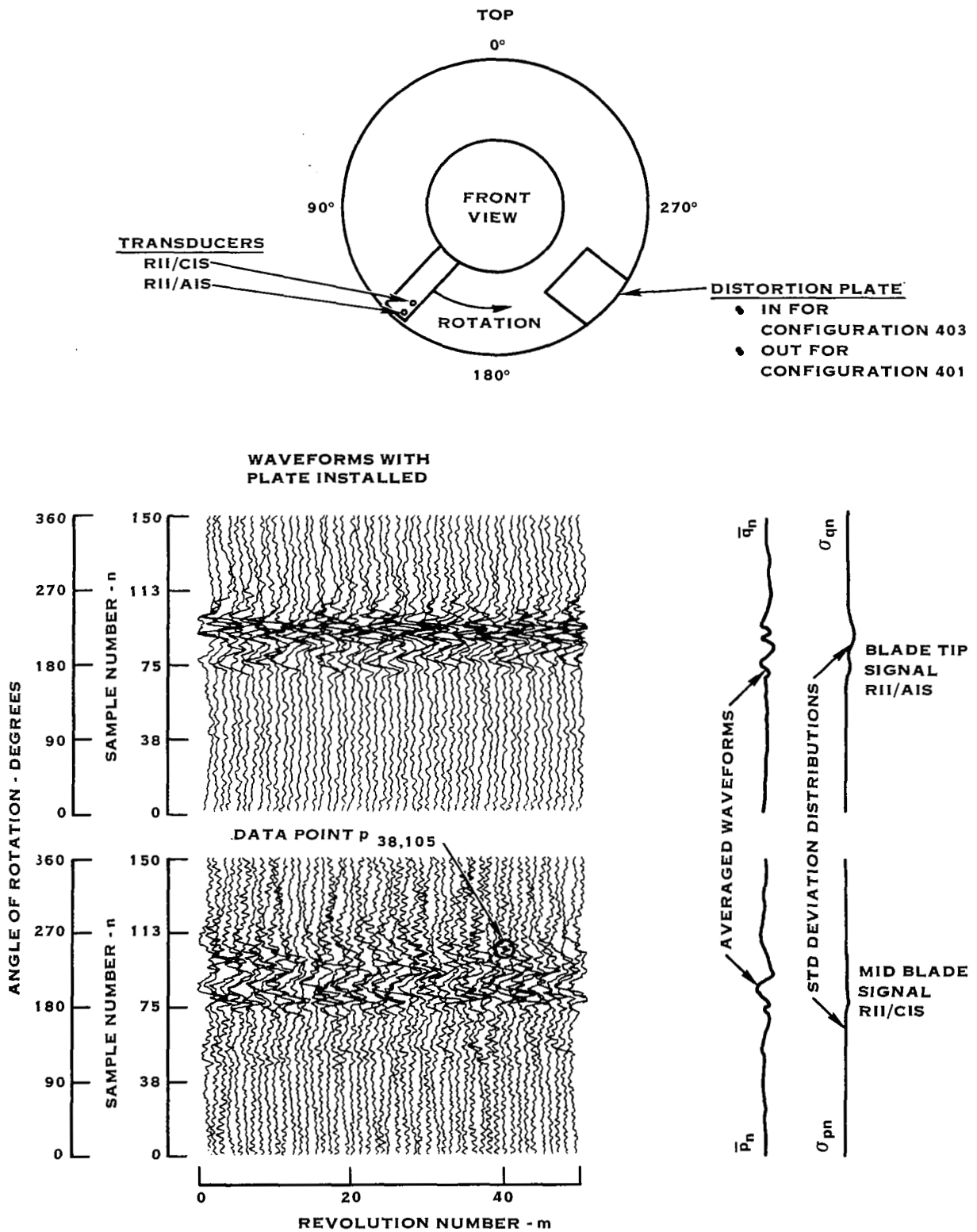

Figure 10. Explanation of blade pressure waveform plots indicating transducer numbers and configuration numbers

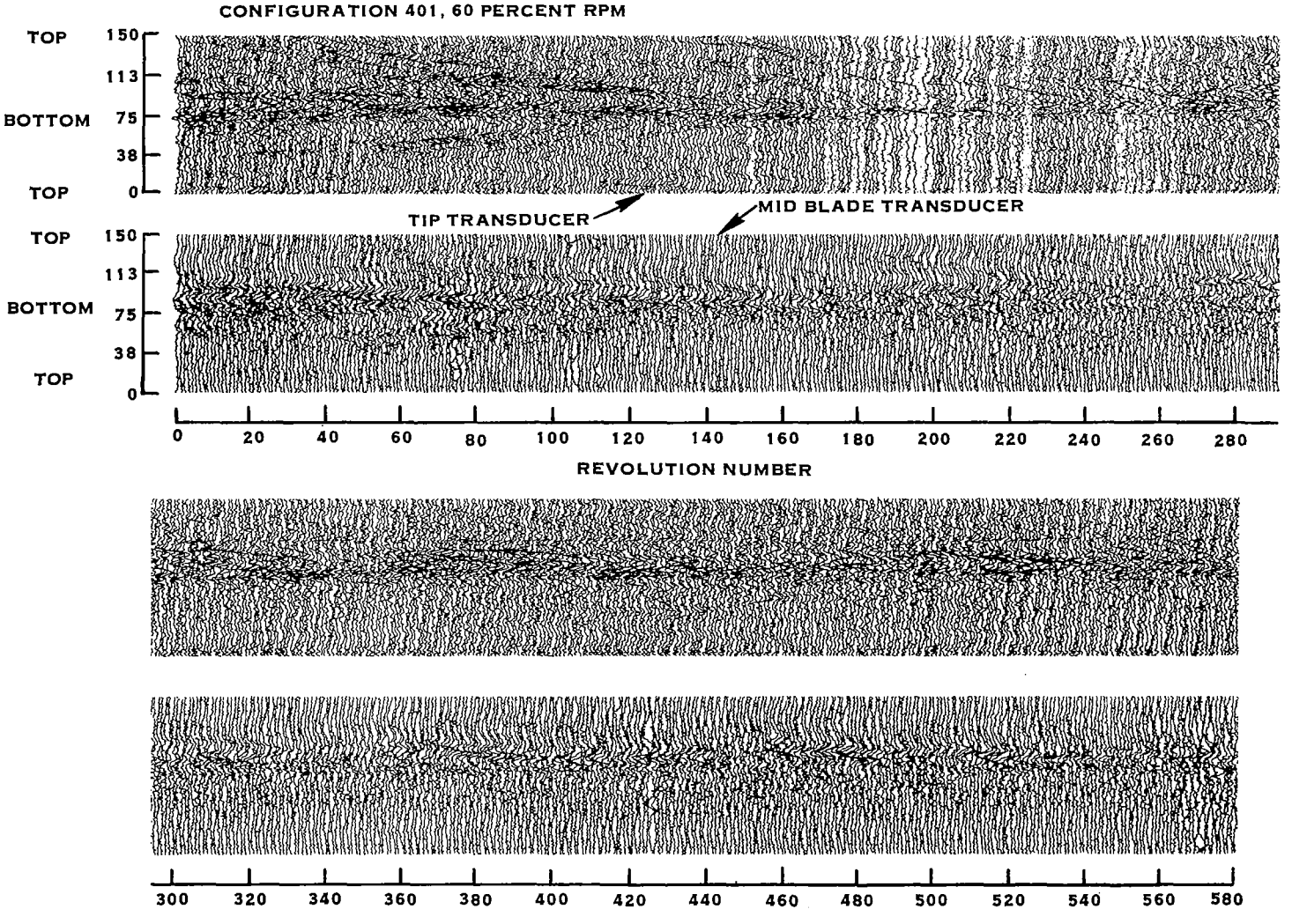

Figure 11. Inlet distortion space-time history - 60% RPM, clean inlet

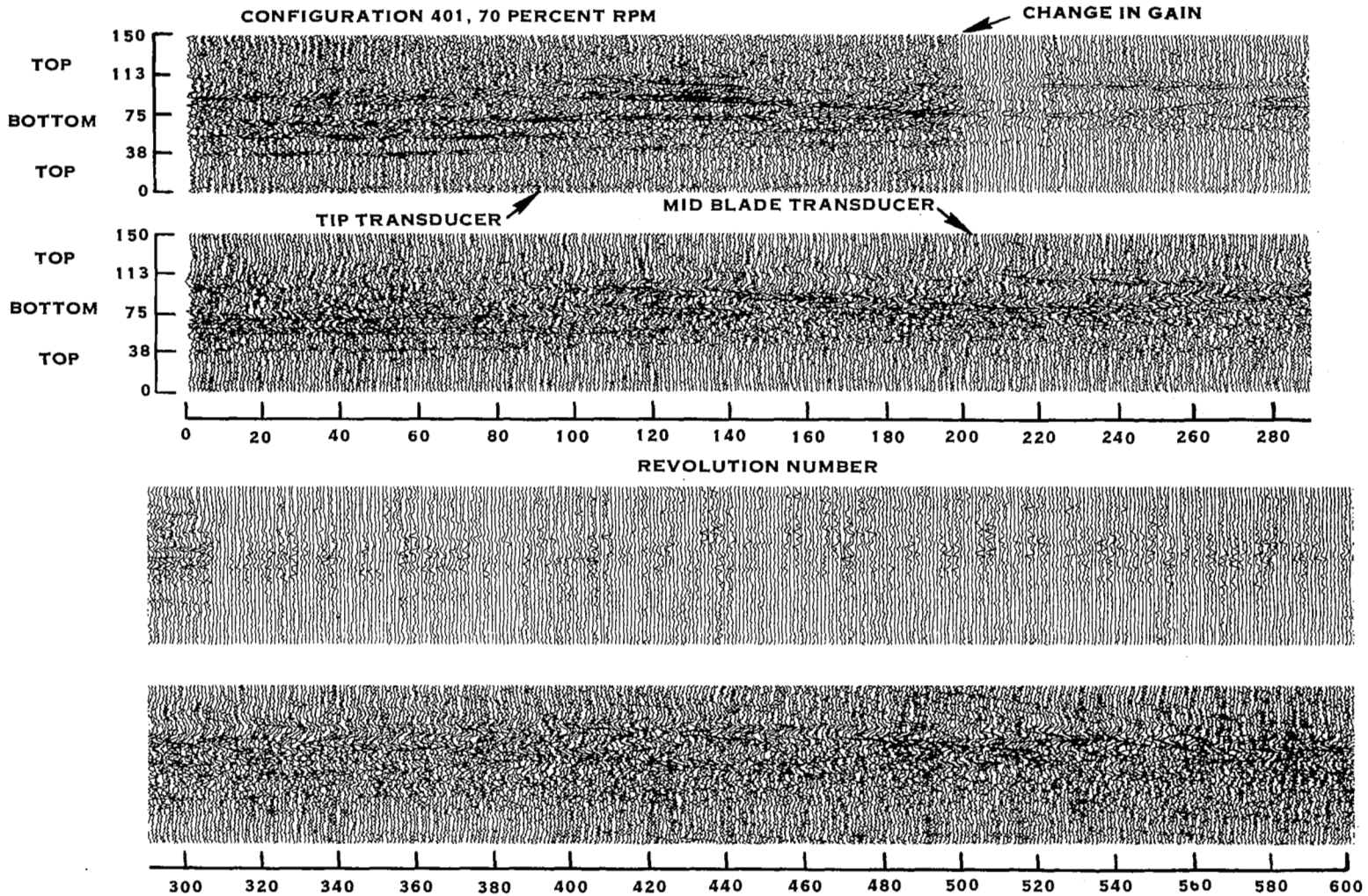

Figure 12. Inlet distortion space-time history - 70% RPM, clean inlet

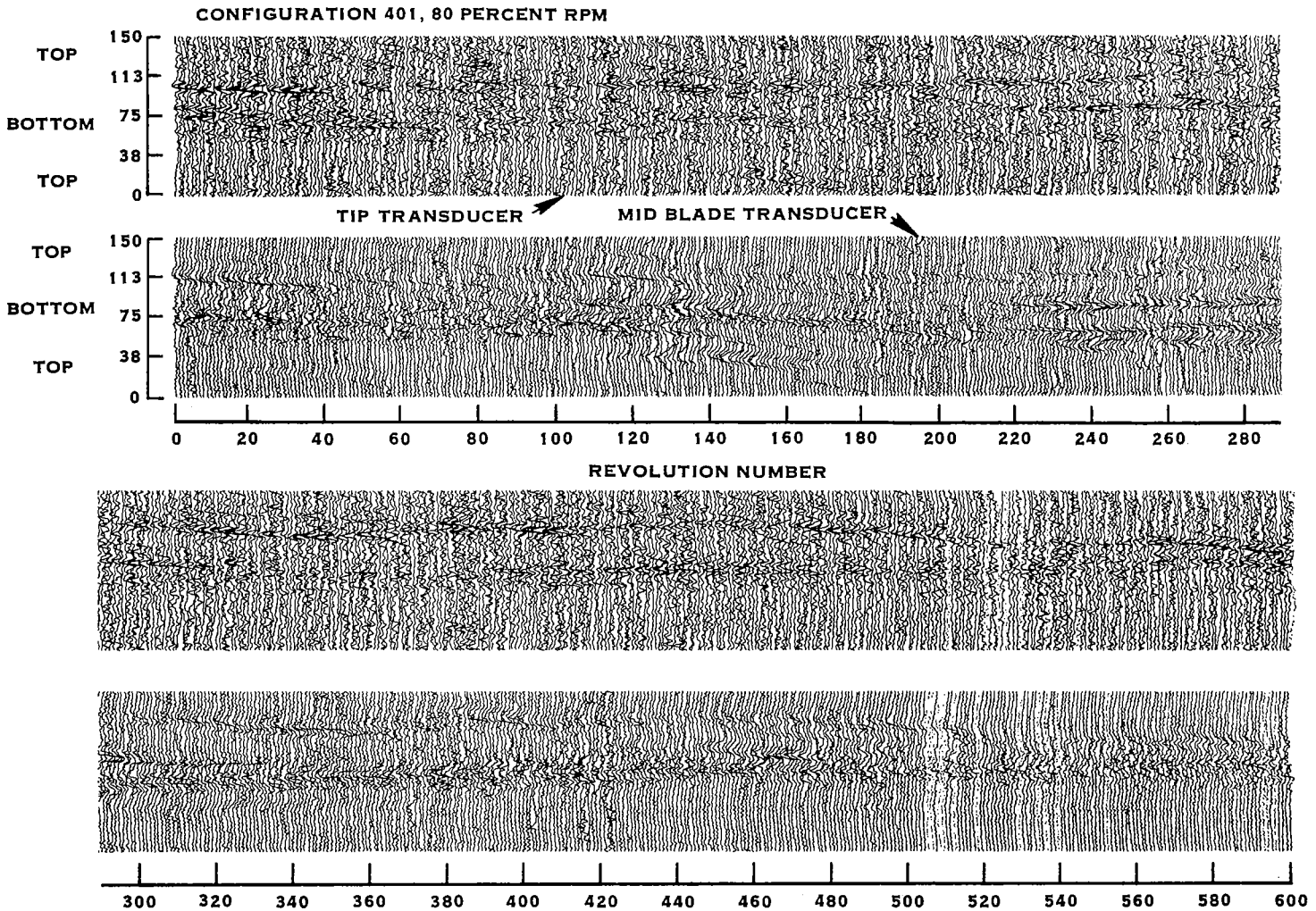

Figure 13. Inlet distortion space-time history - 80% RPM, clean inlet

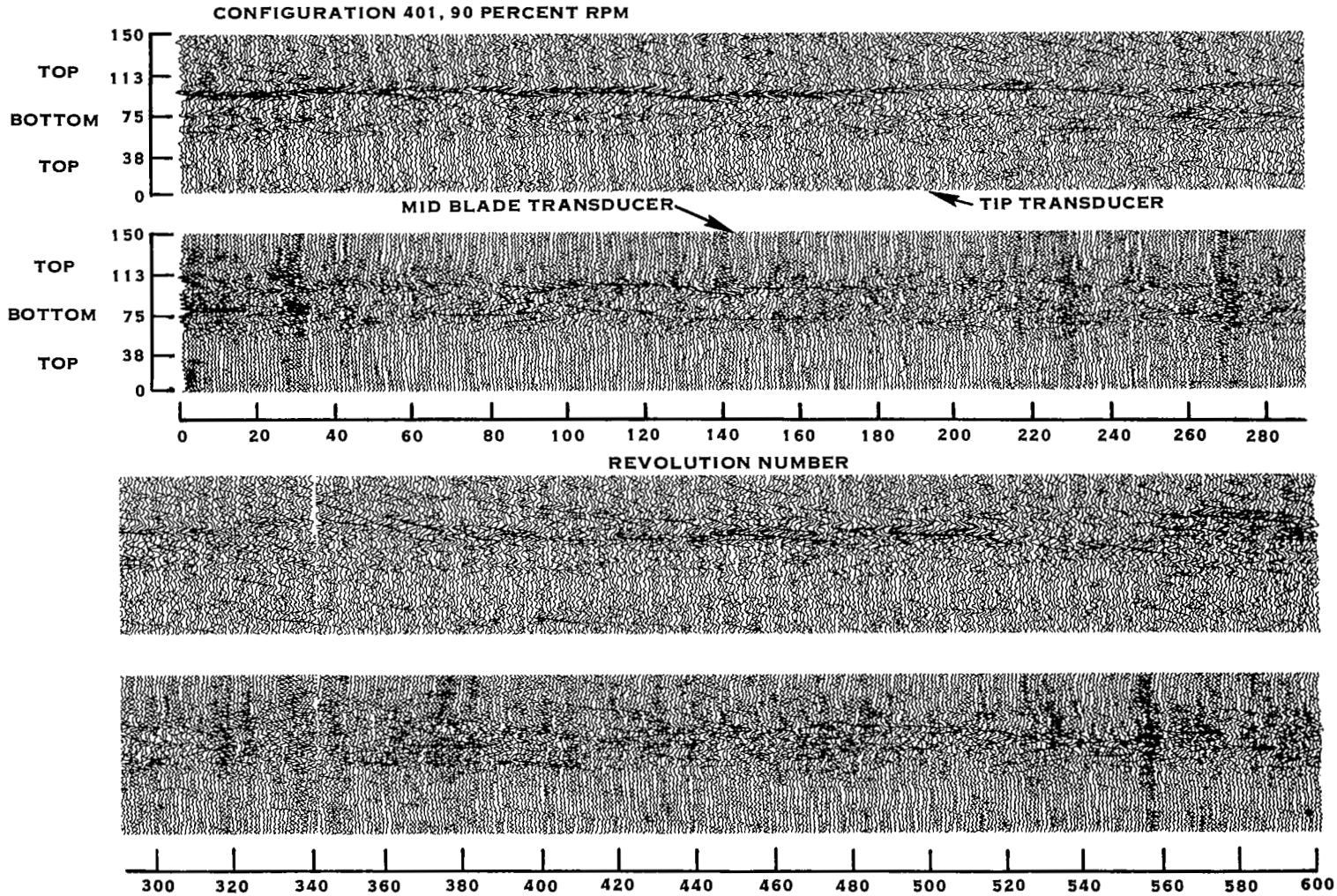

Figure 14. Inlet distortion space-time history - 90% RPM, clean inlet

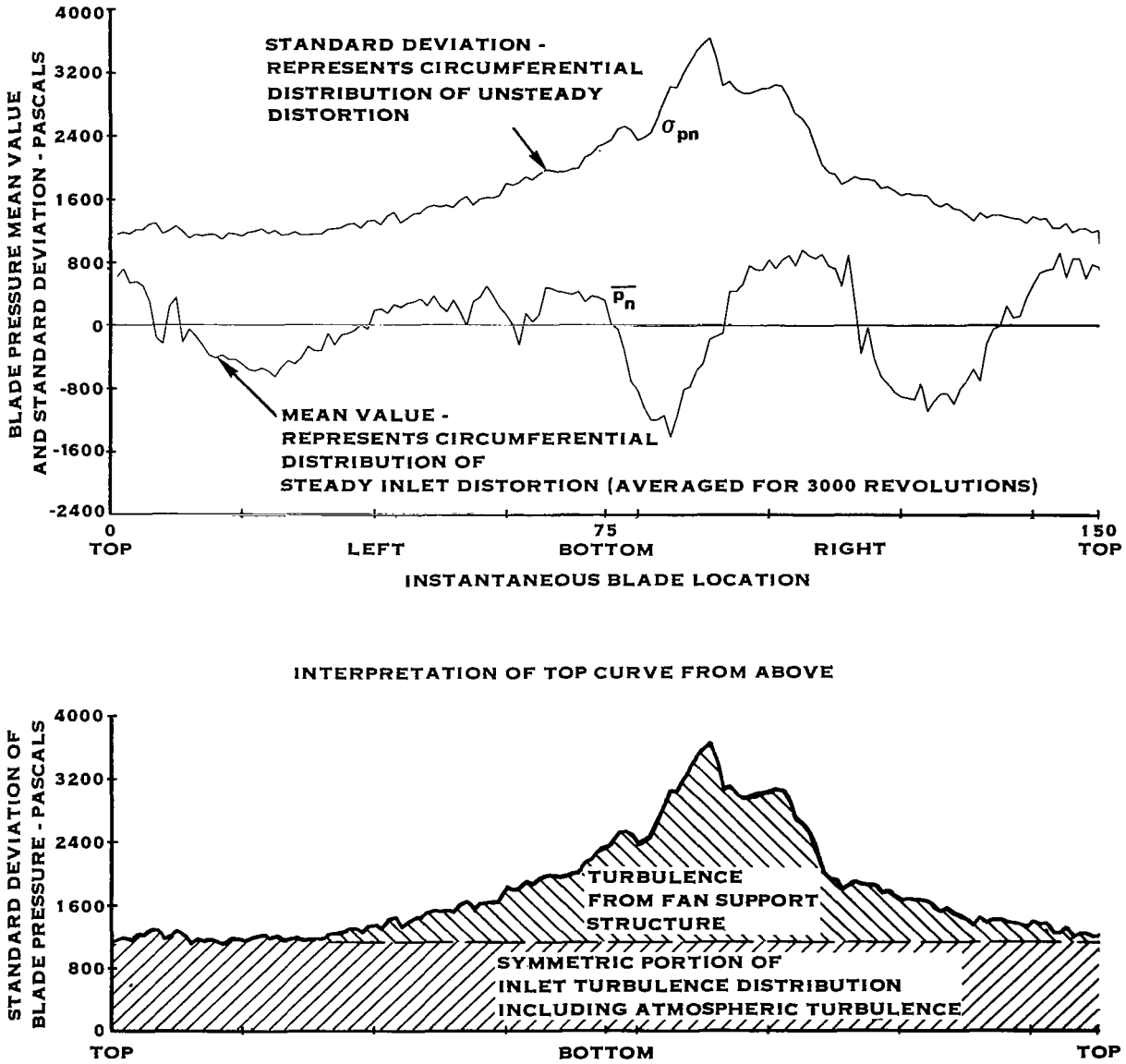

Figure 15. (Top) Explanation of digital plots of blade pressure mean value and standard deviation, 60% RPM. (Bottom) Interpretation of standard deviation distribution plot. (Note: 6895 Pascals = 1 pound/square inch)

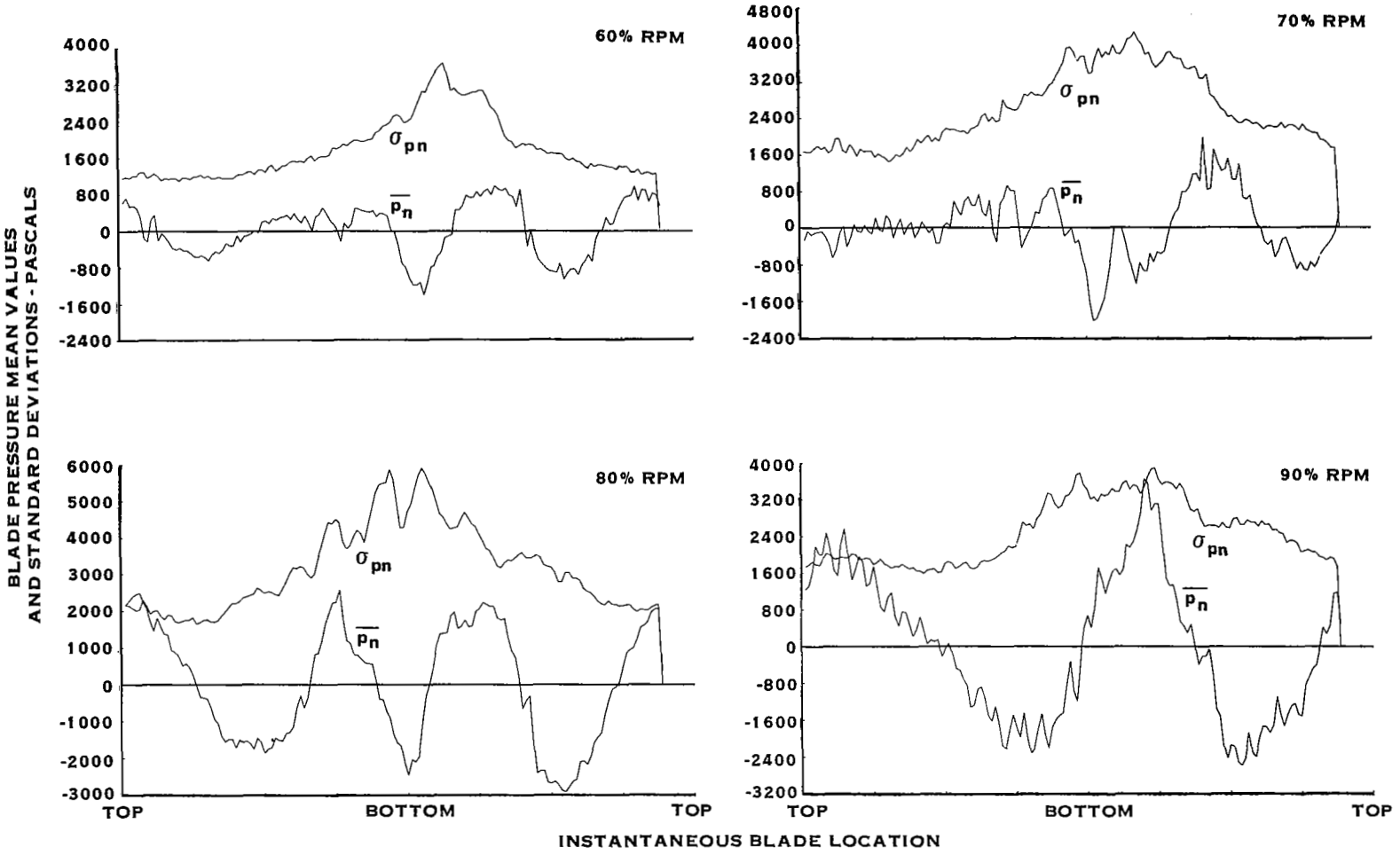

Figure 16. Distributions of mean and standard deviation of blade pressure around fan circumference. Configuration 401 (clean inlet). Mid blade transducer - RII/C1S

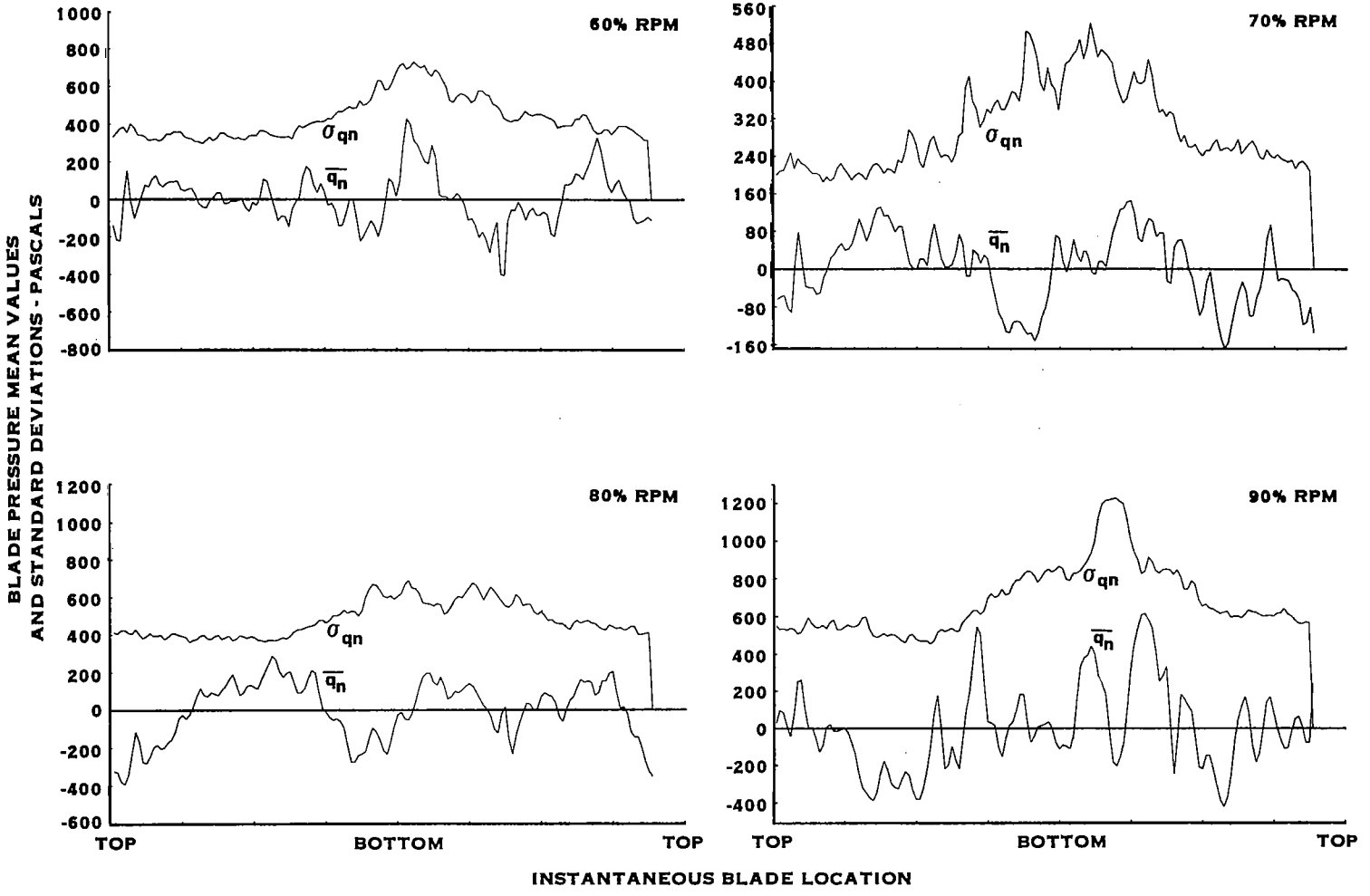

Figure 17. Distributions of mean and standard deviation of blade pressure around fan circumference. Configuration 401 (clean inlet). Tip transducer - RII/A1S.

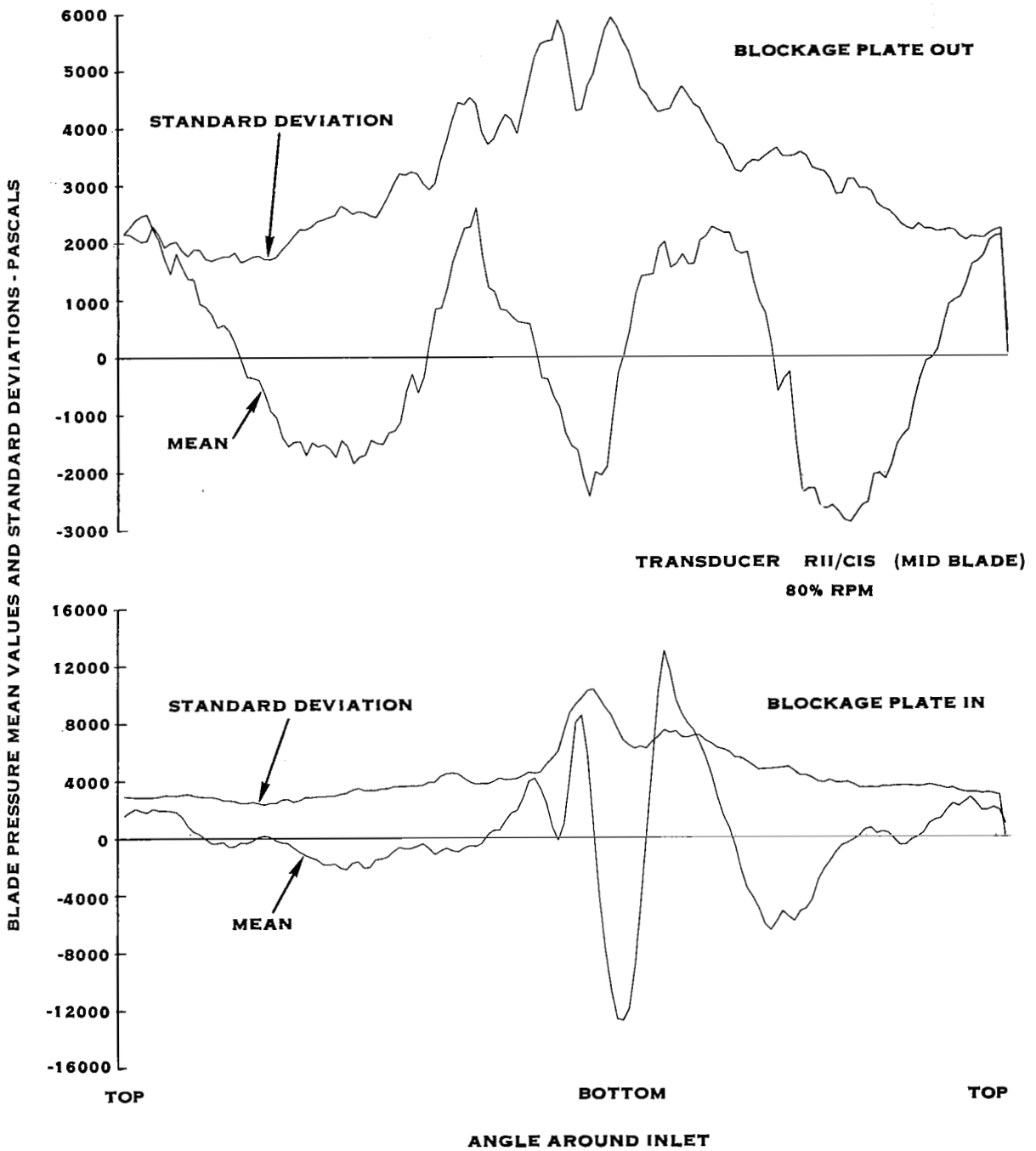

Figure 18. Effect of blockage plate on distributions of blade pressure mean value and standard deviation

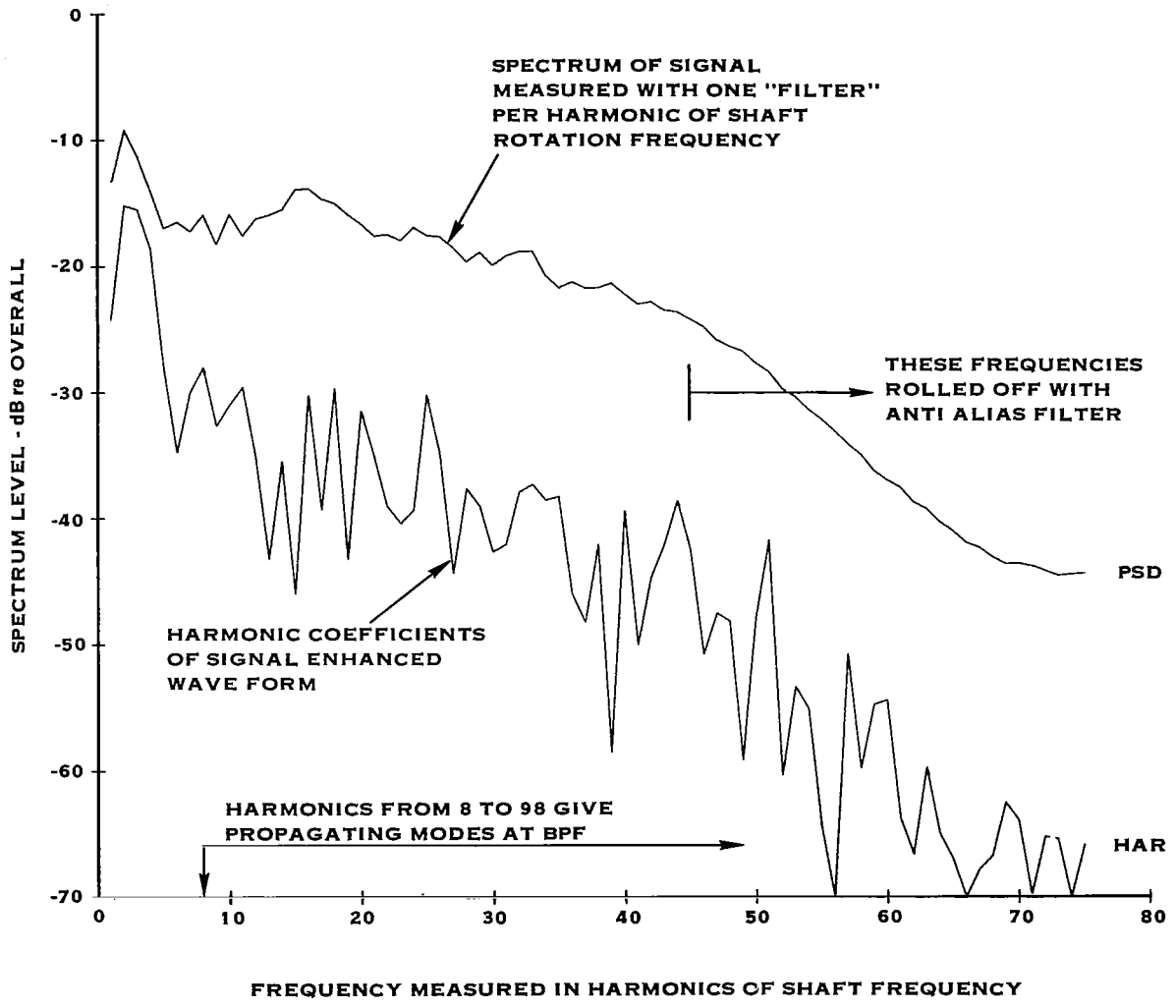

Figure 19. Explanation of digital spectrum plots used in this report. Upper curve gives frequency distribution of overall signal. Lower curve gives frequency distribution of harmonic portion of signal. Difference in the two curves represents the random portion of the signal. These spectra and all succeeding digital spectra were averaged for 1000 revolutions.

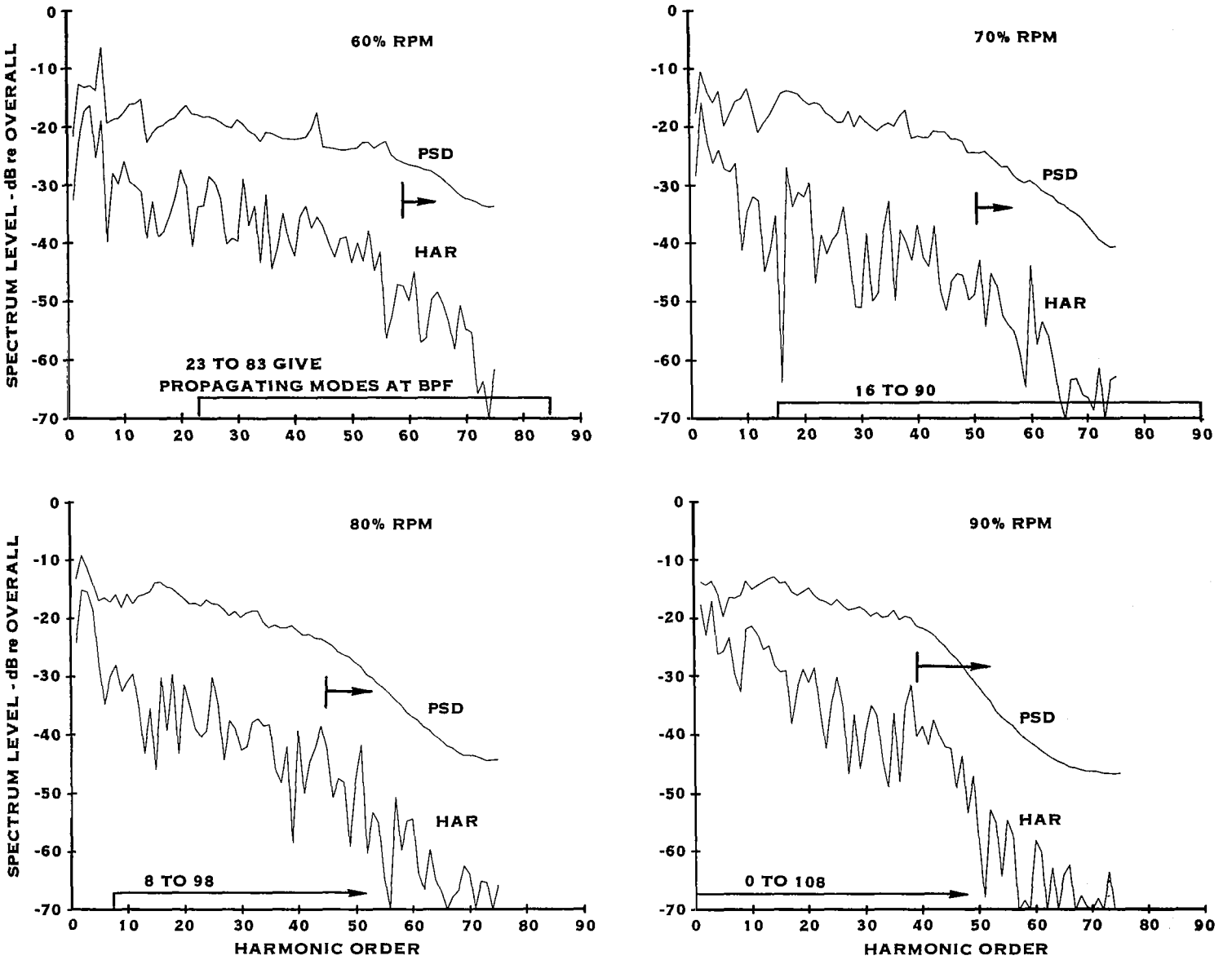

Figure 20. Digital spectrum plots for rotor pressure transducer RII/A1S (near tip) configuration 401 (clean inlet)

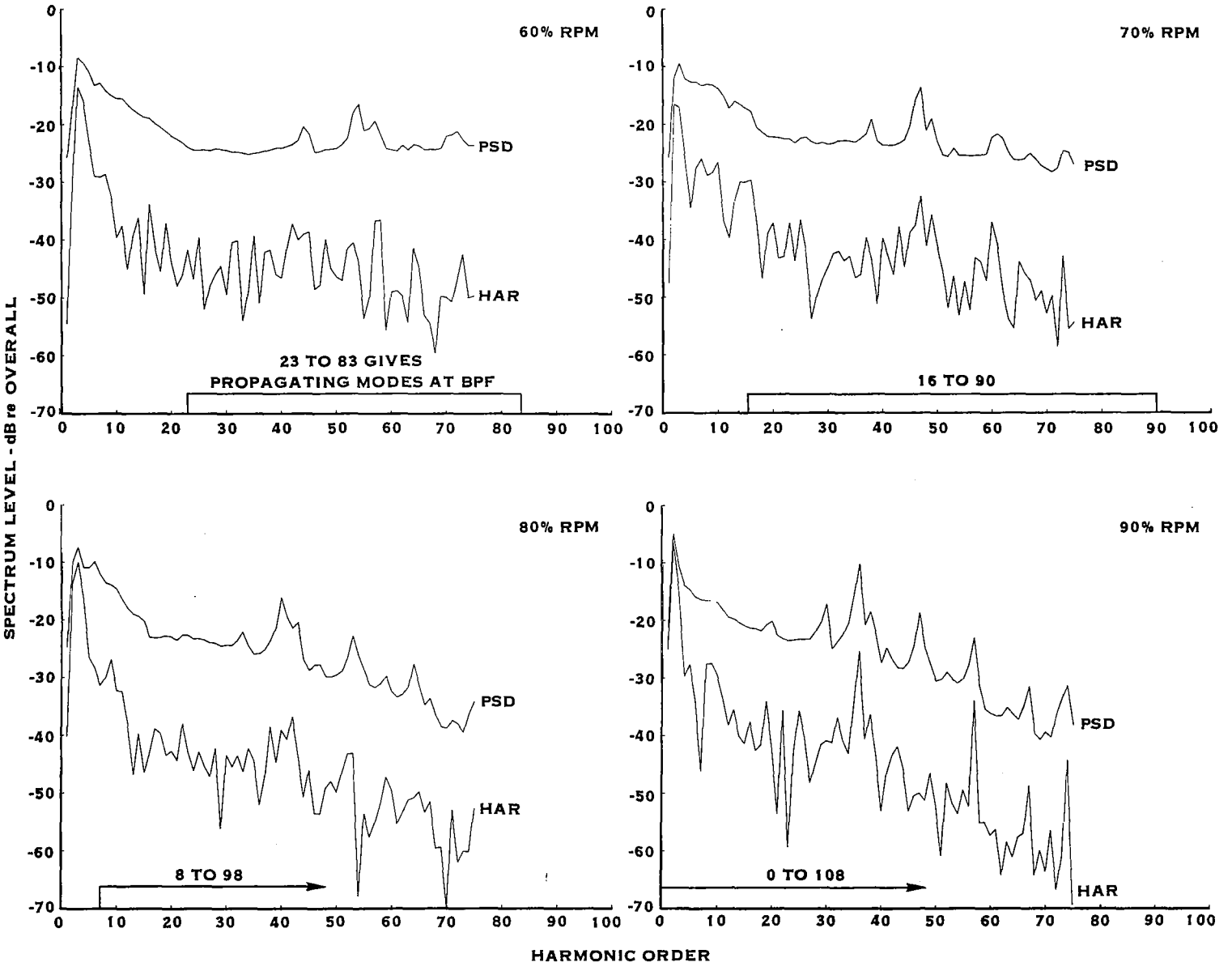

Figure 21. Digital spectrum plots for rotor pressure transducer RII/C1S (mid blade) configuration 401 (clean inlet). (Anti-alias filter set at 75E for all RPM's.)

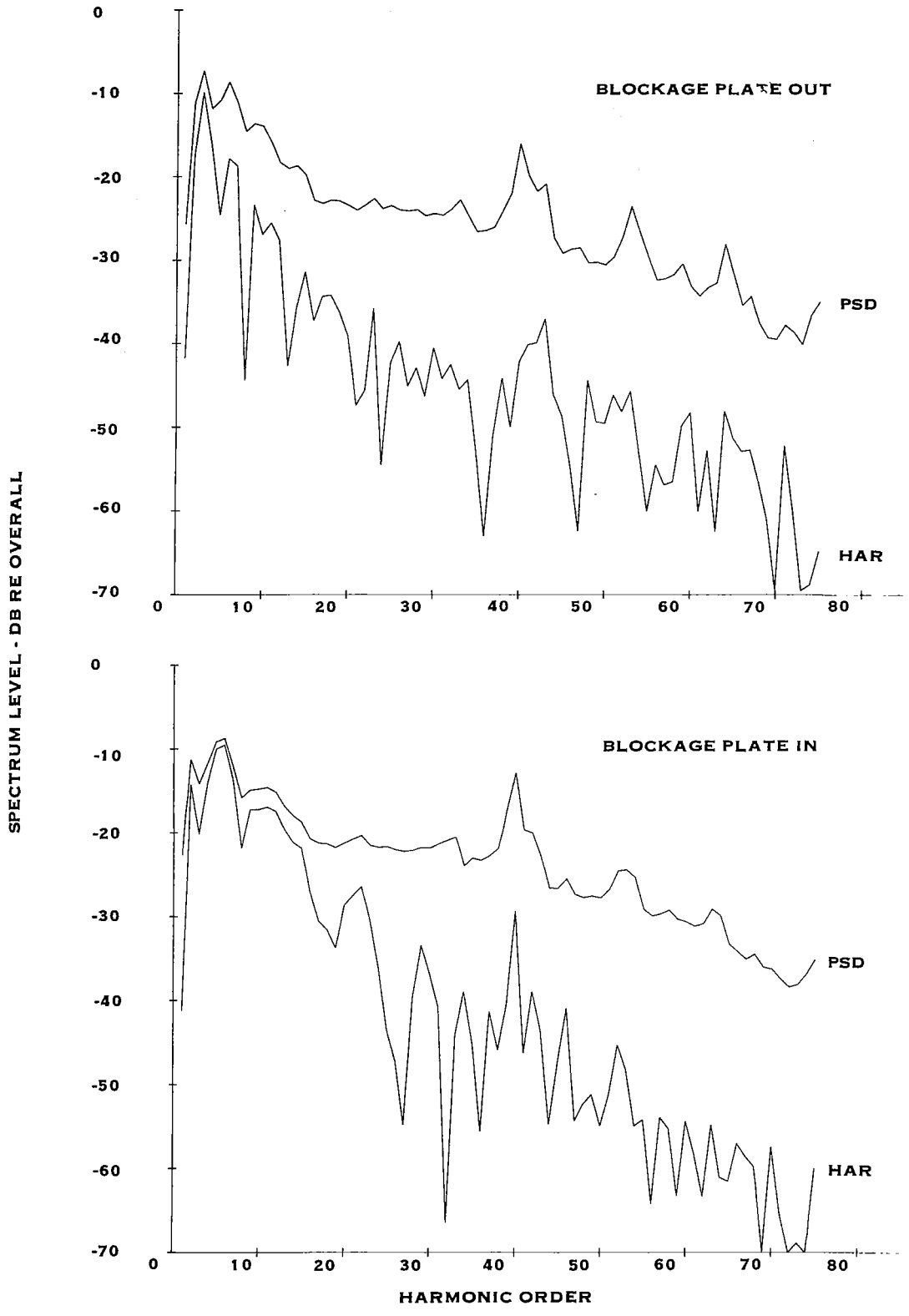

Figure 22. Comparison of blade pressure spectra with and without blockage plate. (Mid blade transducer; 80% RPM; Anti-alias filter at 75E)

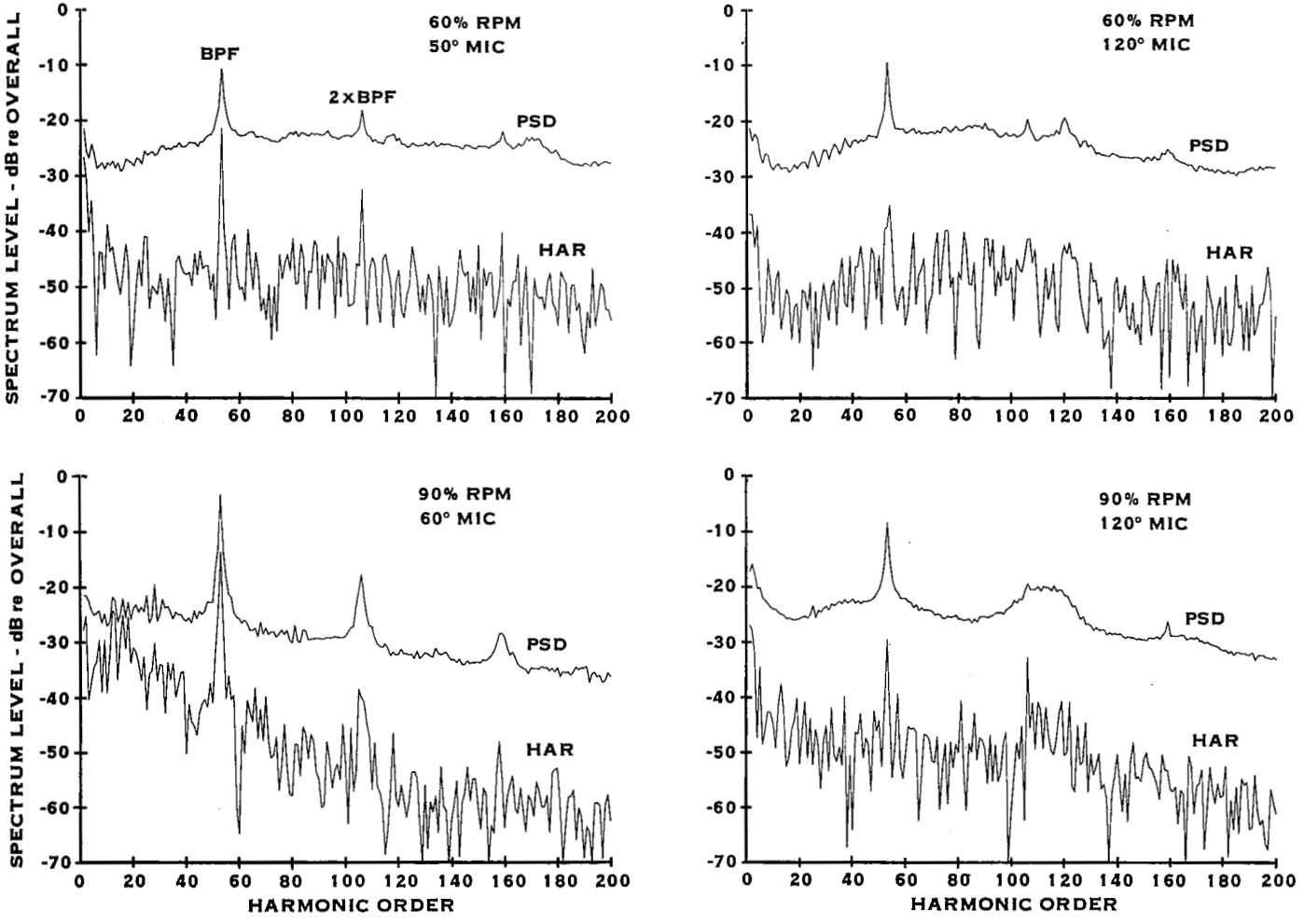

Figure 23. Far field sound pressure spectra for configuration 401 (clean inlet) showing that noise signals are predominantly random even at multiples of blade passing frequency (Anti-alias fitter at 200E)

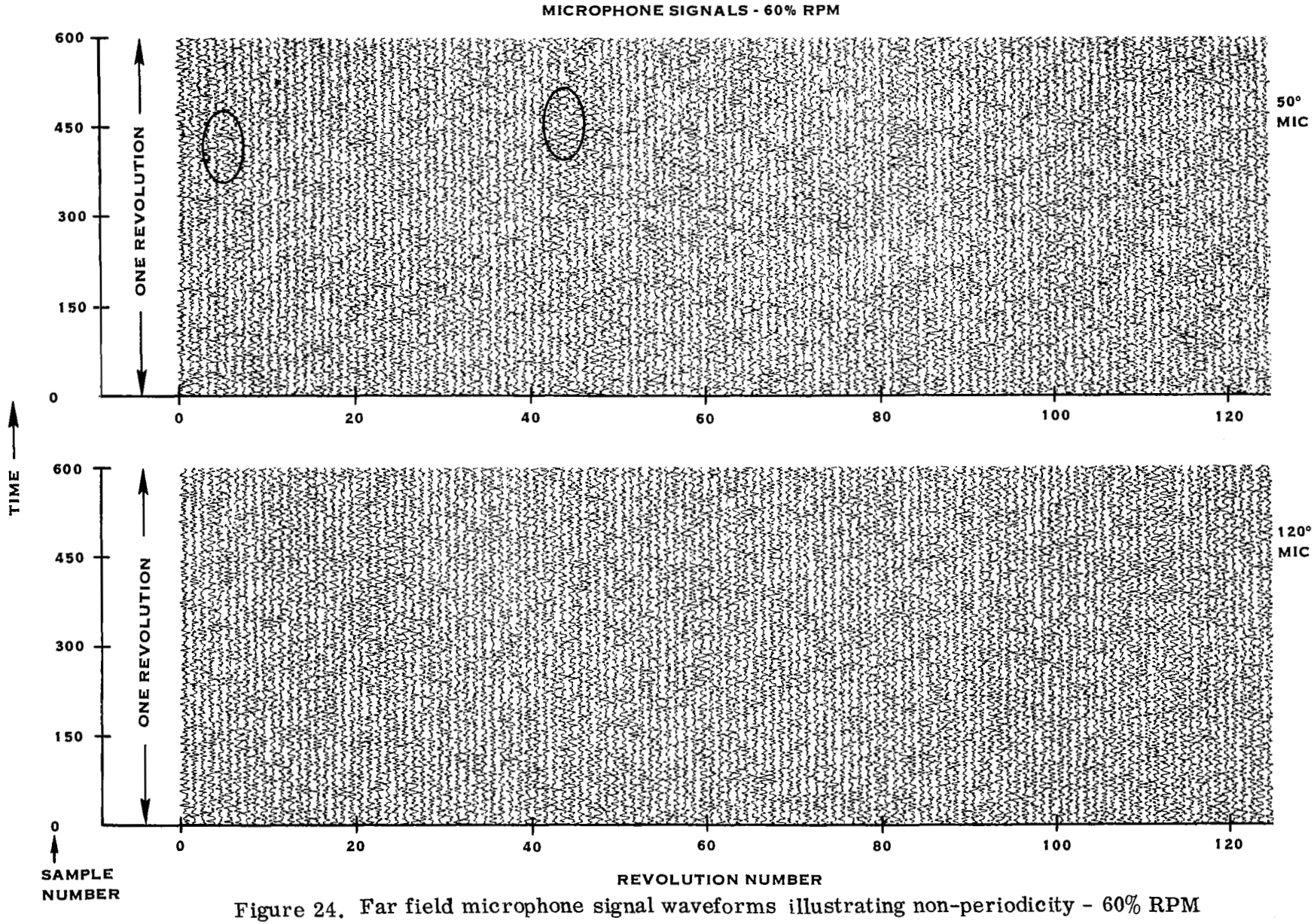

Figure 24. Far field microphone signal waveforms illustrating non-periodicity - 60% RPM

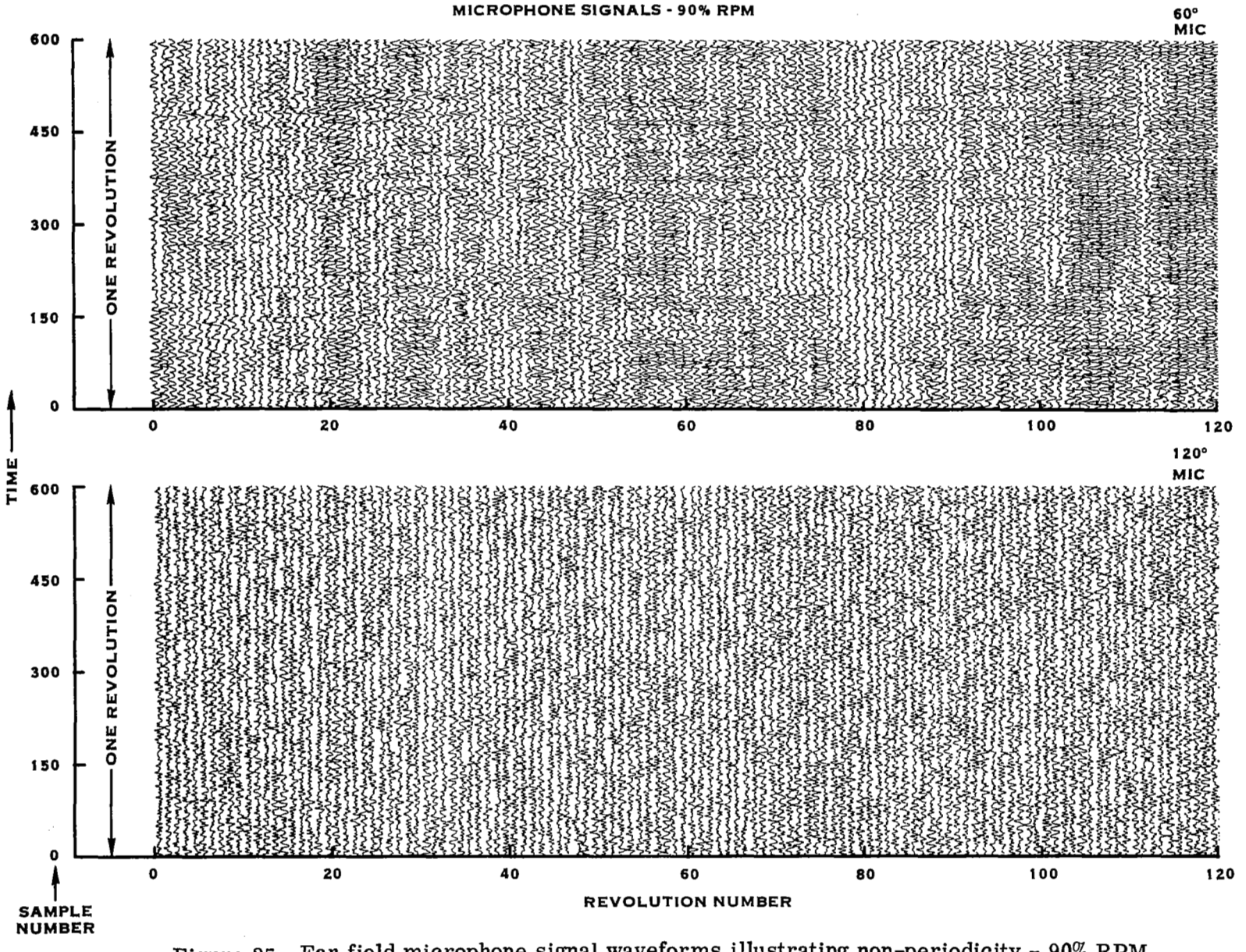

Figure 25. Far field microphone signal waveforms illustrating non-periodicity - 90% RPM

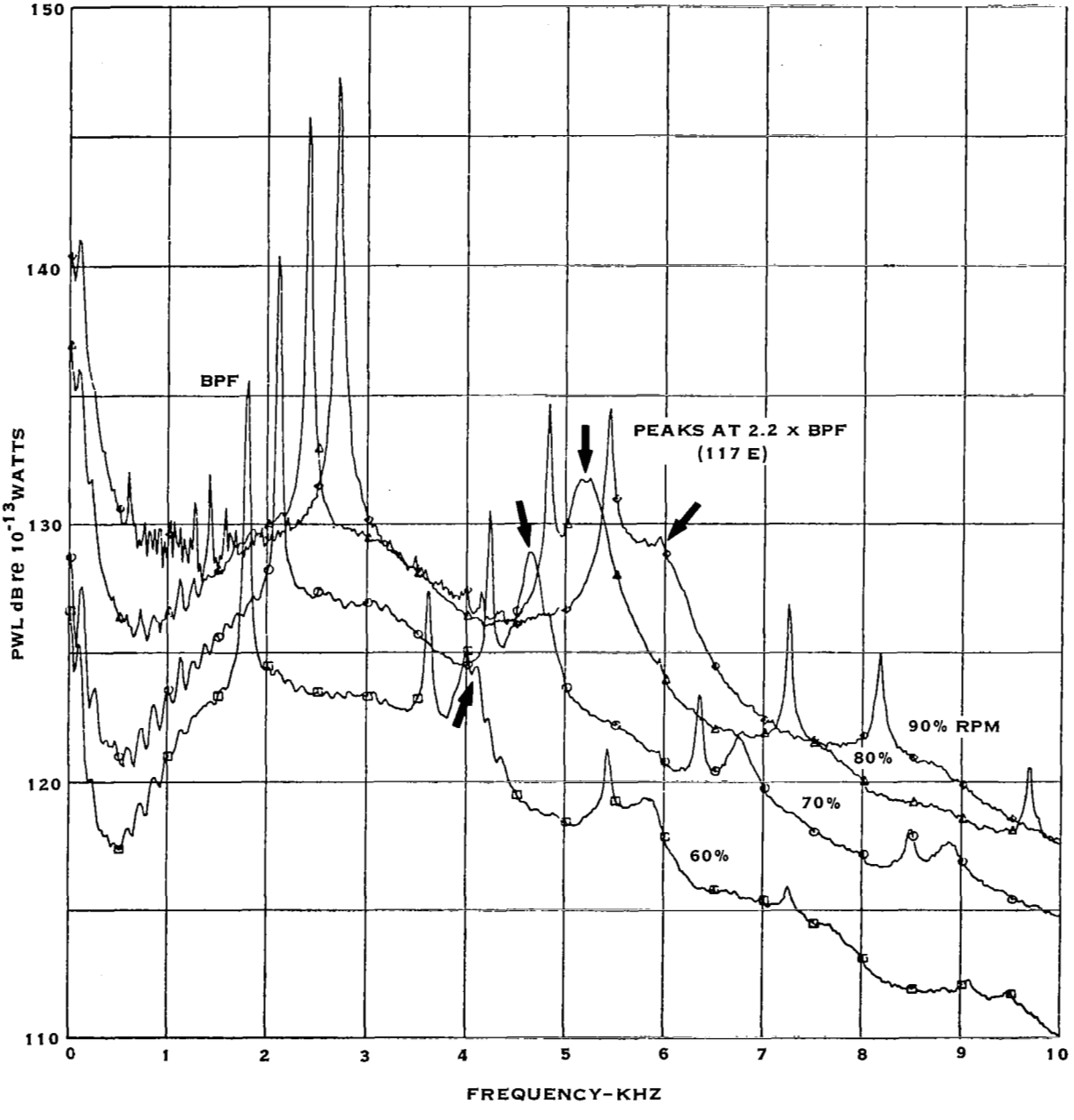

Figure 26. Spectra of sound power for clean inlet configuration showing occurance of "haystack" spectrum component at constant E order (independent of RPM). These 500 point spectra were calculated by NASA-Lewis by integration of 500 point sound pressure spectra measured by the microphones shown in figure 3.

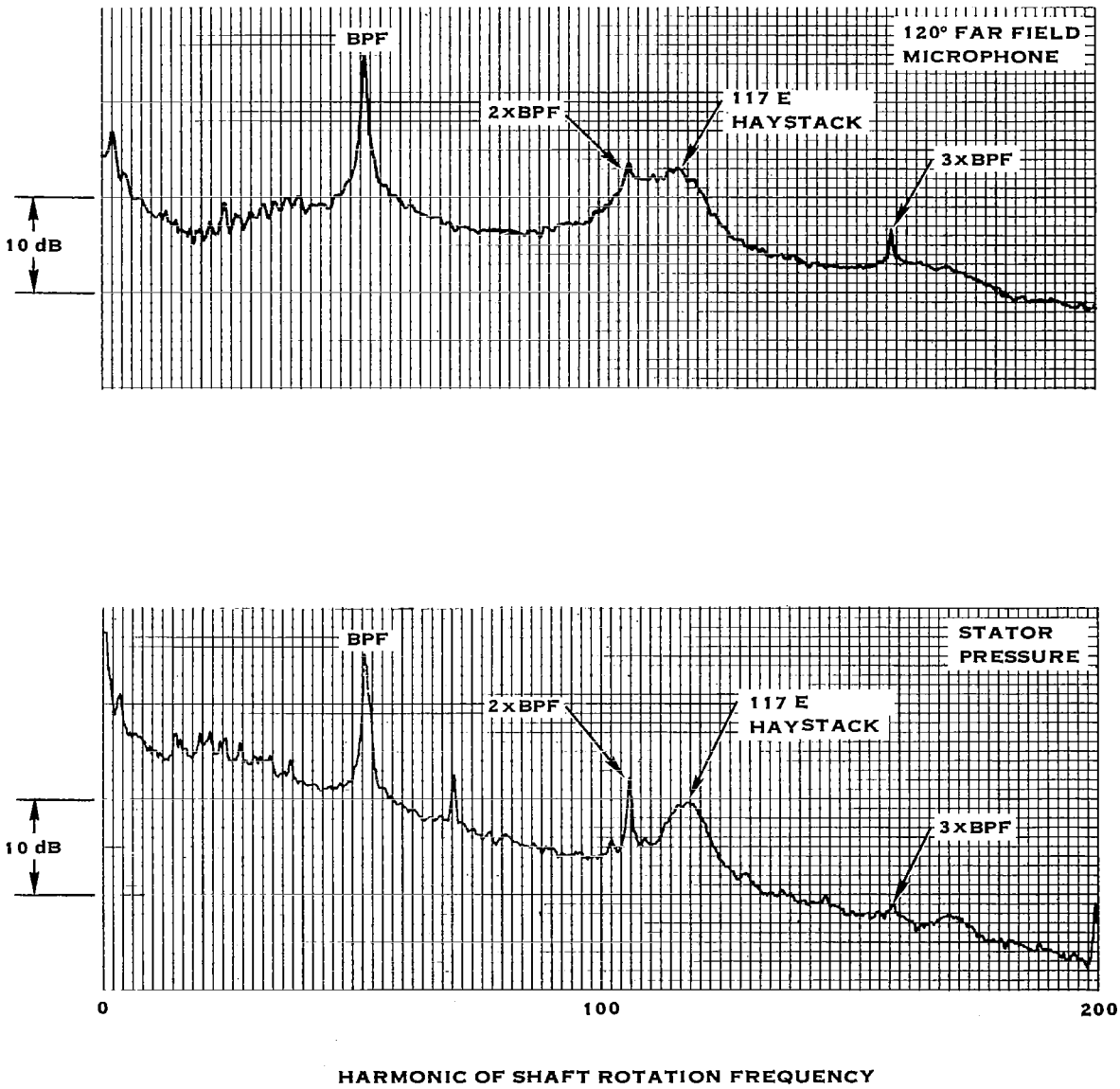

Figure 27. Comparison of spectra of stator pressure and far field microphone signal at 90% RPM indicating stator excitation as the source of the 117E "haystack".

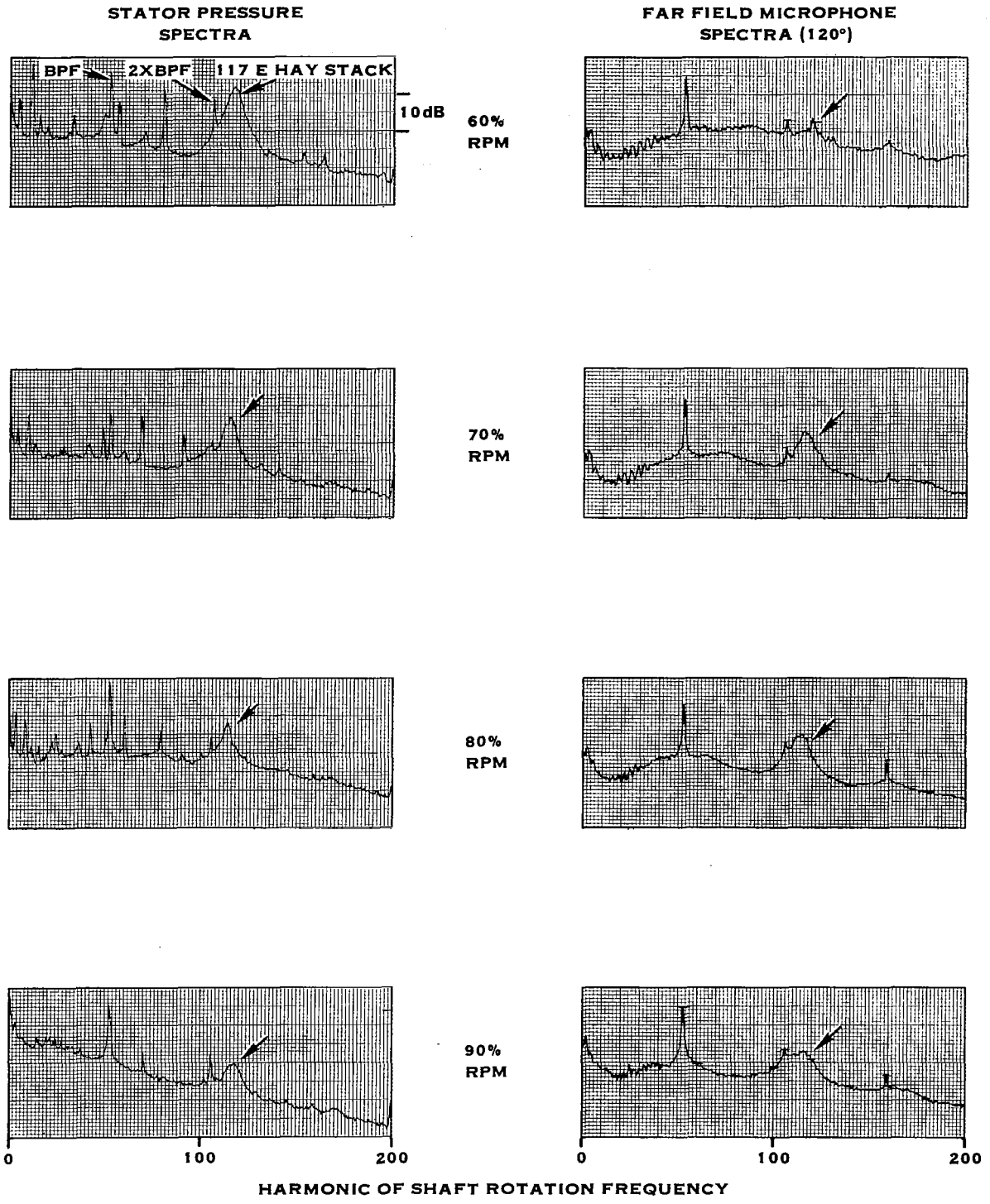

Figure 28. Comparison of microphone and stator pressure spectra showing source of 117E "haystack" and its independence of RPM.

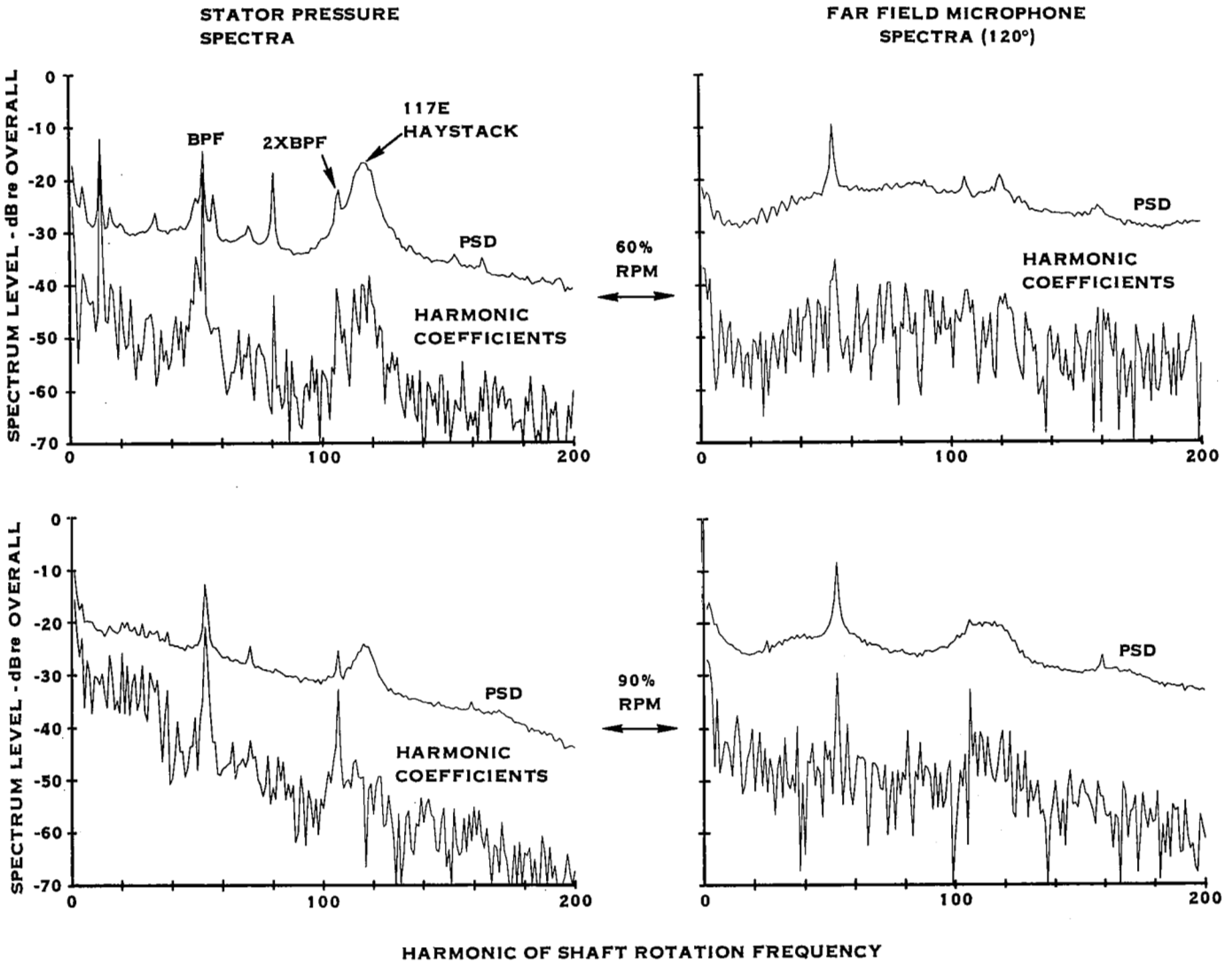

Figure 29. Digital power spectral densities (PSD) and harmonic coefficients (from signal enhanced waveforms) compared for stator pressure and microphone signals (Anti-alias filter at 200E)

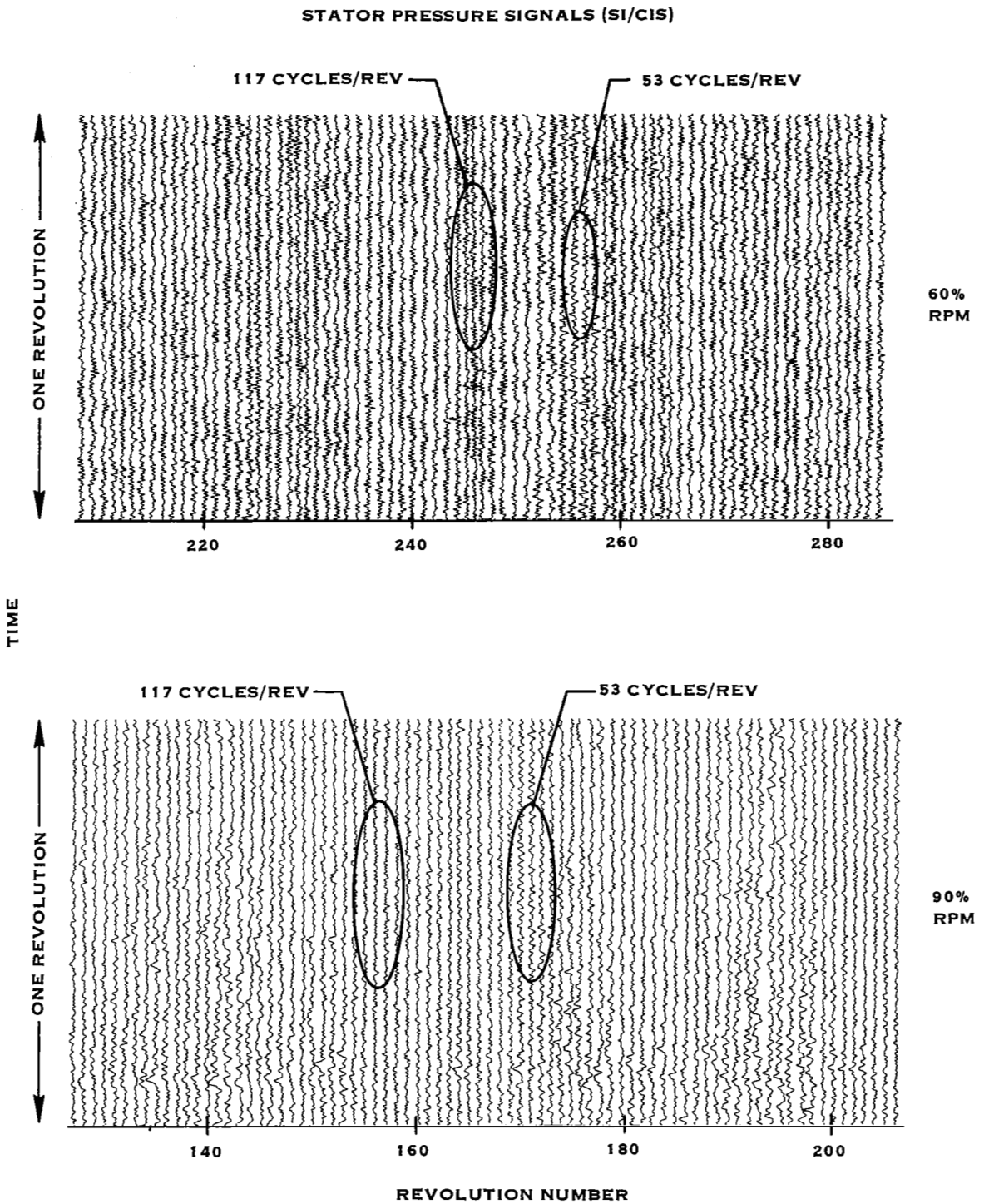

Figure 30. Waveforms from stator pressure transducer exhibiting intermittent 53E and 117E (approximate) response

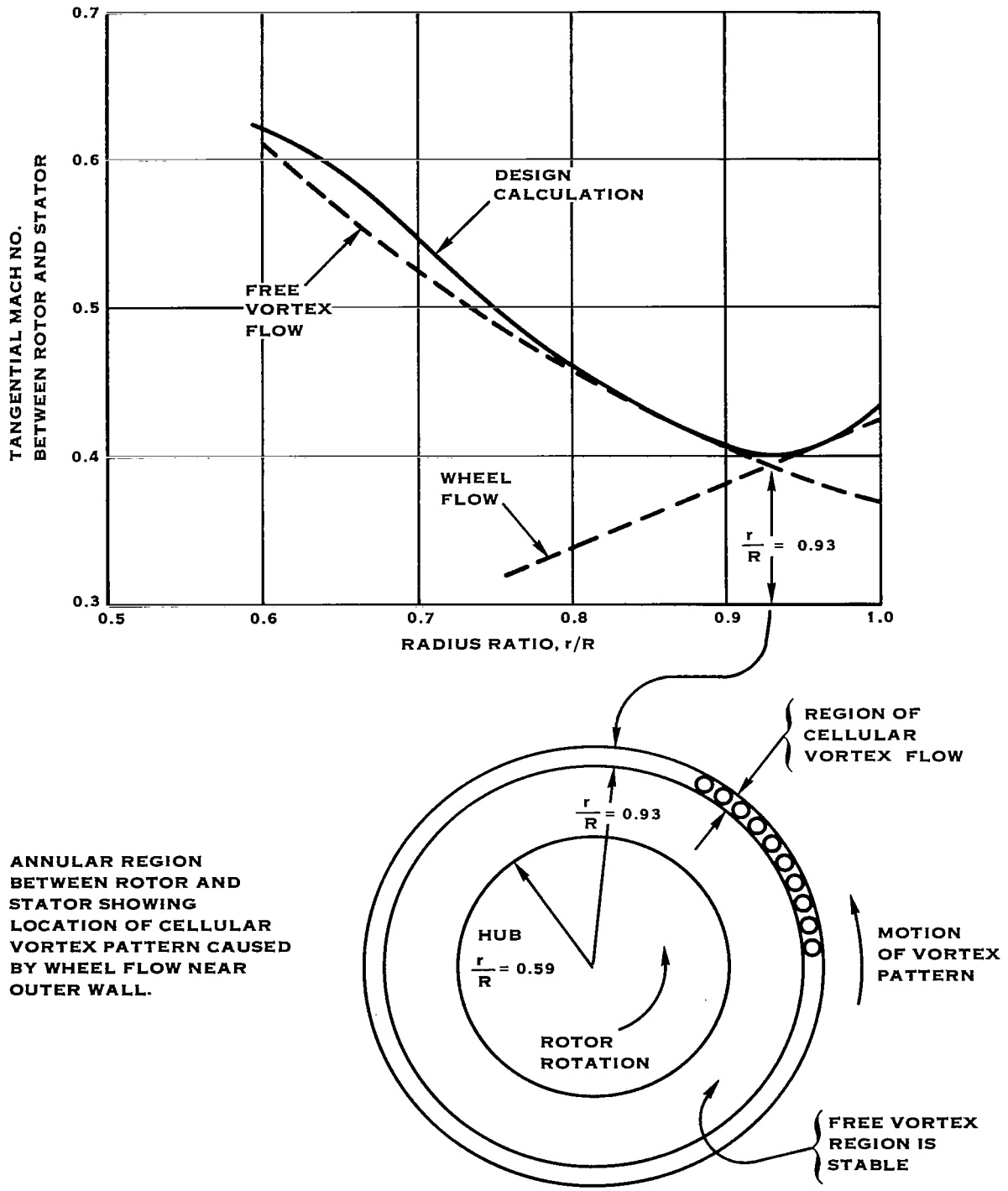

ANNULAR REGION BETWEEN ROTOR AND STATOR SHOWING LOCATION OF CELLULAR VORTEX PATTERN CAUSED BY WHEEL FLOW NEAR OUTER WALL.

Figure 31. Relation between tangential velocity distribution and cellular flow pattern

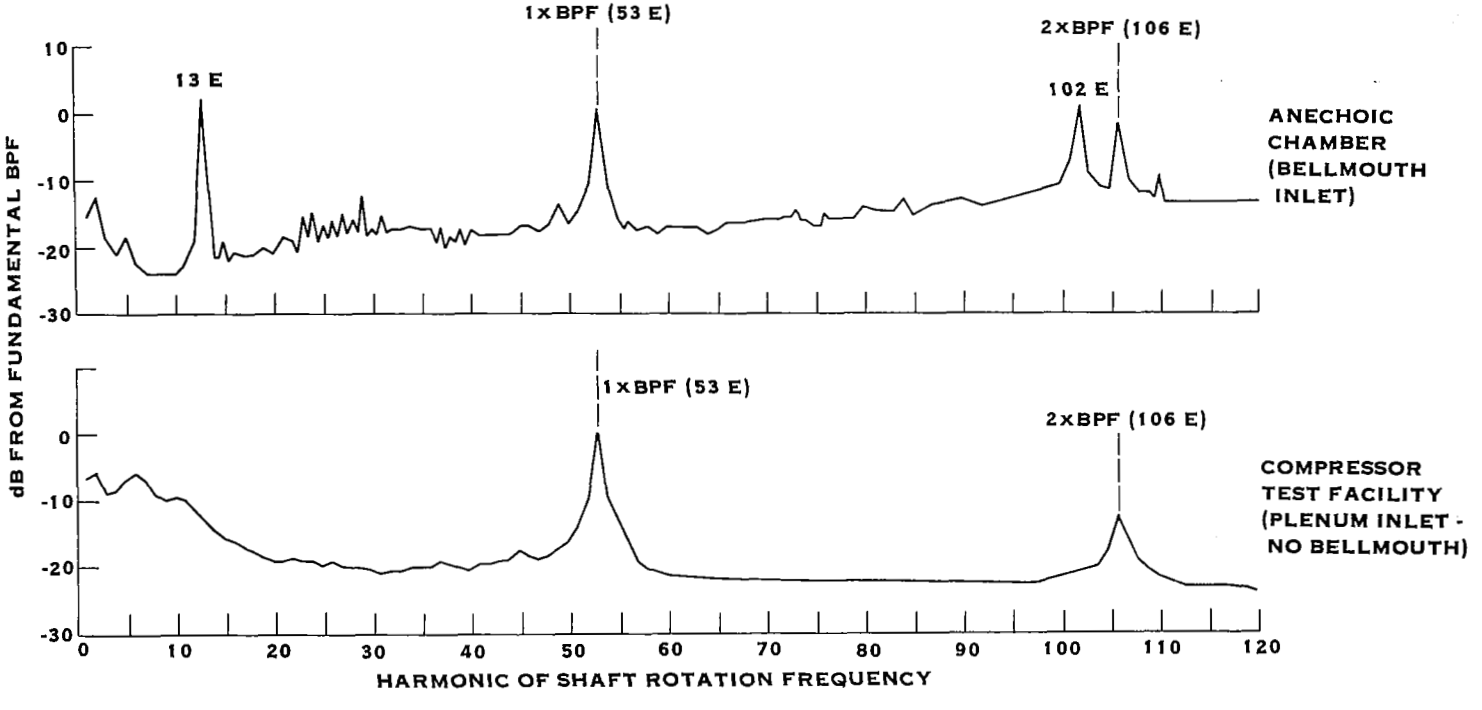

Figure 32. Comparison of inlet noise spectra from 0.277 scale model of QF-1 run in anechoic chamber with bellmouth and in compressor test facility with air drawn from plenum. (Reproduced from reference 14.)

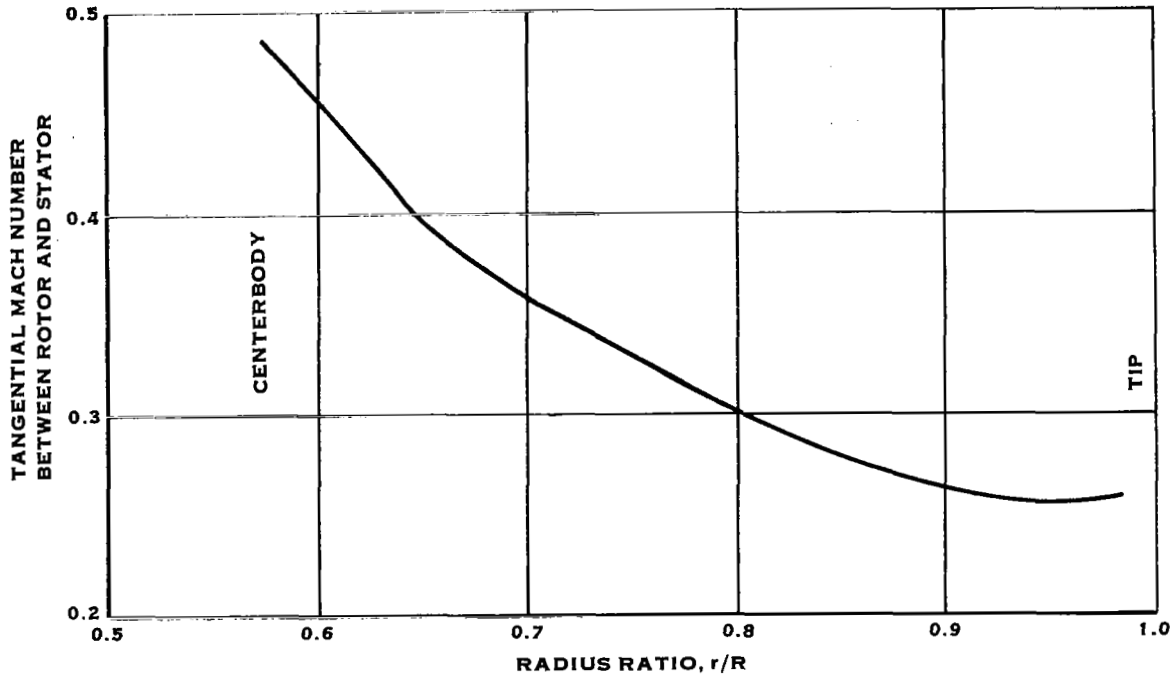

Figure 33. Swirl Mach number distribution between rotor and stator for 27.7% scale model of QF-1 measured in NASA Compressor Test Facility (ref. 14). Compare this with full scale calculations in figure 29 and note reduced upturn near outer wall.

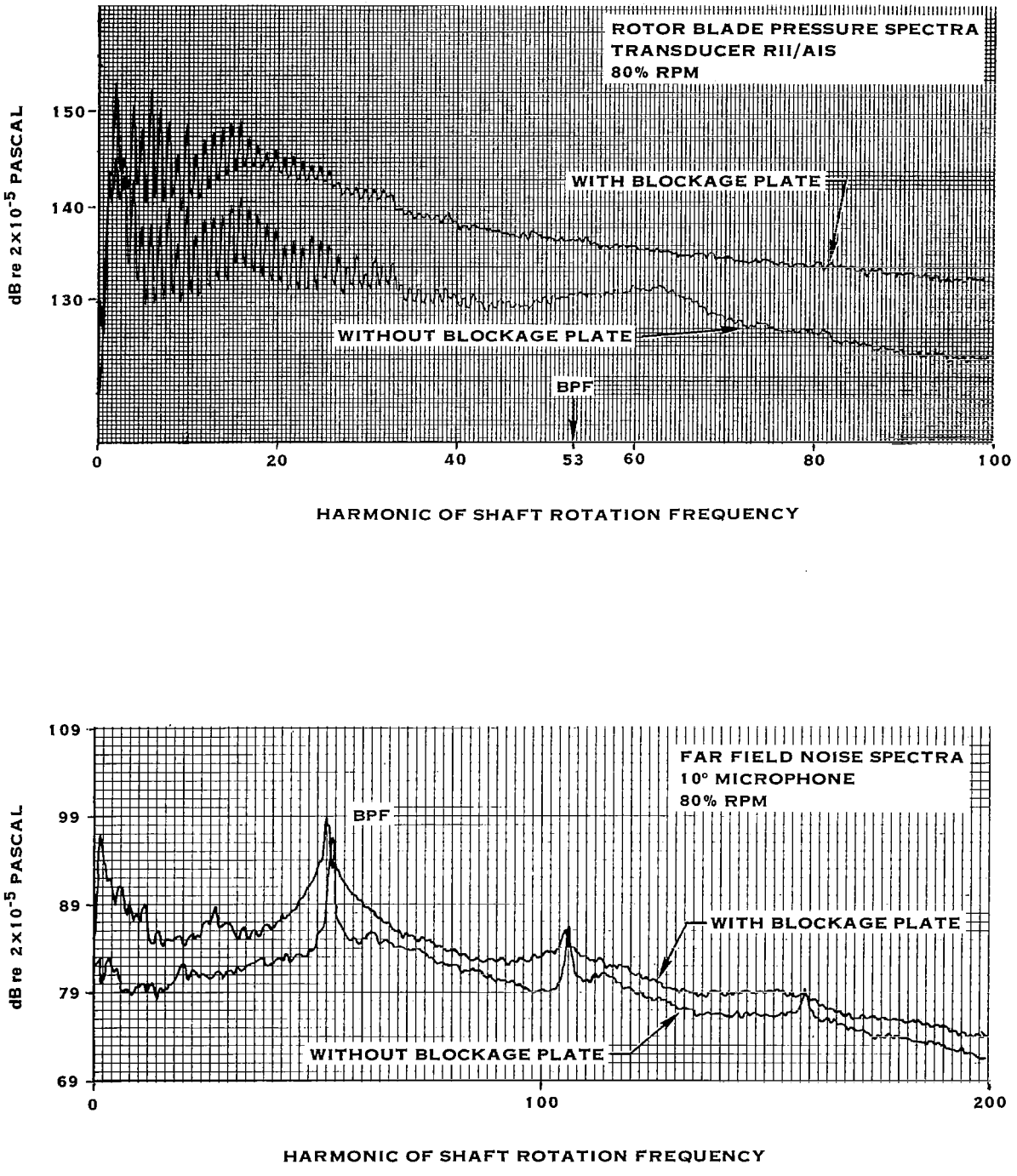

Figure 34. Effect of blockage plate on spectra of blade pressure and noise. No significant tone component at blade passing frequency (53rd shaft frequency harmonic).

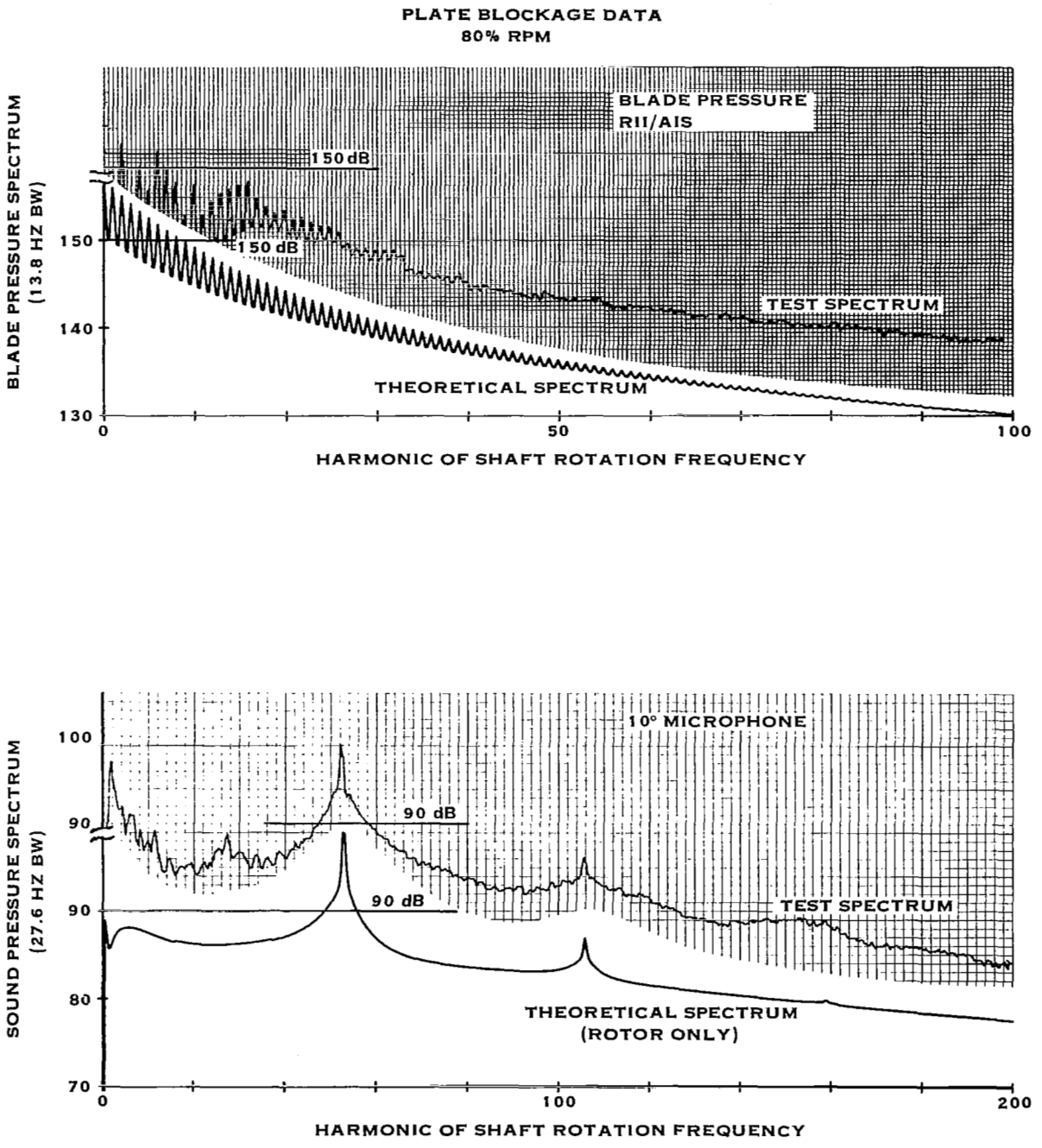

Figure 35. Prediction of noise spectrum from blade pressure spectrum using inlet turbulence noise theory for blockage plate data

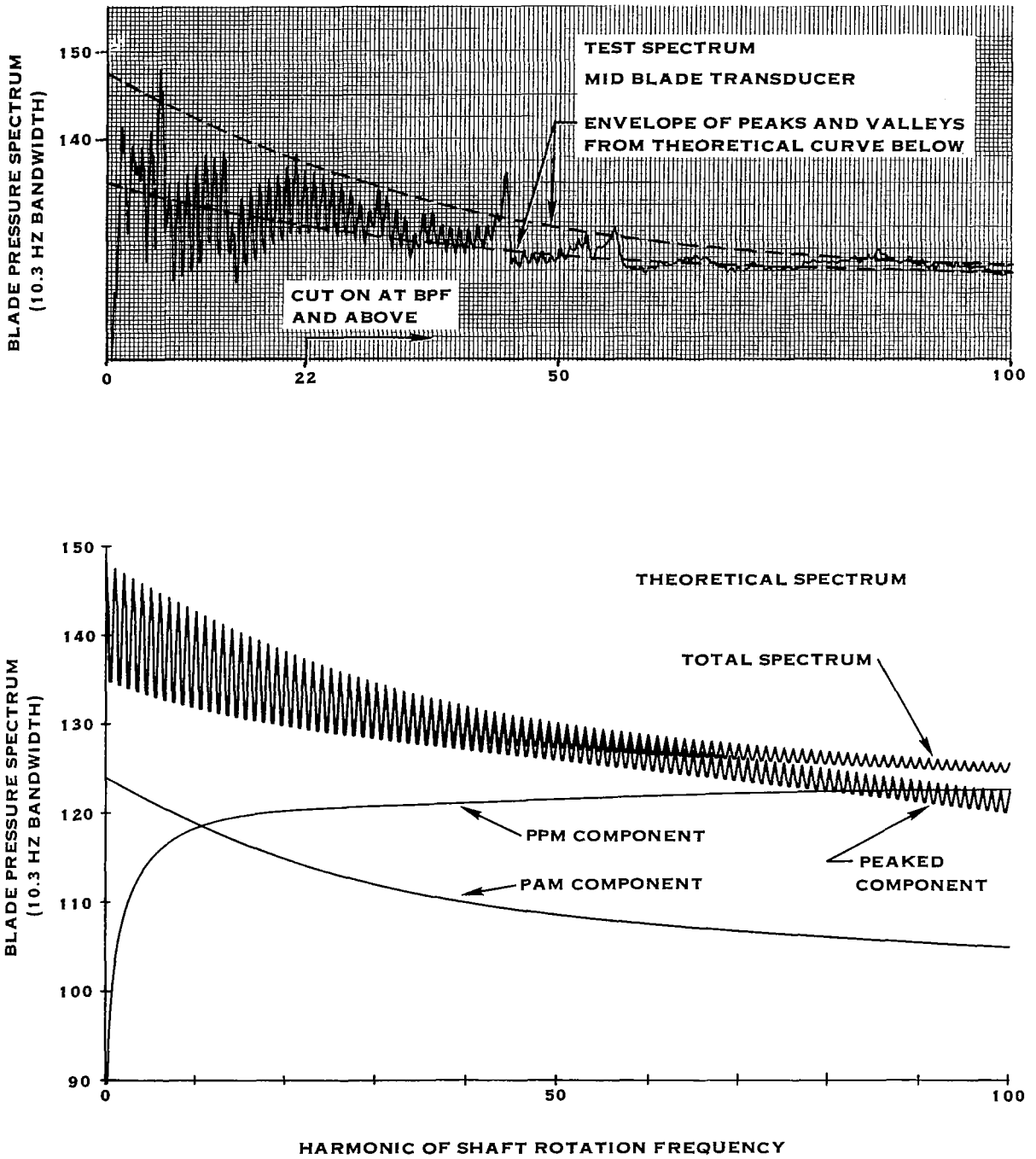

Figure 36. Comparison of experimental and theoretical blade pressure spectra (clean inlet, 60% RPM)

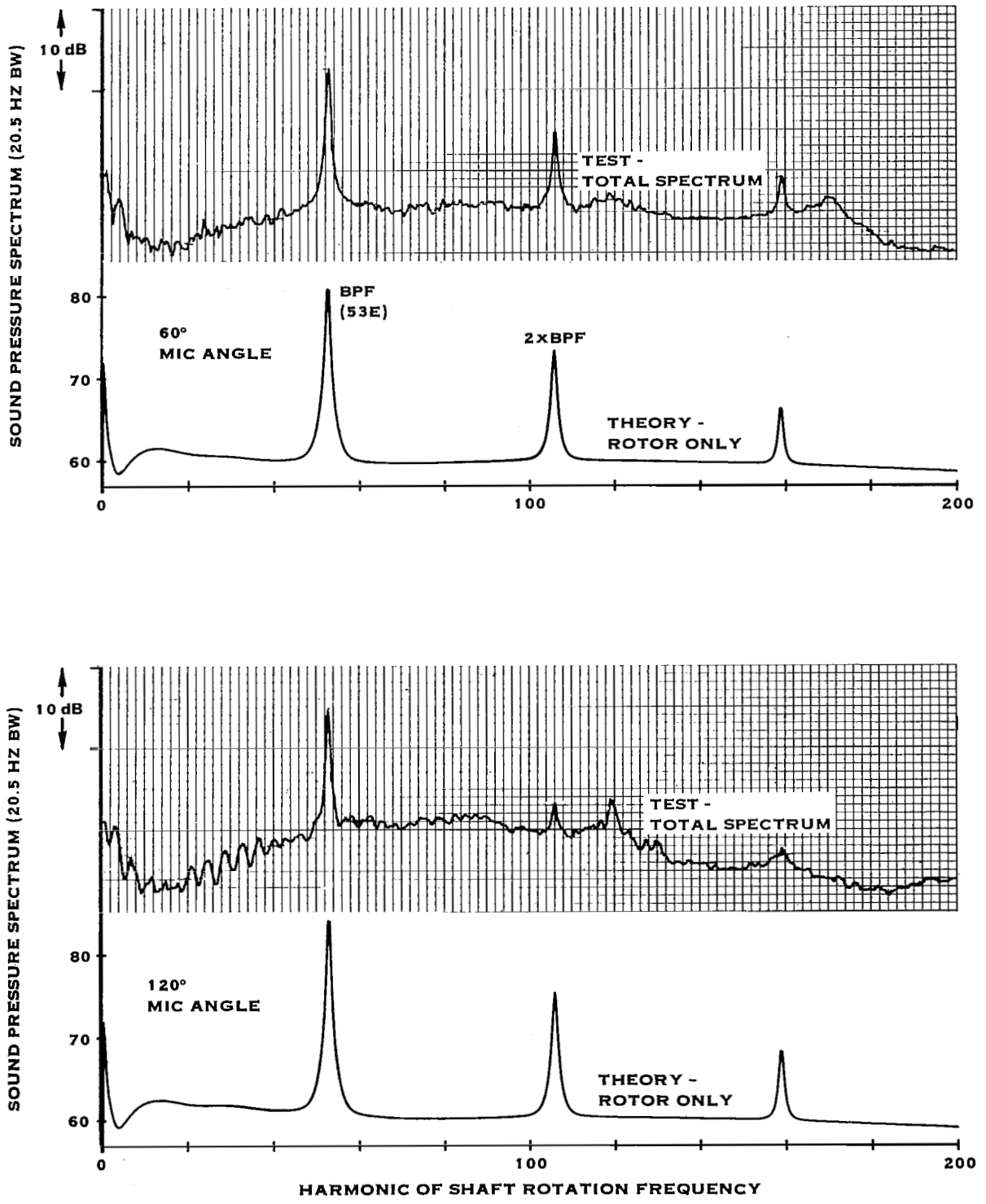

Figure 37. Comparison of experimental and theoretical sound pressure spectra for clean inlet, 60% RPM

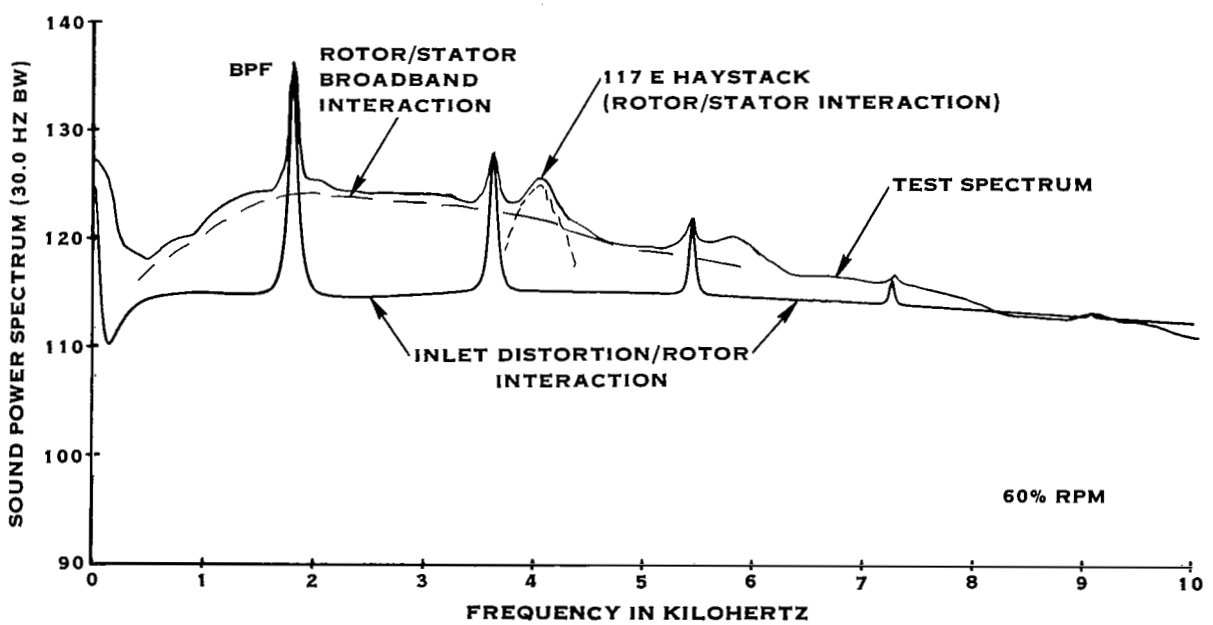

Figure 38. Power level account giving contributions of various sources to spectrum of sound power - 60% RPM. Sound power data supplied by NASA-Lewis.

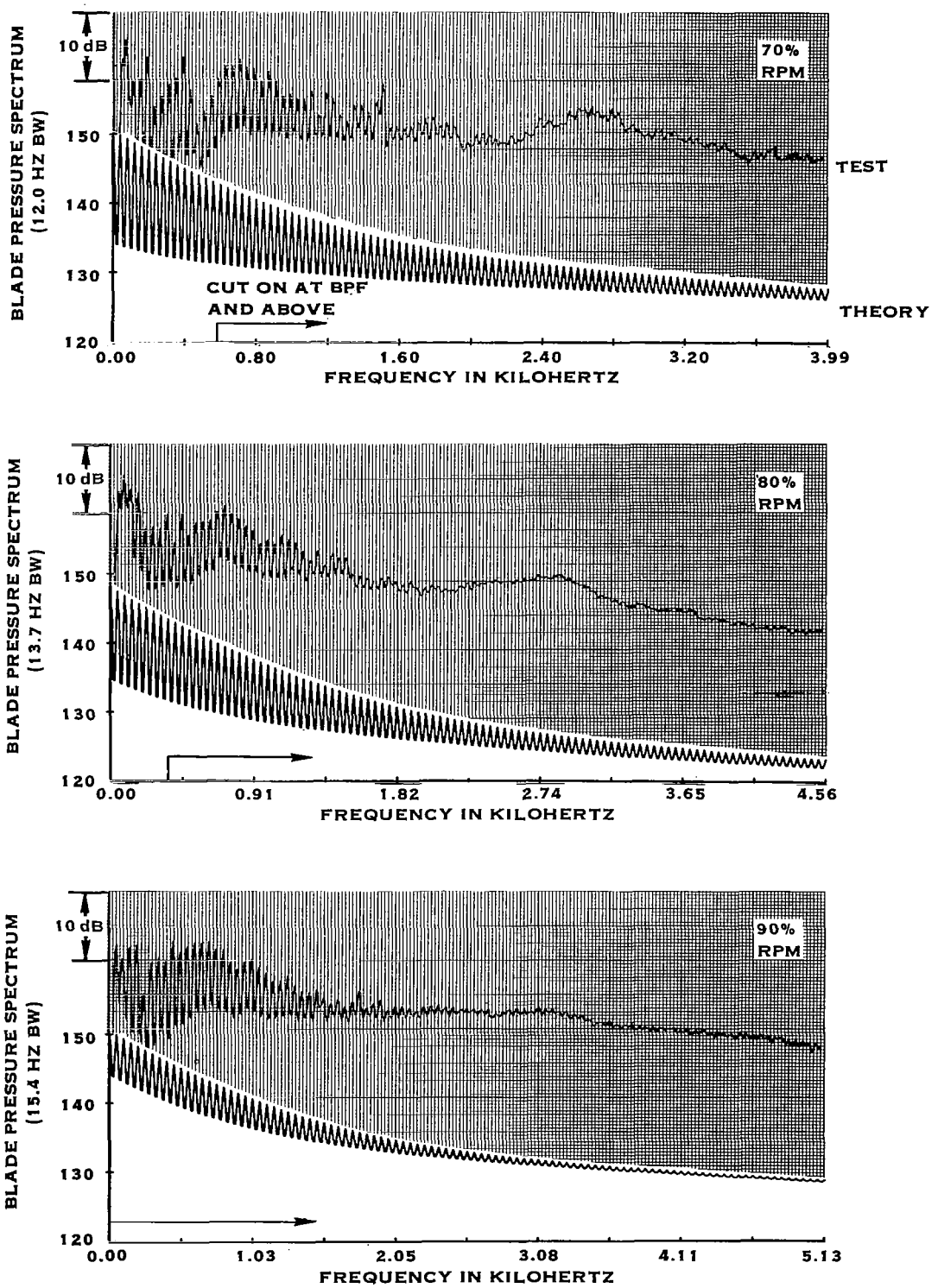

Figure 39. Fit of theoretical blade pressure spectra to measured spectra for clean inlet. Compare shapes only; levels are arbitrary.

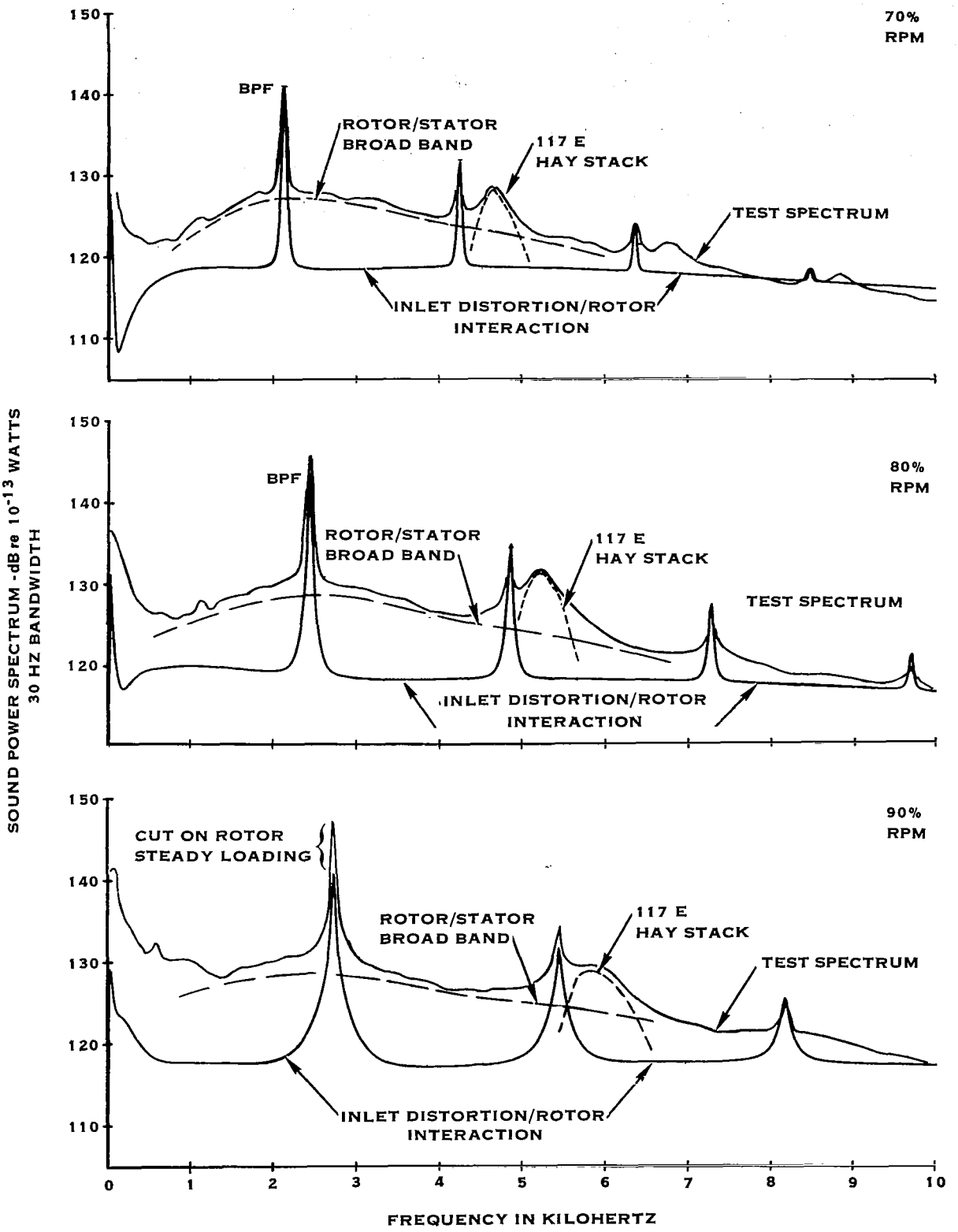

Figure 40. Power level account giving contributions of various sources to spectrum of sound power - 70, 80, 90% RPM. Note: rotor cut on at 90% RPM

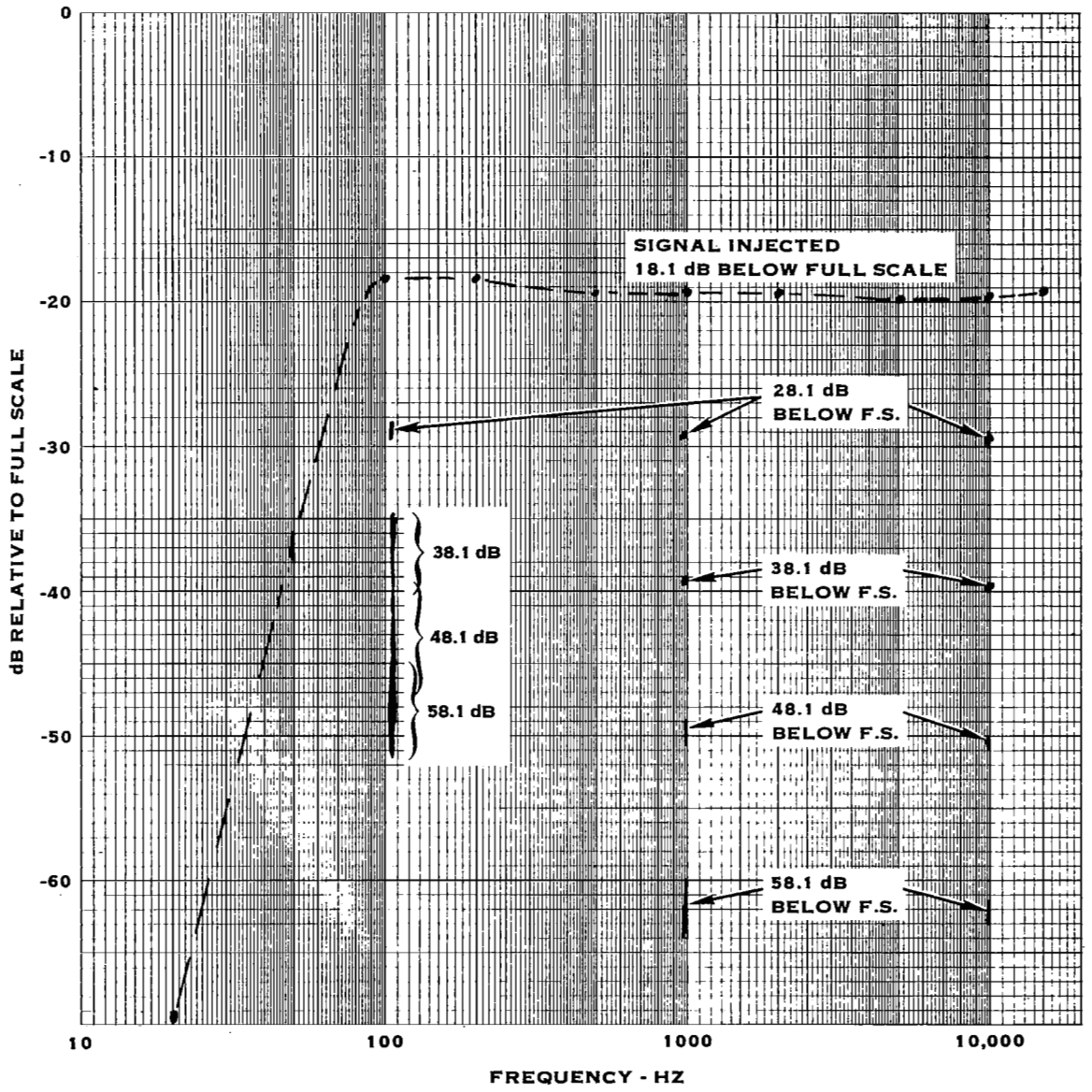

Figure 41. Frequency response and linearity of data system including rotary transformer, frequency compensation network, recorder, playback machine and spectrum analyzer. (Vertical bands at 100 Hz caused by tape flutter which was amplified by compensation network.)

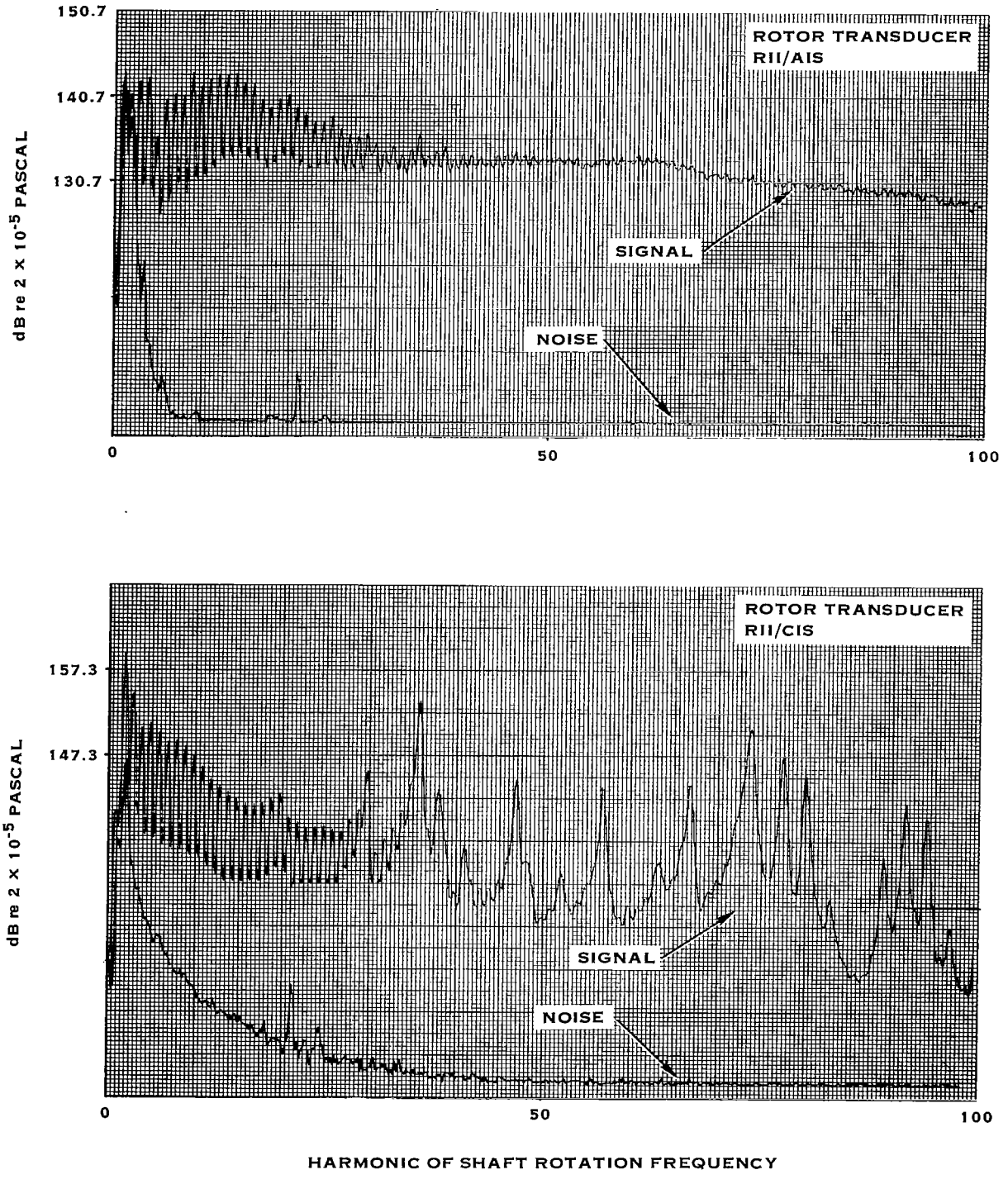

Figure 42. Demonstration of favorable signal to noise ratio as a function of frequency. Clean inlet configuration 90% RPM. (Transducer RII/AIS was used for rotor noise prediction.)

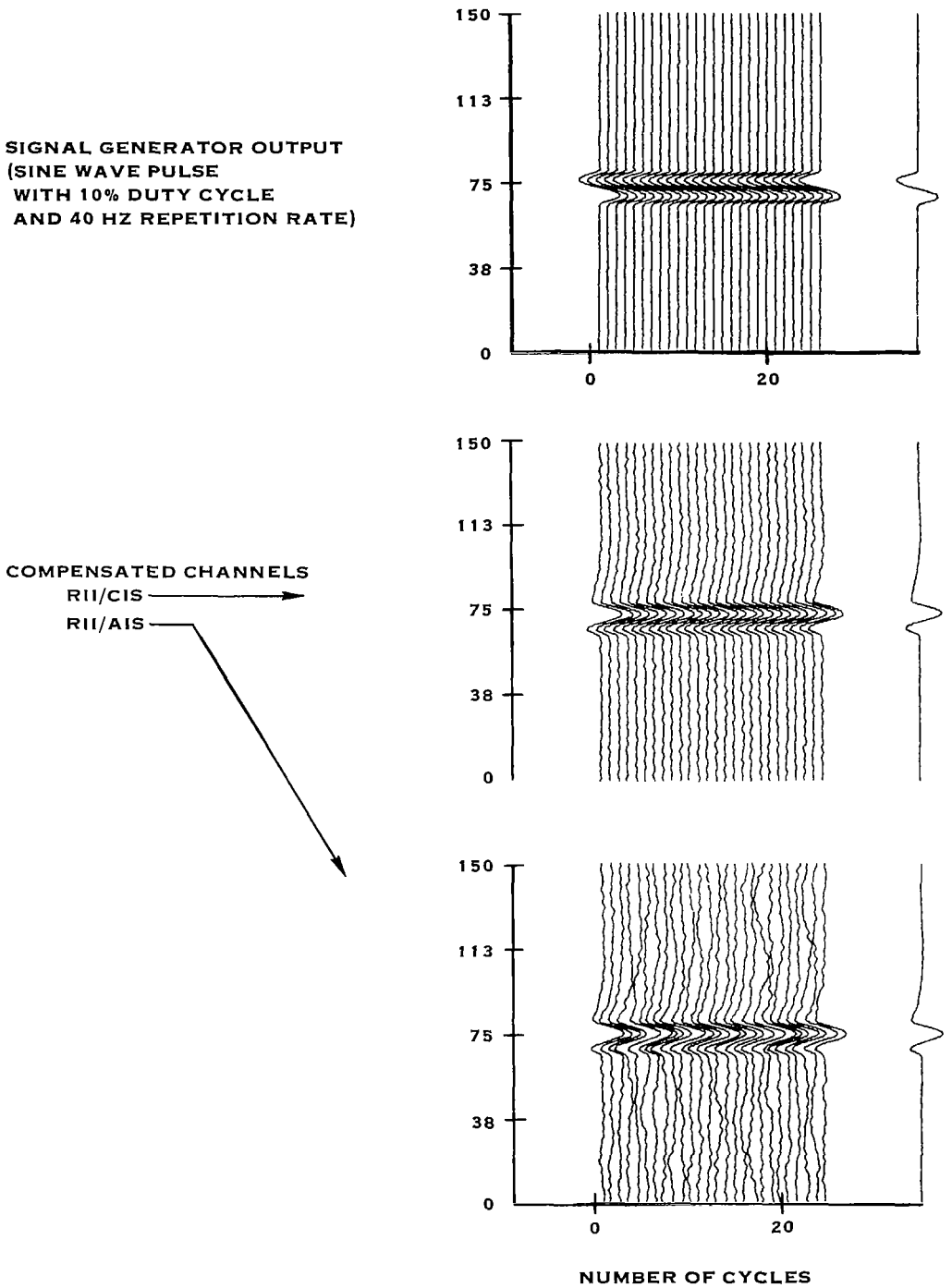

Figure 43. Test signal transmitted by rotary transformer and frequency response compensating network

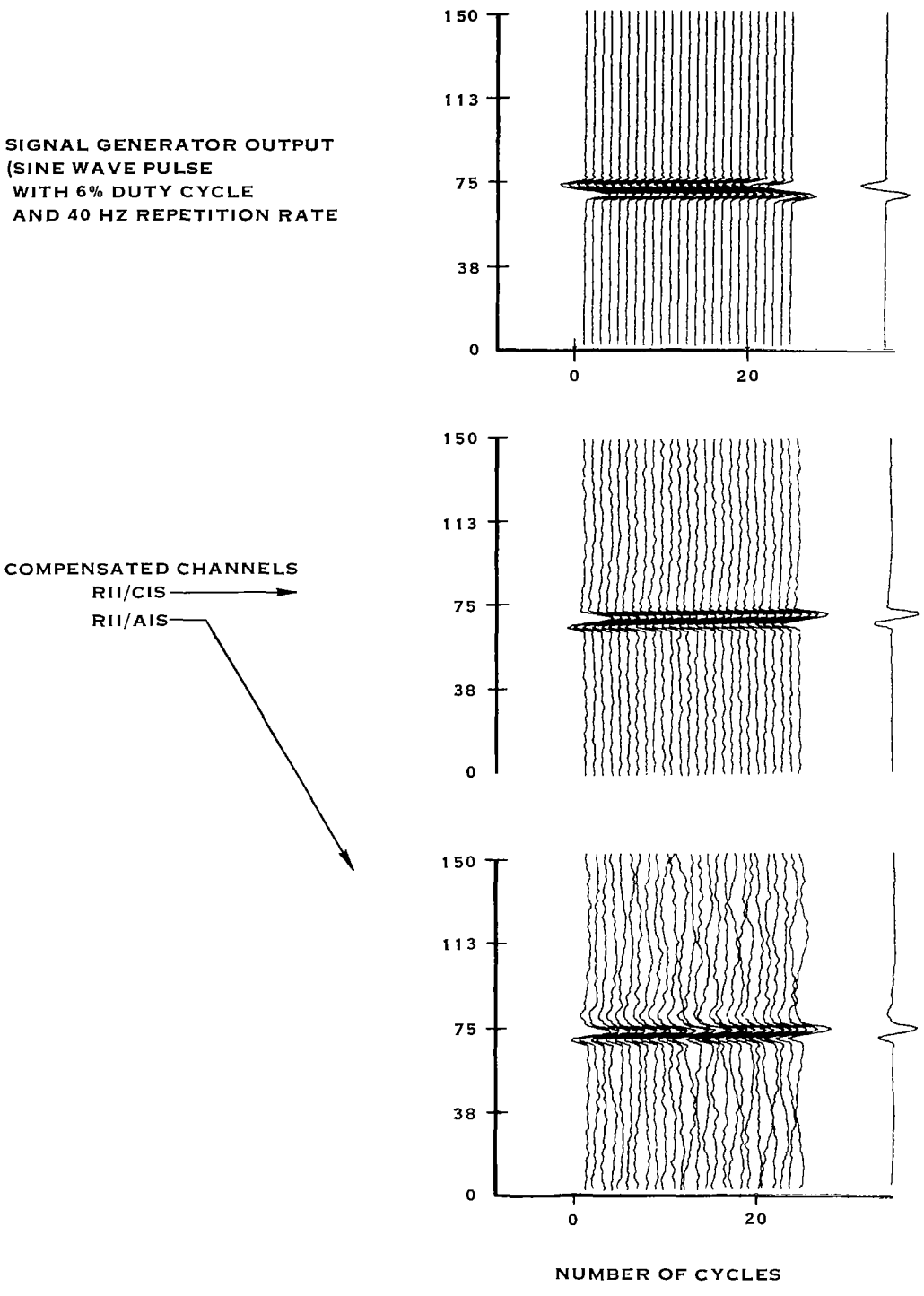

Figure 44. Test signal transmitted by rotary transformer and frequency response compensating network